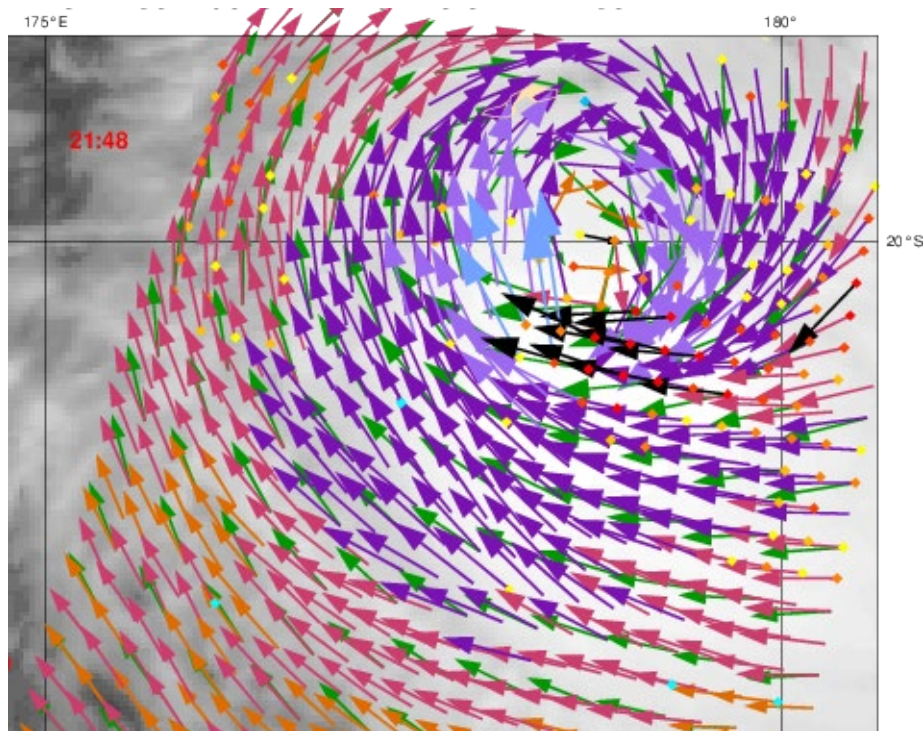




## C-band High and Extreme-Force Speeds (CHEFS)

### - Final Report -



Ad Stoffelen<sup>1</sup>, Alexis Mouche<sup>2</sup>, Federica Polverari<sup>3</sup>,  
Gerd-Jan van Zadelhoff<sup>1</sup>, Joe Sapp<sup>4,5</sup>, Marcos Portabella<sup>3</sup>,  
Paul Chang<sup>4</sup>, Wenming Lin<sup>6</sup> and Zorana Jelenak<sup>4,7</sup>

<sup>1</sup> Royal Netherlands Meteorological Institute (KNMI), De Bilt, The Netherlands

<sup>2</sup> Institut Français de Recherche pour l'Exploitation de la Mer (IFREMER), Plouzané, France

<sup>3</sup> Institut de Ciències del Mar (ICM-CSIC), Barcelona, Spain

<sup>4</sup> NOAA/NESDIS Center for Satellite Applications Research (STAR), College Park, MD, USA

<sup>5</sup> Global Science & Technology (GST), Inc., Greenbelt, MD, USA

<sup>6</sup> Nanjing University of Information Science and Technology (NUIST), Nanjing, China

<sup>7</sup> University Corporation for Atmospheric Research, Boulder, CO, USA

## Front Cover

ASCAT-B scatterometer wind arrows in colour with an infrared satellite image (from Himawari) and numerical weather prediction model forecast winds from ECMWF as green arrows. The scatterometer and model winds are from 28 December 2019 21:48, while the IR is from 21:30 UTC. The scatterometer winds are coloured according to the Beaufort scale, winds up to 5 Bft. ( $10.7 \text{ m s}^{-1}$ ) are in red, winds as of 6 Bft. are coloured as shown in the legend below. A black arrow or flag indicates that the KNMI QC flag is set ( $\text{MLE} > 18$ ). The coloured dots give the value of the Maximum Likelihood Estimator (MLE) which indicates how well an observation fits to the Geophysical Model Function (GMF). High MLE values indicate high spatial wind variability in the Wind Vector Cell, WVC (from [http://projects.knmi.nl/scatterometer/tile\\_prod/tile\\_app.cgi?](http://projects.knmi.nl/scatterometer/tile_prod/tile_app.cgi?)).

(c) EUMETSAT/KNMI

## Acknowledgements

EUMETSAT supported the CHEFS study, which provided resources to KNMI, ICM and IFREMER to lead and progress on the ocean winds community issue of an in-situ reference for satellite and model calibration of extreme winds. Such study is only possible with access to uniformly reprocessed wind data sets which were obtained from NOAA/NESDIS/STAR OSWT dropsondes and SFMR, ICOADS buoys, ECMWF buoy archive and ERA5 winds, ESA Sentinel-1 SAR and RadarSat SAR VV and VH data. In addition, we were informed by a NHC meeting in 2009 on tropical hurricane winds, discussions at several IOVWST meetings and many more informal contacts with scientists knowledgeable in ocean wind measurements, Specifically, discussions with Doug Vandemark, Jean Bidlot, Jim Edson, Lucia Pineau-Guillot, Ralph Foster and Mark Bourassa specifically contributed to this report.

Version 1: 18 March 2020.

Version 2: 10 April 2020, Minor update figure 24.

Version 3: 3 June 2020, Correction of figure 39 and associated text, thanks to Sébastien Langlade, DIROI/PREVI, Météo-France.

## CONTENTS

1.	INTRODUCTION .....	4
2.	DATA COLLECTION .....	6
2.1.	SFMR and dropsonde wind data.....	6
2.2.	Synthetic Aperture Radar and L-band radiometer.....	9
2.3.	ASCAT wind products reprocessed with ERA5 model winds .....	12
2.4.	Buoy wind description .....	13
2.5.	Effect of Stress-Equivalent Reference Winds.....	13
2.6.	Summary .....	16
3.	SFMR CAL/VAL USING DROPSONDES.....	17
3.1.	SFMR/dropsonde collocation procedure.....	17
3.2.	Dropsonde winds .....	18
3.3.	Analysis of the WL150 dropsonde winds.....	20
3.4.	SFMR and dropsonde wind comparisons.....	22
3.5.	Summary .....	28
4.	ASCAT/SFMR WIND COMPARISON .....	29
4.1.	ASCAT-related storm-centre estimates .....	29
4.2.	ASCAT/SFMR collocation approach .....	31
4.3.	ASCAT/SFMR wind comparisons.....	34
4.4.	Summary .....	38
5.	ASSESSING BUOY WIND REFERENCE QUALITY.....	39
5.1.	Cwinds versus MARS buoy winds.....	40
5.2.	ASCAT/Buoy wind comparison .....	42
5.3.	Summary .....	45
6.	SENTINEL 1 AND SFMR WIND COMPARISON.....	46
6.1.	C-band cross-polarization signal wind sensitivity .....	46
6.2.	Transects over Tropical Cyclones.....	46
6.3.	Signal sensitivity analysis with respect to ocean surface wind speed .....	50
6.4.	Saturation of VH signals.....	55
6.5.	Analysis against L-Band Brightness temperature.....	59
6.6.	Summary .....	64
7.	DISCUSSION AND CONCLUSIONS .....	65
8.	RECOMMENDATIONS.....	68
9.	REFERENCES.....	69
10.	ACRONYMS .....	73

## 1. INTRODUCTION

Global information on the motion near the ocean surface is generally lacking, limiting the physical modelling capabilities of the forcing of the world's water surfaces by the atmosphere (Belmonte and Stoffelen, 2019). This also limits our knowledge of the exchange of momentum across the ocean-atmosphere interface, affecting meteorological and ocean applications (Trindade et al., 2019). A particularly pressing requirement in the Ocean Surface Vector Wind (OSVW) community is to obtain reliable extreme winds in hurricanes ( $> 30 \text{ m s}^{-1}$ ) from wind scatterometers, since extreme wind, storm surge and wave forecasts for societal warning are a high priority in nowcasting as well as in Numerical Weather Prediction (NWP).

Scatterometers provide 10-m stress-equivalent winds (de Kloe et al., 2017), with a grid resolution of 12.5 km or 25 km. They have proven to be very effective for wind vector retrieval (Vogelzang et al., 2009). Over the years, improvements have been done on the development of the empirical Geophysical Model Functions (GMFs) in order to obtain more accurate wind estimates with respect to in situ measurements. Scatterometer measurements are then largely used for weather warning and forecasting, climate monitoring, research on processes, ocean forcing and air-sea interaction. Indeed, C-band scatterometers have the capability to provide all-weather measurements, including in extreme wind conditions. However, developing and verifying wind scatterometer processing algorithms for high and extreme winds is challenging, since in situ wind measurements are scarce and they may be hazardous and unreliable. Moreover, theoretical statistical descriptions of the high-wind ocean surface, where patchy foam, droplets, spume and wave breaking occur are much simplified, while the microwave interaction on cm scales is rather complex.

In this framework of the Eumetsat-funded “C-band High and Extreme-Force Speeds (CHEFS)” project, the *Koninklijk Nederlands Meteorologisch Instituut* (KNMI), the *Institut de Ciències del Mar* (ICM-CSIC) and the *Institut Français de Recherche pour l'Exploitation de la MER* (IFREMER) aim at assessing the extreme wind capabilities of the next generation of C-band wind scatterometers on-board Metop Second Generation (SG), in order to provide reliable extreme ocean surface vector winds information in open ocean and marine coastal regions, where generally limited in-situ measurement capability exists. Three main objectives have been proposed in this project: (i) improving the understanding of satellite remote sensing of high-extreme wind conditions over ocean; (ii) the definition of spatial scaling issues and related consequences for product sample resolutions and validations approaches; (i) understanding the **cross-polarization** contribution to the high-extreme winds.

To this end, an important goal within CHEFS is to provide an appropriate and consolidated **high and extreme-wind reference** data set at scatterometer scales, based on in-situ wind references. This reference is crucial for purposes of scatterometer calibration and validation. Moored buoy data are generally used as absolute reference to calibrate the GMFs, however, for very high and extreme winds above  $25 \text{ m s}^{-1}$ , moored buoys may not be reliable. Moreover, controversy exists in the OSVW satellite community on the quality of moored buoys above  $15 \text{ m s}^{-1}$  rather than  $25 \text{ m s}^{-1}$  (e.g., Pineau-Gouillot et al., 2018). Therefore, collaboration has been sought with the Ocean Surface Winds Team (OSWT) at the National Oceanic and Atmospheric Administration (NOAA)/National Environmental Satellite, Data, and Information Service (NESDIS)/Center for Satellite Applications and Research (STAR) (hereafter as NOAA/NESDIS/STAR OSWT) to have additional high and extreme winds reference data sets. The OSWT routinely fly into hurricanes

and extratropical cyclones and deploy GPS drop-wind-sondes (also known as simply dropsondes) obtaining wind profiles. In addition, they operate dedicated microwave instrumentation on the aircraft to obtain detailed wind patterns in hurricanes, such as the Stepped-Frequency Microwave Radiometer (SFMR).

The present report finalizes the CHEFS project. In particular, several wind data sets have been collected, i.e., (i) different types of moored buoy data; (ii) reprocessed SFMR 10-m winds, from 2008 to 2018; (iii) estimated 10-m dropsonde winds, from 2009 to 2018, along with the corresponding raw/quality-controlled wind profiles; (iv) reprocessed ASCAT-A 10-m winds at 12.5 km grid resolution, from 2007 to 2017; (v) the latest European Centre for Medium-Range Weather Forecasts (ECMWF) fifth reanalysis dataset ERA5 from 2007 to 2017, and (vi) Synthetic Aperture Radar (SAR) winds from Sentinel-1 and RadarSat. The collected datasets are discussed in Section 2 of this report. A comprehensive SFMR wind statistical analysis using dropsonde data as reference is presented in Section 3. The impact of the so-called WL150 algorithm used to compute the dropsonde 10-m winds on the SFMR/dropsonde statistics has been also evaluated. An SFMR winds re-calibration has not been performed at this time, but rather suggestions and outliers to be taken into account when comparing dropsonde and SFMR winds are presented. Subsequently, the ASCAT and SAR high-wind performance and calibration are investigated with respect to collocated SFMR winds in Section 4 and 6 respectively. The quality of buoy winds between  $15 \text{ m s}^{-1}$  and  $25 \text{ m s}^{-1}$  is thoroughly evaluated in Section 5. ASCAT surface winds are moreover used as a reliable and stable calibration reference to bridge buoy and SFMR/dropsonde collocations, to allow indirect inter-comparison between such datasets at the scatterometer scale, as sufficient direct collocations of buoy and dropsonde winds were not available. Some conclusions may be drawn from SAR and L-band radiometer (SMAP) comparisons. The inconsistencies between buoy and SFMR/dropsonde winds together with more general conclusions are then discussed in Section 7 and, finally, the recommendations of this study can be found in section 8.

## 2. DATA COLLECTION

### 2.1. SFMR and dropsonde wind data

The SFMR and dropsonde datasets are provided by the NOAA/NESDIS/STAR OSWT. These datasets have been acquired by the many NOAA WP-3D and U.S. Air Force Reserve Command (AFRC) flights over several hurricane seasons. For each flight, the hurricane hunters' aircraft crosses the storm centre several times, acquiring both SFMR sea surface wind and rain along with wind profiles from the Global Positioning System (GPS) dropsondes. An example of the SFMR wind speed variation along a flight trajectory as well as a wind profile from a dropsonde launched from the same flight are shown in Figure 1(a) and Figure 1(b), respectively. As can be seen from the SFMR wind variation, during each storm cross, the wind intensity alternatively goes from high to low speeds and the wind minima usually move during this time, identifying the movement of the storm.

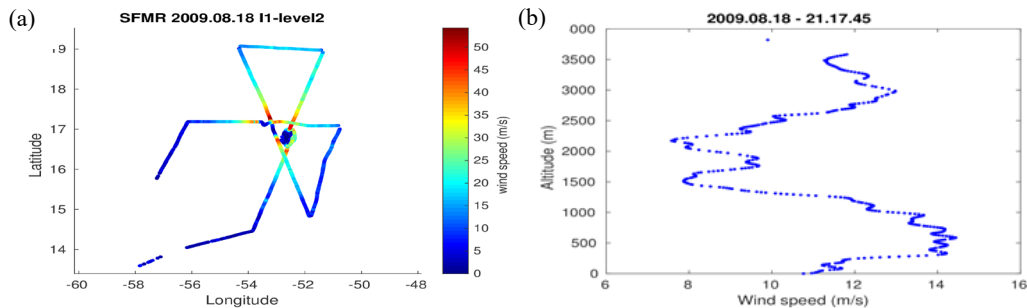


Figure 1. (a) Wind variation during the NOAA hurricane hunters flight experiment on August 18<sup>th</sup>, 2009. Wind data are obtained from SFMR measurements. (b) Dropsonde wind profile acquired from NOAA hurricane hunter during that same flight experiment.

A third dataset is also collected from the Imaging Wind and Rain Airborne Profiler (IWRAP) on-board the NOAA P-3 flights. However, this instrument only operates on a subset of these flights depending on whether or not the instrument space has been provided for the whole hurricane season and whether or not the storm is of interest. Due to the limited data availability, this dataset has not been used in this work. However, it is available for future analysis.

For this study, ten years of SFMR wind and rain retrievals reprocessed by NOAA/NESDIS/STAR OSWT have been collected from 2009 to 2018. These data have been reprocessed using a new GMF that corrects an approximate 10% low bias observed in the SFMR wind retrievals between 15 and 45  $\text{m s}^{-1}$  with respect to dropsondes [Sapp *et al.*, 2019], i.e., the so-called WL150 winds as discussed later. SFMR is a passive nadir-looking instrument that measures the brightness temperature ( $T_B$ ) of the ocean surface at six C-band frequencies. In order to ensure that the  $T_B$  values measured during the flight are accurate, an in-flight ocean calibration is always performed prior to each flight campaign. For each channel, such ocean calibration aims to adjusting few of the instrument internal temperature coefficients forming the  $T_B$  calibration equation, in order to reflect the actual conditions. However, errors in the definition of these calibration coefficients may occasionally occur, leading to differences between the SFMR-measured  $T_B$  values and the corresponding  $T_B$  values predicted by the GMF, i.e., the so-called tuning error. The NOAA/NESDIS/STAR OSWT has developed a  $T_B$  bias correction routine in order to correct for these differences. Such correction is applied to the measured  $T_B$  and the corrected

value is then used in the wind retrieval process. More details can be found in Sapp *et al.* (2019). The SFMR dataset used for the present study has been inspected by the NOAA/NESDIS/STAR OSWT to ensure that they were good in terms of instrument calibration and wind retrievals. In particular, they have excluded those data whose  $T_B$  values was not considered as reliable, because of: (i)  $T_B$  differences amongst the six channels higher than 2K, suggesting possible errors in the  $T_B$  calibration equation; (ii) presence of high amount of noise in the  $T_B$  channels; (iii) possible instrument instability (visible in few SFMR flights of 2008, but which has been fixed since then). As shown in Sapp *et al.* (2019), the standard deviation of the SMFR wind speed error with respect to dropsondes is typically 3-4  $\text{m s}^{-1}$  for wind speed between 15-40  $\text{m s}^{-1}$  in low rain, while biases are below 1  $\text{m s}^{-1}$  with respect to WL150.

The wind retrievals are provided at a frequency of 1 Hz. Note that most NOAA P-3 flights have more accurate geolocation information than AFRC flights. As it can be seen in Figure 2, SFMR data points from the AFRC flight on June 20<sup>th</sup>, 2019 are geolocated at a grid resolution of 0.01 deg. This is because AFRC geolocation (latitude/longitude) information is archived in floating numbers with only two decimals. As such, assuming a flight speed of about 100  $\text{m s}^{-1}$  and an SFMR sampling rate of 1 Hz, about 10 SFMR data points are assigned to the same lat/lon position in AFRC flights. Also, depending on the flight orientation, the SFMR data points are grouped over two apparent parallel tracks, whereas in reality there is only one single track distributed. This leads to a geolocation error of  $\pm 0.005$  deg, which should be taken into account when using AFRC data. Note that the geolocation error is very much reduced in NOAA P-3 flight data, since a higher precision geolocation information (floating-point numbers with four decimals) is kept.

A quality control (QC) flag is available in the wind products in order to discriminate the valid wind solutions from those questionable or invalid.

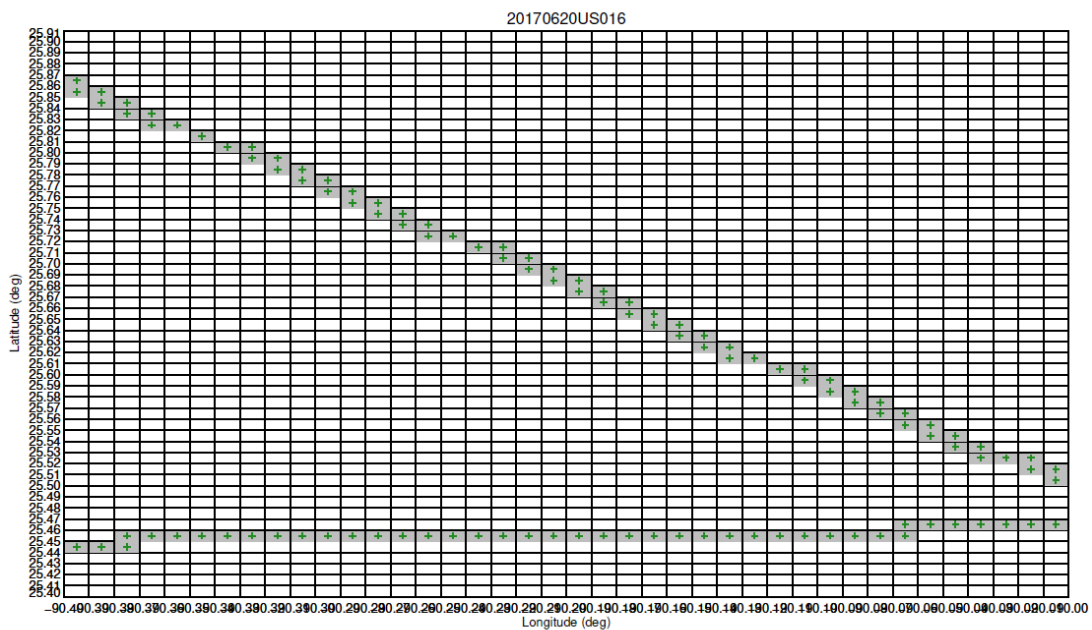


Figure 2. SFMR raw data outlined by boxes, from AFRC flight on June 20<sup>th</sup>, 2017.

GPS dropsondes are launched from the hurricane hunters' aircraft to measure profiles of wind speed, direction, pressure, temperature and relative humidity from the moment they are

launched until they reach the ocean surface (Hock et al., 1999). The dataset used in this analysis covers the period between 2009 and 2018 according to the SFMR dataset. These data have been filtered by the NOAA/NESDIS/STAR OSWT in such a way that only the dropsondes outside the hurricane eyewall and in tropical cyclone conditions have been included. In addition, they refer to dropsondes relevant for SFMR-dropsonde collocation purposes. Details on the criteria used to filter the data can be found in Table 2 of Sapp *et al.*, (2019).

The data have been provided in two different forms: on the one hand, the entire wind profile of each dropsonde and, on the other hand, the corresponding estimated 10-m winds. As it will be discussed in Section 3.2, the dropsonde 10-m winds are estimated by an averaged wind computed from the corresponding wind profile [Franklin *et al.*, 2003, Uhlhorn *et al.*, 2007]. Both the raw and the QC-ed wind profiles have been provided. The latter are obtained by processing the raw profiles using the NCAR's Atmospheric Sounding Processing Environment (ASPEN) software, which systematically detects and removes the incorrect measurements. After exiting the aircraft, the soundings usually undergo an extreme change, so that all the sensors need time before they settle in the new environmental conditions and they start acquiring valid measurements. ASPEN usually filters out these invalid points. Note that the dropsonde profiles of 2018 have been processed with a new release of ASPEN and the output format slightly differs from the previous one. Due to time constraints, the developed data reader could not be adapted, so that the wind profiles of 2018 could not be used at this time and will be included in future analyses.

The time of the first reliable measurement is assigned to the resulting QC-profile as dropsonde launch time and this time may differ from the actual launch time. On the other hand, the actual information of the launch time is generally stored in the raw profiles. As a consequence of such time difference, the SFMR point at the dropsonde launch time stored in the QC-profiles (hereafter as SFMR- $L_{QC}$ ) may be displaced with respect to the SFMR point at the actual launch time (hereafter SFMR- $L_{RAW}$ ). An example is shown in Figure 3. A transect of the SFMR flight on August 25<sup>th</sup>, 2011 is displayed along with the positions of a dropsonde launched during that flight. It can be seen that ASPEN has filtered quite a few dropsonde data points from the raw profiles (black dots). The launch time in the QC-profile is 39 sec apart from the time in the raw profile. This results in a displacement between SFMR- $L_{QC}$  and SFMR- $L_{RAW}$  of about 5.2 km at an aircraft speed of  $133 \text{ m s}^{-1}$ . These time differences are taken into account here when using the launch time for dropsonde/SFMR collocation purposes (see Section 3.1).

A total of 2,174 estimated dropsonde 10-m winds are available. However, 10% of these dropsondes do not have the corresponding QC/raw profile available in our dataset. In addition, 7% of the dropsondes do not have the corresponding SFMR flights, which may have been removed from our dataset because of calibration issues or available wind speeds lower than  $15 \text{ m s}^{-1}$ , where SFMR is not reliable. As such, a total amount of 1,804 dropsonde profiles are used in the dropsonde/SFMR wind comparison. Note that, when carrying out dropsonde wind analysis which does not involve the use of SFMR winds or raw dropsonde profiles, we could enlarge the number of used dropsondes up to 1,983 out of 2,174 available.

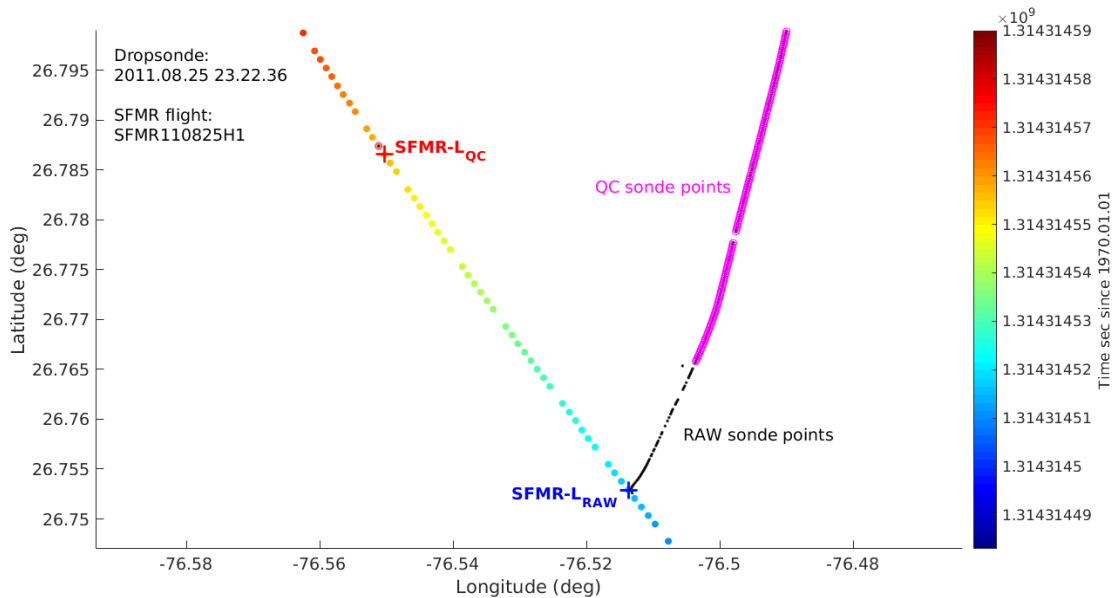


Figure 3. Transect of SFMR data during the NOAA flight on August 25<sup>th</sup>, 2011. Both the raw (black dots) and the QC profile (pink) of a dropsonde launched during the same flight experiment are shown. Both SFMR points at the launch time stored in the QC-profile (red cross) and in the raw profile (blue cross) are outlined.

## 2.2. Synthetic Aperture Radar and L-band radiometer

### Synthetic Aperture Radar

Despite having a single antenna, existing C-band SAR systems can acquire data in both co- and cross-polarization. Consequently, they can provide valuable data before the launch of the Metop-SG scatterometer SCA in order to improve our understanding of the C-band backscattered signal and prepare the mission. In particular,

- its dual-polarization capability allows to directly compare the sensitivity of co- and cross-polarized backscattered signal to ocean surface wind speed and direction but also other phenomena such as intense rainfall that can lead to issues for ocean surface wind retrieval.
- its high resolution allows to analyse the impact of the resolution in order to describe the dynamic of strong but « small » phenomena such as Tropical Cyclones. As a matter of fact, the capability of a sensor to accurately measure the maximum wind speed of a TC is directly related to its spatial resolution and the TC size.

In the following, Sentinel-1 and Radarsat-2 SAR data are introduced for these purposes.

The Sentinel-1 mission (S1) is part of the operational European Copernicus program space component. S1 is a constellation of two satellites (S1-A and S1-B units). Both Sentinel-1A and -1B carry a C-band Synthetic Aperture Radar (SAR) and continue previous European ERS and ENVISAT SAR missions. Sentinel-1A & -1B were launched in April 2014 and 2016 respectively. They have four exclusive imaging modes: Interferometric Wide swath (IW), Extra Wide (EW) swath, Strip Map (SM) and Wave (WV) modes. The IW swath is 250 km wide and covers incidence angles from about 30 to 46 degrees. When processed into Level-1 (L1) GRDH (Ground

Range Detected High resolution), IW Sentinel-1 products have a resolution of about 20 m in range (across-track) and 22 m in azimuth (along-track). The EW swath is 400 km wide and covers incidence angles from about 30 to 46 degrees. When processed into L1 GRDH, EW Sentinel-1 products have a resolution of about 50 m in range (across-track) and 50 m in azimuth (along-track).

Tasking SAR with respect to the hurricane tracks forecast is required to jointly maximize acquisitions over TCs and mitigate the impact on the whole mission acquisition plan. This implies to solve potential conflicts between users regarding the duty cycle along the orbit and the acquisition modes to be used over a given area of interest. Since 2016, ESA set up specific S1 acquisition campaigns to test the instrument capabilities for mapping, at very high resolution, extreme (TC) ocean wind conditions. These campaigns of dedicated acquisitions are named as SHOC, for Satellite Hurricane Observations Campaign. Fully coordinated as for the hurricane watch program approach (Banal et al., 2007), SHOC campaigns help maximizing the number of SAR acquisitions for both Copernicus/ESA Sentinel-1 and MDA Radarsat-2 missions. For this study, the strategy to collect the data over TC includes two different approaches. (i) As part of SHOC, we collect the data through acquisitions requests for both Radarsat-2 and Sentinel-1 missions respectively to MDA and ESA. These requests are based on 5-day forecasts of the hurricane track and satellite orbit. This approach requires great flexibility for data provider. (2) We also analyse the SAR data archives and the maximum wind speed with respect to the hurricane Best-Tracks database to find observations over TC in the past data. The period considered for the archive analysis is from 2015 and 2017. Radarsat-2 data from the archive have been analysed in cooperation with Prof. Biao Zhang from NUIST (Nanjing, China).

To date, SHOC is still on-going. Thanks to this campaign, after the 2018 summer TC season, a total of 194 acquisitions over TC eyes are available, yielding to an unprecedented SAR TC collection over 5 distinct basins. Recently, the first acquisitions of the North Indian Ocean have been obtained.

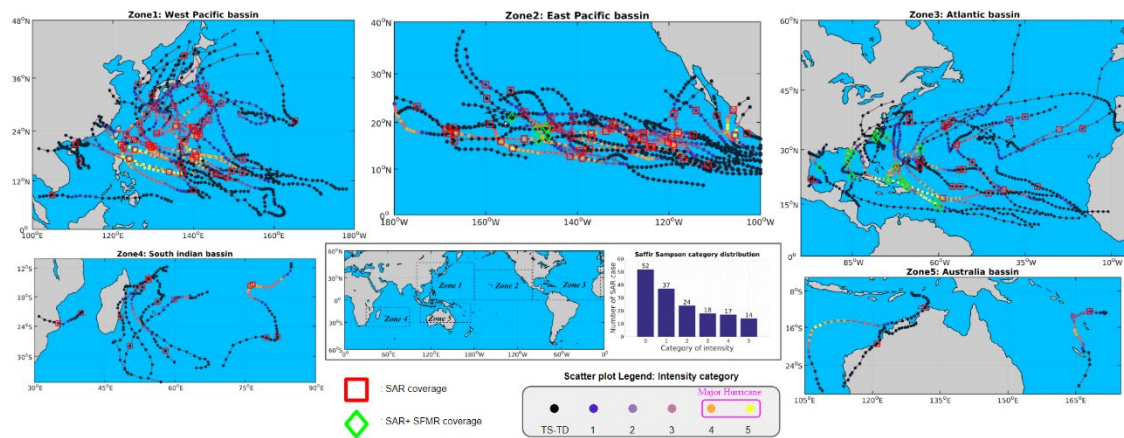


Figure 4. Composite view of TC cases for each geographical zone, where basin locations are indicated in the global map (centre bottom panel). Acquisition positions from Best-Tracks are displayed for each TC, where colours depict intensities with respect to Saffir-Simpson scale. Markers are stated for TC positions with measurements. Red square: SAR measurements only; Green diamond: sequential measurements of SAR and SFMR.

After the filtering steps (partial TC eye for instance), 161 snapshots corresponding to 72 different tropical systems in the period 2015-2018 can thus be analysed. Figure 4 synthesizes the S1 data set. For each storm, the 6-hour Best-Track locations with corresponding storm intensity (colours) are indicated. Specific markers highlight the collocation opportunities: a red square when only SAR is available and a green diamond, when simultaneous SAR+SFMR measurements co-exist. Because aircraft measurements are restricted to North American basins, with a majority in the Atlantic and a few paths in the Eastern Pacific, collocations with SFMR count for only 13% of the data set, with respectively 23 and 6 flights for the Atlantic and East-Pacific. 70% of the Atlantic hurricanes are actually covered. The intensity histogram illustrates the spectrum of TC intensities. Unlike most of the previous SAR-based studies, all Saffir-Simpson scale intensities are sampled.

### L-band Radiometer (SMAP)

Both the VH NRCS and L-band radiometer returns depend on wind speed, with little ancillary sensitivity to wind direction, and are potentially capable of retrieving extreme winds. Hence, it is useful to compare both ocean returns, which is possible by collocating S1 SAR and the NASA Soil Moisture Active Passive (SMAP) L-band radiometer data (<https://smap.jpl.nasa.gov/>).

The L-band radiometer on-board SMAP scans a wide 1000-km swath with a spatial resolution of 40 km. The L-band radiometer measures the four Stokes parameters,  $T_v$ ,  $T_h$ ,  $T_3$ , and  $T_4$ , at a frequency of 1.41 GHz with a surface incidence angle of approximately  $40^\circ$ .  $T_{B,rough}$  is the quantity used in by Reul et al. (2012; 2016), Yueh et al. (2016) and Meissner et al. (2017) to relate ocean surface L-band emission and ocean surface wind speed. In order to estimate  $T_{B,rough}$  from SMAP antenna measurements, radiometer calibration is applied, and several contributions to the antenna temperature are removed or filtered such as radio frequency interferences, extra-terrestrial contributions (galaxy, sun, etc.), and faraday rotation across the ionosphere (Piepmeier et al., 2016). Then atmospheric corrections are performed to estimate brightness temperature emitted by the ocean surface ( $T_{B,surface}$ ). At last, the brightness temperature of the flat ocean surface, a function of the sea surface salinity (SSS) and sea surface temperature (SST), is subtracted from  $T_{B,surface}$  to get the residual brightness temperature  $T_{B,rough}$ . To estimate  $T_{B,surface}$ , we used external monthly SSS from World Ocean Atlas (WOA) 2009 and European Centre for Medium range Weather Forecasting (ECMWF) 3-h forecast SST.

SMAP L-band radiometer can measure the same target from two different azimuth angles, thanks to the rotating scan of the antenna.  $T_{Bh,rough}$  and  $T_{Bv,rough}$  measured forward and afterward of the SMAP satellite position are averaged to reduce directional variation. In this report, we consider the first Stokes parameter  $(T_{Bh,rough} + T_{Bv,rough})/2.0$  for analysis against Sentinel-1 NRCS. The spatial resolution of original NASA level 1B SMAP data is about 40 km, while the reprocessed SMAP product used here is mapped onto a global grid with spatial resolution of  $0.25^\circ$ .

To perform accurate analysis of Sentinel-1 NRCS and SMAP  $T_{B,rough}$ , we collocate SMAP  $T_{B,rough}$  with Sentinel-1 NRCS, and IMERG rain rate (rain product from NASA) as illustrated in Figure 5. For spatial collocation, the Sentinel-1 NRCS pixels located in the same SMAP grid are arithmetically averaged (in linear scale) to obtain a match up with SMAP  $T_{B,rough}$  on the same grid. We note that the aggregated SMAP footprints have substantial extensions outside their grid box, as the product is oversampled. On the other hand, a box-car filter of width  $L$ , has an effective resolution of  $L/(2\sqrt{3})$  and as such the Sentinel-1 product is still higher resolution than SMAP by about a factor of 3. Considering the spatial grid of the pre-processed Sentinel-1 NRCS and the

SMAP grid size, one pixel on the SMAP grid can contain up to 2,500 Sentinel-1 pixels. Grids with less than 1,300 valid Sentinel-1 pixels are excluded. The same processing is applied to the IMERG rain rate data. For temporal collocation, the time difference between Sentinel-1 sensing and SMAP measuring is constrained to be less than 60 min, and IMERG data is interpolated to the SMAP measurement time. Finally, we obtain 210 collocations for Sentinel-1 EW and SMAP observations.

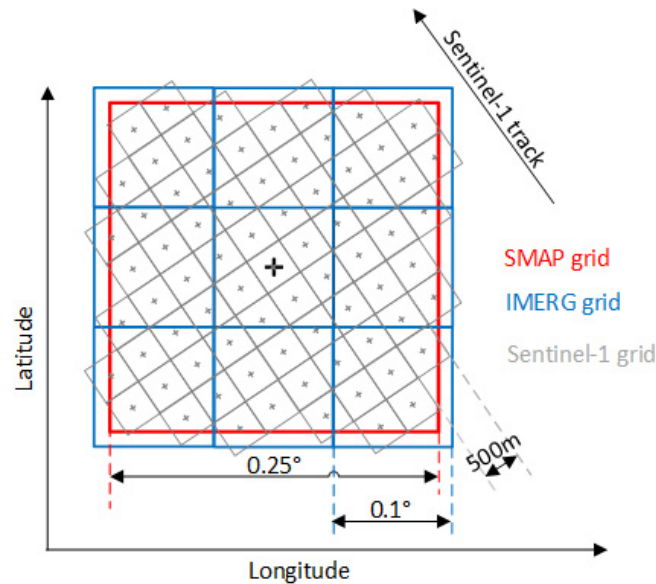


Figure 5: Sketch for illustrating the collocation of Sentinel-1 NRCS, SMAP  $T_{B,rough}$ , and IMERG rain rate.

### 2.3. ASCAT wind products reprocessed with ERA5 model winds

The latest version of the reprocessed 12.5 km ASCAT-A wind data products have been provided by the EUMETSAT Ocean and Sea Ice Satellite Application Facility (OSI SAF) team. In order to have a consistently reprocessed dataset, the ASCAT wind data have been reprocessed with the recently available ECMWF fifth Re-Analysis (ERA5) (Hersbach and Dee, 2016) model winds, in full resolution (Copernicus Climate Change Service (C3S), 2017).

The ERA5 dataset was produced using Cycle 41R2 of the ECMWF Integrated Forecast system (IFS) and it covers the period from 1979 to 2-3 months before the present time. The horizontal grid resolution is 31 km globally, with 137 pressure levels in the vertical up to 0.01 hPa. The data consist of analyses and forecasts, initialised twice daily from the analyses at 06 and 18 UTC. With respect to the operational ECMWF model winds, ERA5 has been processed with one of the latest versions of the IFS, albeit at lower grid spacing. Unlike ERA-Interim and the operational ECMWF runs, it provides hourly forecasts for the whole period of time. Note that only 3-hourly forecasts are available from ECMWF at a grid spacing comparable to ERA5 before November 16<sup>th</sup>, 2011. ERA-Interim has the coarsest grid spacing. Under hurricane conditions, hourly forecasts are more suitable than 3-hourly forecasts since they provide a more precise location of the storm eyewall and centre at the scatterometer overpass time.

The hourly ERA5 10-m equivalent neutral winds have been downloaded through the ECMWF Meteorological Archival and Retrieval System (MARS). The stress-equivalent winds [De Kloe *et al.*, 2017] have not been used at this stage, due to the downloading time of the ERA5 parameter

GRIB files needed to carry out the stress-equivalent wind conversion. This causes a systematic overestimation of the ERA5 wind by about 10% at 920 mb mean sea level pressure and which error is about linear with 0% error at 1013 mb; see Figure 7). We have then used spatially and temporally interpolated ERA5 neutral winds to carry out the reprocessing of eleven years of the 12.5 km ASCAT-A data from 2007 to 2017, by using the ASCAT Wind Data Processor (AWDP) version 3.2. Three subsequent ERA5 forecast fields around the ASCAT acquisition time are used by AWDP to perform the interpolation, two forecast fields corresponding to UTC times before the ASCAT observing time and one after. Each of the three selected ERA5 forecasts is spatially interpolated to each ASCAT WVC position. Then, a time interpolation of the three forecasts to the ASCAT acquisition time is performed to get the final collocated ERA5 wind vector components (Verhoef and Stoffelen, 2019; Lin *et al.*, 2016).

## 2.4. Buoy wind description

The buoys used in this study include the National Data Buoy Center (NDBC) moored buoys off the coasts of U.S.A., the Ocean Data Acquisition System (ODAS) buoys in the north-east Atlantic and British Isles inshore waters, the National Oceanic Atmospheric Administration (NOAA) Tropical Ocean Atmosphere (TAO) buoy arrays in the tropical Pacific, the Japan Agency for Marine-Earth Science and Technology (JAMSTEC) Triangle Trans-Ocean Buoy Network (TRITON) buoys in the western Pacific, the Prediction and Research Moored Array in the Atlantic (PIRATA), and the Research Moored Array for African–Asian–Australian Monsoon Analysis and Prediction (RAMA) at the tropical Indian Ocean.

Two different buoy data sets are freely available to the users. The first data set consists of buoy winds that hourly report an averaged wind over 10 minutes, distributed through the Global Telecommunication System (GTS) stream, and quality controlled and archived at ECMWF Meteorological Archival and Retrieval System (MARS). Such buoy data are hereafter referred to as MARS buoy winds. Note that the MARS buoy winds are binned every  $1 \text{ m s}^{-1}$  in speed and  $10^\circ$  in direction bins. The second data set consists of continuous 10-minute (10-min) buoy wind measurements, further referred to as continuous buoy winds (Cwinds). This data set is obtained from <http://www.pmel.noaa.gov/>, while it does not contain ODAS and TRITON continuous buoy winds. In both buoy data sets, the measured wind vectors at a given anemometer height are converted to 10-m equivalent neutral winds,  $U_{10N}$ , using the Liu-Katsaros-Businger (LKB) model (Liu *et al.*, 1979) in order to make them more comparable to ASCAT and ECMWF winds. This also causes a systematic overestimation of the buoy  $U_{10N}$  winds by about 10% at 920 mb mean sea level pressure as compared to the ASCAT stress-equivalent winds,  $U_{10S}$ , as explained in next section.

## 2.5. Effect of Stress-Equivalent Reference Winds

Active remote sensing systems like scatterometers and SARs measure the backscattered signals from the ocean surface. This backscatter is mainly influenced by the ocean surface roughness, which is directly related to surface wind stress and not to just the standard 10-m winds only (de Kloe *et al.* 2017). For validation purposes, the direct retrieval of winds from scatterometers and SARs is therefore at odds with the World meteorological Organization (WMO) standard 10-m winds coming from the moored buoys or numerical weather models.

For scatterometers, the backscatter has always been related to the wind vector at 10 m ( $U_{10}$ ) using a geophysical model function (GMF). As the ocean-modulated scattering with respect to

wind speed and direction is extremely complex, this GMF is derived empirically, by comparing a large amount of scatterometer data with corresponding buoy and Numerical weather prediction (NWP) model data, combined with additional measurements. In the newest version of the European organisation for exploitation of Meteorological Satellites (EUMETSAT) Ocean and Sea Ice Satellite Application Facility (OSI SAF) Geophysical Model Function (GMF) for C-band scatterometry, called CMOD7, is related to the stress equivalent wind ( $U_{10S}$ ), hence avoiding implicit dependencies on air mass stability and air mass density, which do not relate to the ocean surface as sensed by a satellite instrument.

The conversion from  $U_{10}$  to  $U_{10S}$  for NWP and buoy winds is performed in two steps, first relating the  $U_{10}$  to the equivalent-neutral wind ( $U_{10N}$ ) and subsequently to  $U_{10S}$ .  $U_{10S}$  is physically more consistent with satellite winds and a better resource for comparison. In the  $U_{10N}$  conversion process the  $U_{10}$  wind is transformed to the near surface wind using a realistic surface layer wind profile, estimated from local buoy measurements or NWP model parameters, respectively, and then translated to 10 m again using an average (neutral) wind profile in order to make the satellite wind comparisons independent of the local atmospheric stability conditions (Liu *et al.*, 1979). The  $U_{10N}$  can subsequently be converted to  $U_{10S}$  by correcting the corresponding surface wind stress for actual air mass density (as defined by the NWP model), in order to be representative of the generation of the cm-scale roughness by air–sea momentum exchange. Subsequently, it is rescaled with the global average air mass density, and scaled back again to 10 m, using the same surface layer wind profile as in the first step.

The conversion between the two derived 10-m winds has the shape of (de Kloe *et al.*, 2017):

$$U_{10S} = U_{10N} \left( \frac{\rho_{air}}{\langle \rho_{air} \rangle} \right)^{1/2}$$

In Section 5.4 results from 32 observed tropical cyclones SAR images are discussed. For each of these observations the ECMWF forecast has been collocated, i.e., the observed cyclones eye matches the lowest pressure and velocity structure within the model, and interpolated in space with the SAR image. For this the closest forecast result in time to the Sentinel 1a or 1b has been used since interpolation in time has a tendency of stretching and deforming modelled tropical cyclones.

In Figure 6 and Figure 7 the conversions between  $U_{10N}$  to  $U_{10S}$  and  $U_{10}$  to  $U_{10S}$  are respectively shown. Note that this is based on the ECMWF model data where no observations have been included here and that it only includes wind information relatively close to the cyclone.

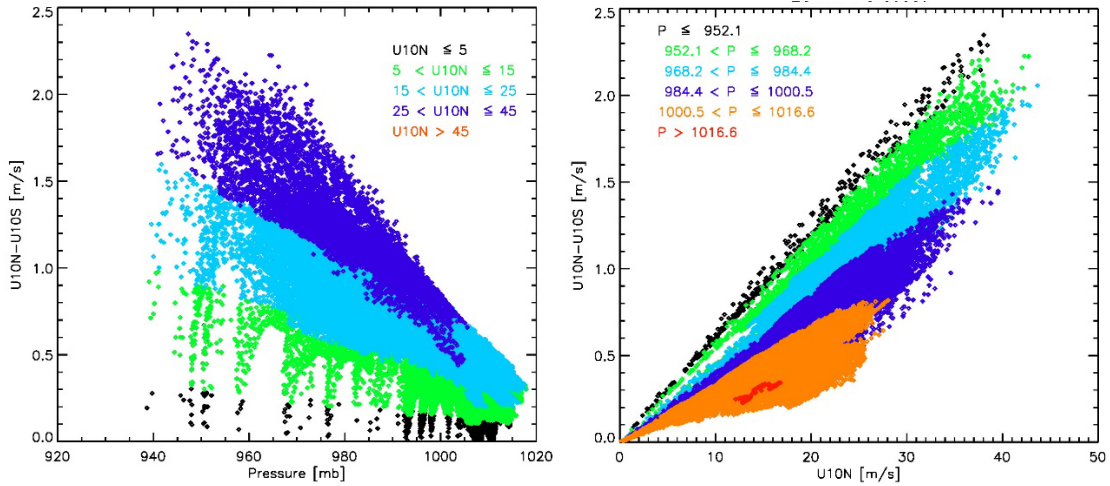


Figure 6. The difference between  $U_{10N}$  and  $U_{10S}$  with respect to surface pressure (left panel) and  $U_{10N}$  (right panel). Color coded are different wind speed regimes (left) and surface pressures (right)

In both figures the conversion is plotted in two manners, the left panel shows the difference in wind speed with respect to surface pressure and color coded for different wind speed regimes, the right panel shows the same information but now the wind speed difference with  $U_{10N}$  and  $U_{10}$  respectively, where the color code shows the surface pressure. The arcs on the lower side in the left panel indicates the minimum pressure of the individual cyclone centers.

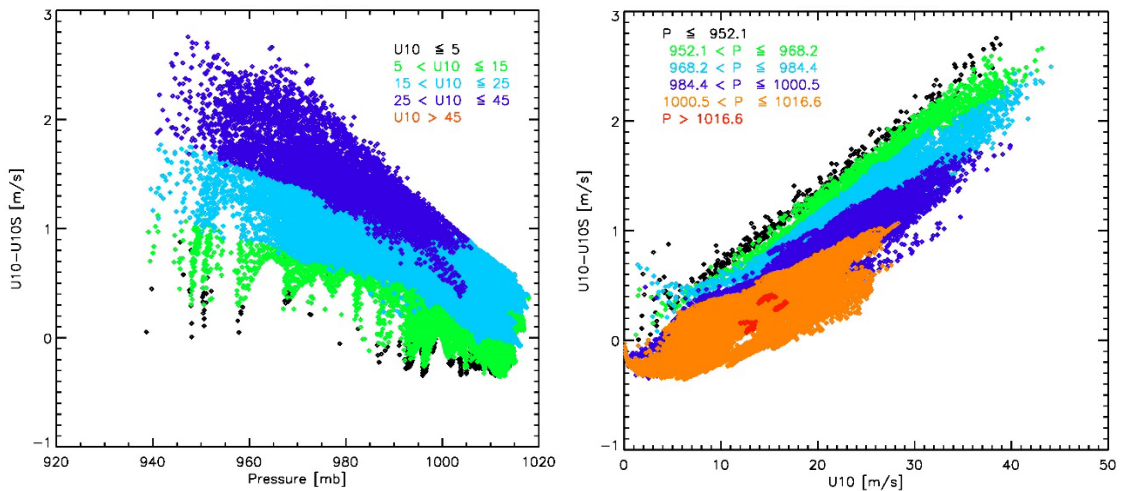


Figure 7. The difference between  $U_{10}$  and  $U_{10S}$  with respect to surface pressure (left panel) and  $U_{10}$  (right panel). Color coded are different wind speed regimes (left) and surface pressure (right).

From the figures it can be concluded that  $U_{10S}$  is always smaller than both  $U_{10N}$  and  $U_{10}$  for extreme wind speeds ( $U_{10} > 25 \text{ m s}^{-1}$ ), which can have an absolute difference up to  $\sim 2.5 \text{ m s}^{-1}$  for extreme winds. The relative error is more similar for the different wind speeds. There is a clear dependence with surface pressure, which is a proxy to air density. For low wind speeds and high surface pressures  $U_{10}$  can be smaller than  $U_{10S}$ .

The results presented above show that when constructing a consolidated high and extreme wind reference based on active remote sensing (SFMR, SAR, scatterometers) there is need to take into account the difference between  $U_{10}$  (the standard value) and  $U_{10S}$  (more closely related to

the measurements). By using  $U_{10S}$  as the GMF retrieved parameter with a subsequent conversion to  $U_{10}$  one can ensure not only lower error estimates, but also reduce the introduction of a wind speed and pressure biased result for in particular the extreme winds at low pressures.

## 2.6. Summary

Several collocation data sets have been prepared from hurricane data and are described here, where so-called storm-motion centric coordinates have been used. The dropsondes and the buoys provide our in-situ references, while SFMR has been calibrated to dropsondes. The model (ERA5) and satellite complements (S1, RadarSAT, ASCAT, SMAP) have different calibrations and different spatial aggregations as described here. Multiple spatial samples are allowed in order to be able to investigate spatial scaling effects in hurricanes.

In CHEFS it has been planned to use equivalent neutral winds,  $U_{10N}$ , for collocation for ERA5 and buoy winds. An investigation of the differences between  $U_{10N}$  and stress-equivalent winds,  $U_{10S}$ , reveals an important effect of the air mass density, which can be substantially reduced close to the centre of a hurricane, leading to 5% lower stress-equivalent winds (i.e., reduced impact on the water surface) than the real winds at 10m height. This effect needs to be accounted for in the results on scatterometer, SAR, SFMR and SMAP  $U_{10S}$  and dropsonde, buoy and ERA5  $U_{10N}$ .

### 3. SFMR CAL/VAL USING DROPSONDES

In this Section, a comprehensive SFMR wind calibration analysis is presented using dropsonde data as reference. In Section 3.1, the SFMR/dropsonde collocation criterion is defined. In Section 3.2, the so-called WL150 algorithm used to estimate 10-m surface winds from dropsonde wind profiles is revised and its impact on the SFMR calibration process is tested. The results are presented and discussed in Section 3.3.

#### 3.1. SFMR/dropsonde collocation procedure

The SFMR surface wind measurement at the dropsonde launch time stored in the raw profile data is selected to be compared against the dropsonde-derived surface wind. Although the dropsonde position at the surface is generally horizontally displaced with respect to the launch location, such displacement is generally in the azimuthal direction, while the storm wind gradient mostly changes in the radial direction with respect to the storm centre. Therefore, by pairing SFMR and dropsonde surface winds at the dropsonde launch time, one can assume that both sensors are in general observing similar wind conditions (see Figure 8).

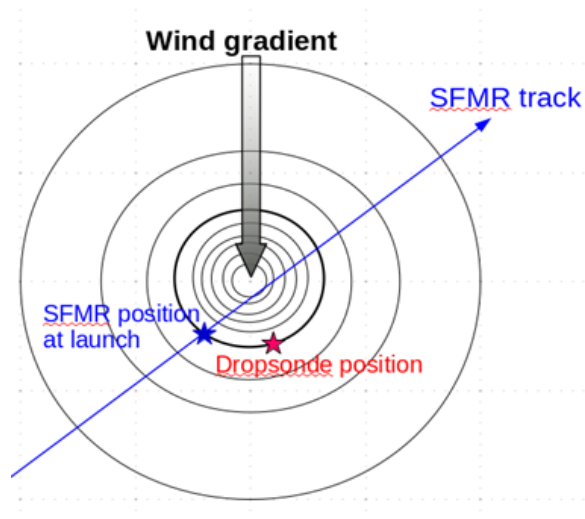


Figure 8. Schematics of the dropsonde displacement after launch with respect to the SFMR position at launch time and to the wind gradient change. The grey scale goes from lower (light grey) to higher (dark grey) wind intensities.

The dropsonde wind profile files contain the sounding description including the name of the aircraft from which they have been launched. Such information is compared to the aircraft identification name stored in a field of the SFMR data files called platform ID, in order to identify the SFMR-sonde flight. This check of the platform name is needed since more than one storm may simultaneously occur over different locations, such that more than one aircraft may be flying at the same day and time. However, for the AFRC flights, the sounding description and the SFMR platform ID use different ways of naming the aircraft, so that the correspondence is not straightforward. For this reason, in this work the following two criteria are used to pair the dropsonde/SFMR surface winds:

- 1) When the SFMR platform ID and the flight identification available in the sounding description match, the SFMR wind measurement whose time ( $t_{SFMR}$ ) meets the following condition is selected:

$$\Delta t = |t_{SFMR} - t_{launch}| \leq 1 \text{ second} \quad (1)$$

where  $t_{launch}$  is the dropsonde launch time. Note that since SFMR sampling rate is 1 second and that the dropsonde time information is rounded to the nearest second, a  $\Delta t$  of 0 seconds should suffice. However, since that particular SFMR wind observation may be missing or QC-rejected, the collocation procedure allows the selection of the previous or consecutive SFMR measurement (i.e., at  $\pm 1$  second distance from  $t_{launch}$ ), whichever is valid.

- 2) When the SFMR platform ID and the dropsonde flight identification do not match, an additional condition on the spatial distance is included in order to identify the corresponding SFMR platform, such that:

$$\Delta d = |d_{SFMR} - d_{launch}| \leq 10 \text{ km} \quad (2)$$

where  $d_{SFMR}$  is the position of the selected SFMR point and  $d_{launch}$  is the dropsonde position corresponding to zero seconds after launch. The seconds-after-launch value is stored in the dropsonde profile as a variable called  $time_{offset}$ . When the dropsonde position at  $time_{offset} = 0 \text{ s}$  is not available,  $d_{launch}$  corresponds to the first available position at  $time_{offset} > 0 \text{ s}$ .

Hereafter, we refer to the SFMR wind at launch time as SFMR-L. A total of 1797 dropsondes have been collocated with SFMR. 31% of these collocations have been obtained by using the condition shown in Eq. 2, since the SFMR platform ID and the dropsonde flight identification do not match.

### 3.2. Dropsonde winds

As pointed out in the CHEFS project proposal, an inconsistency exists between moored buoy and dropsonde in-situ winds, preventing the calibration of satellite winds and NWP models to a consolidated in-situ reference. Hence, for CHEFS the question emerges what observation of the dropsonde should be used for wind calibration? Going back to Hock and Franklin (1999), we note that the dropsonde-computed 10-m wind is actually unbiased and accurate within  $\sim 1 \text{ m s}^{-1}$ , which is really excellent for extreme winds (cf. their Figure 9). The correction for deceleration in the lowest layers of descent appears to work quite well and one can convert the sonde speed to wind speed by taking account of a deceleration term. The measured sonde 10-m wind thus appears a good candidate as calibration reference.

Hock and Franklin (1999) show a few typical dropsonde acquisitions in two hurricanes (their Figure 13), with  $10 \text{ m s}^{-1}$  wind variability in the lowest few 100 m, both in amplitude and structure. Later on, Franklin et al. (2003) indicate nevertheless that wind dissipation due to drag in a log profile near the surface appears a good general assumption at extreme winds. On the other hand, to motivate the introduction of the WL150 estimation algorithm for operational maximum 1-minute-sustained 10-m wind estimation, Uhlhorn et al. (2007) state: "Improvements to the GPS drop-wind-sonde have increased the availability of 10-m wind speed measurements. However, this single instantaneous measurement may be interpreted as containing 'gustiness', and is not necessarily representative of the 1-min average, 10-m wind speed required for operation". Although a clear proof for this statement is not provided, one expects indeed local downdrafts, vertical motions and waves affect wind variability near the

surface at all lower levels, cf. Figure 13 of Hock and Franklin (1999). However, irrespective of operational application considerations, the question remains, what is the 10-m wind representative of and how to obtain a locally unbiased estimate useful for satellite and NWP model calibration?

Averaging over 150 m in the vertical may be equivalent to averaging at 10-m over 1 minute, but how do we know this? How can this be tested? We note at this point that we are not per se interested in representing 1-minute 10-m winds when calibrating remote-sensing data.

The instantaneous dropsonde 10-m wind may be a better understood reference for a local calibration of the SFMR instrument, rather than an estimate depending on the lowest 150 m of the wind profile. The wave boundary layer (WBL) is a first concern in estimating 10-m winds. In fact, in hurricane conditions, waves reach 10 m height. The WBL will distort the notion of a logarithmic profile. Nevertheless, using available campaign data, Edson et al. (2013) investigated wave age- and wave slope-dependent parameterizations of the surface roughness up to  $25 \text{ m s}^{-1}$ , where their COARE 3.5 wind speed-dependent formulation matches the observations well without any wave information. Their available data indicate that wind speed-, wave age-, and wave slope-dependent formulations give similar results, since the inverse wave age varies nearly linearly with wind speed in long-fetch conditions for wind speeds up to  $25 \text{ m s}^{-1}$ . See also Potter et al. (2015). This assessment has been corroborated by mast measurements over waves, indeed resulting in a logarithmic drag profile over many waves. Ergo, there could be noise, but no indication of systematic (calibration) effects. In addition, the 10-m wind of a dropsonde is not really an instantaneous value. The deceleration in the lowest 10s of meters by drag acts like a vertical integration of the wind variability. The speed of the sonde at 10 m for  $30 \text{ m s}^{-1}$  wind is equal to the wind at about 20 m for a standard wind profile at 10 m, which lag suggests an effective vertical integration of about 10 m. Since acceleration is used to correct the 10-m wind speed, the error in estimating the 10-m wind from the sonde speed and deceleration may be systematic, but nevertheless quite small (Hock and Franklin, 1999). The vertical smearing will however reduce the noise due to the wave boundary layer and hence reduce the perceived "gustiness".

The coupled wind-wave processes that are thought to be important under extreme wind conditions (i.e., wind speeds greater than  $25 \text{ m s}^{-1}$ ) are poorly understood due to the scarcity of measurements under these conditions. These processes include wave breaking, flow separation, bubble production and generation and transport of evaporating sea-spray, all of which impact the momentum, heat and energy exchange under these conditions. Being mostly supported by short waves (with wavelength of the order of cm to meters), these processes mostly act on a shallow atmospheric layer of one order of magnitude smaller than these wavelengths. This results in a height of the WBL of the order of 5 m the absence of swell (Ayet et al., 2019).

Foster and Fairall (2015) investigated Monin-Obukhov (M-O) similarity signatures in dropsonde profiles. They found in the lowest 40 or 50 m, that reasonable M-O solutions could be fit to the individual profiles. Sometimes the fits are essentially perfect, while at other times there are systematic deviations. However, the deviations are such that positive wind perturbations correlate with negative humidity deviations. This may be interpreted as sampling over-turning near-surface eddies. The idea is that slower wind speeds are associated with momentum ejections, which in turn are associated with converging flow that, being closer to the sea surface and uplifted, tends to be closer to saturation. Conversely, higher wind speeds are associated with momentum sweeps, which bring lower humidity air toward the surface. Perhaps, these

variations could be associated with swell and ocean wave phase (Ralph Foster, personal communication).

The questions addressed in this report are: should we not be using the derived sonde 10-m winds for 10-m wind calibration of SFMR, rather than WL150 and what difference would it make?

Another open question is related to the fundamental measurements of the dropsonde, i.e., the position measurement, which is proprietary information of the GPS manufacturers. The basic techniques are using Kalman filters, but how they are implemented along with anti-spoofing and multipath algorithms is unknown. Since the dropsonde is increasingly decelerated along its path towards the ocean surface, the position filtering could have systematic effects on position, hence on speed and acceleration of the sonde, which are used to determine the 10-m wind. Detailed information from manufacturers appears essential to understand possible errors (error propagation modelling is needed).

### 3.3. Analysis of the WL150 dropsonde winds

A dropsonde may not report winds at an altitude of 10 m and even if it does, such instantaneous measurement may be affected by wind gust, large ocean waves and altitude estimation errors, as mentioned above. For this reason, a layer-averaged wind is usually computed in order to estimate the maximum 1-minute-sustained 10-m winds. Evaluating the algorithms used to estimate the dropsonde surface wind is crucial since such winds are then used as reference in the SFMR calibration process and it may play a role in the SFMR-dropsonde wind comparison.

The NOAA/NESDIS/STAR OSWT estimates dropsonde surface winds using the WL150 algorithm with an altitude-scaling factor applied. The WL150 wind is an altitude-weighted average of the dropsonde wind speeds over the lowest 150 m layer from 10 m to 350 m. Its zonal ( $u_{L150}$ ) and meridional ( $v_{L150}$ ) wind components are computed as follows:

$$u_{L150} = \frac{\sum_{i=1}^n u_i w_i}{h_n - h_1} \quad (3)$$

$$v_{L150} = \frac{\sum_{i=1}^n v_i w_i}{h_n - h_1} \quad (4)$$

Where  $n$  is the number of wind samples in the 150m-layer,  $u_i$  and  $v_i$  are the zonal and meridional components of the wind sample, respectively, and  $w_i$  is the altitude weight, assuming a continuous distribution of the wind samples, such that:

$$w_1 = \frac{h_2 - h_1}{2}; \quad w_n = \frac{h_n - h_{n-1}}{2}; \quad (5)$$

$$w_i = \left[ \left( \frac{h_{i+1} - h_i}{2} + h_i \right) - \left( \frac{h_i - h_{i-1}}{2} + h_{i-1} \right) \right]; \quad i = 2, \dots, n-1 \quad (6)$$

As described in Sapp *et al.* (2019), according to their processing, each wind component is then scaled to the surface by using a correction factor of 0.85 as suggested in the equation given in Uhlhorn *et al.* (2007), as follows:

$$u_{10_{WL}} = 0.85u_{L150} + 0.89 \quad (7)$$

$$v_{10_{WL}} = 0.85v_{L150} + 0.89 \quad (8)$$

In collaboration with NOAA/NESDIS/STAR OSWT, ICM implemented and tested the WL150 algorithm. As an independent check of the equation given in Uhlhorn *et al.* (2007), the collected dropsonde QC profiles have been used to compute the WL150 wind in order to verify the 0.85 scaling factor. To this end, a subset in which the lowest reading (LR) within the layer ranges between 10 m and 15 m, has been used to compute the WL150 wind in nominal conditions ( $WL150_N$ ), with layer width between 140 m to 150 m. Note that, using only LR at 10 m height significantly reduces the number of points, and for this reason, we have decided to include readings up to 15 m.

The WL150 wind speed has been compared to the LR surface wind speed ( $U_{10_{LR}}$ ). The regression line in Figure 9 indicates that, for this data set, the  $U_{10_{LR}}/WL150_N$  wind speed ratio is 0.86. Such value is consistent with the value of 0.85 from Uhlhorn *et al.* (2007), as it is within the accuracy range of the regression line slope reported in Fig. 3 of their work.

We have also carried out a simple test on the WL150 scaling factor using a dropsonde logarithmic wind profile in neutral stability conditions and judge the above correlation value rather high. We have modelled the lowest 150-m-layer using 6 dropsonde readings at 10 m, 15 m, 45 m, 75 m, 105 m and 135 m, respectively. We have assumed a logarithmic profile in two different conditions, such as: (a) surface roughness length  $z_0 = 5$  mm and friction velocity  $u^* = 1.58$  m s<sup>-1</sup> and (b)  $z_0 = 1$  mm and  $u^* = 1.3$  m s<sup>-1</sup>. These values are typical values in hurricane conditions and they lead to  $U_{10_{LR}} = 30$  m s<sup>-1</sup>. We have computed the wind weights according to Eqns. (5) and (6) and applied those values to the wind speeds rather than to the wind components in order to compute the corresponding  $WL150_N$ . The results show that, the ratio  $U_{10_{LR}}/WL150_N$  is 0.81 and 0.84 when using a logarithmic profile with configuration (a) and (b), respectively. If scaling the  $WL150_N$  wind to a wind speed at 15 m the corresponding ratio is 0.85 and 0.87 for (a) and (b) respectively. This suggests that using a correction of 0.85 would imply a scaling to a wind speed at 15 m rather than 10 m, so a 5 m height error. Further investigations are certainly needed to better understand these differences. However, these preliminary results show that the estimate of the 10-m winds from dropsonde measurements is sensitive to the height. Hence, height knowledge may affect Figure 9 and GPS position, speed and acceleration processing appear quite critical for using dropsondes as an in-situ reference.

Finally, if a dropsonde gusty wind profile is averaged and scaled into WL150, then this wind should generally be less extreme than the gusty 10-m wind, as averaging in time or space has the effect of removing extremes from a PDF. Rescaling the expected wind to an instantaneous value will in principle not restore the instantaneous PDF, while this will be necessary to interpret the real wind field for calibration purposes.

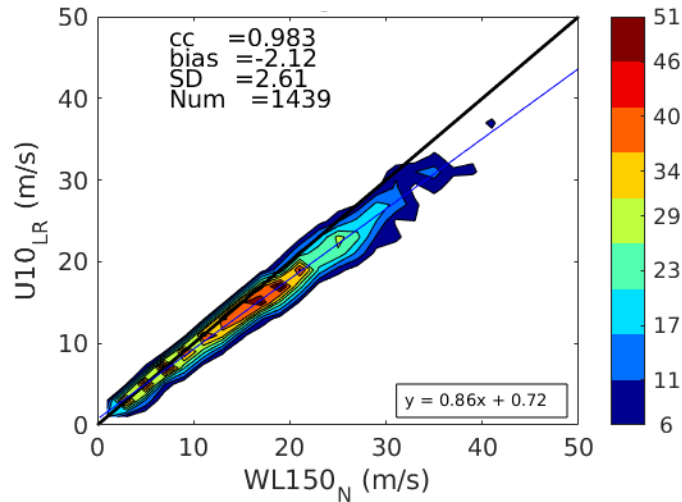


Figure 9. Two dimensional histogram of the surface winds as measured by the dropsonde ( $U10_{LR}$ ) versus the  $WL150_N$  wind speed computed in nominal conditions, i.e., where the lowest reading available within the layer ranges between 10-15 m altitude and the layer mean altitude ranges between 80-90 m. The Pearson correlation coefficient ( $cc$ ), bias, standard deviation ( $SD$ ), and number of points ( $Num$ ) can be found in the legend. The corresponding linear fit is also shown at the bottom right side of the plot.

### 3.4. SFMR and dropsonde wind comparisons

In this Section, the impact of two main parameters in the  $WL150$  wind computation, i.e., the layer mean altitude and the layer widths, on the SFMR comparisons is investigated. In particular, the  $WL150$  winds are re-computed by averaging the dropsonde readings over 150-m layers at different altitudes, as well as by modifying the layer width from its nominal 150 m. The new averaged winds are then compared with the corresponding  $WL150_N$  as well as with the collocated SFMR winds. Changing the altitude of the 150-m layer is intended to simulate dropsondes that fail at different heights above the surface, while averaging the dropsonde wind measurements over different layer widths is intended to verify if the winds averaged over smaller layers close to the surface are more representative of SFMR sea surface wind measurements.

To check the impact of the altitude variation of the 150-m layer, the  $WL150$  wind has been re-computed by moving the minimum height of the layer ( $z_{min}$ ) starting from 50 m ( $WL150_{50}$ ) to 200 m ( $WL150_{200}$ ) with a step of 50 m. These winds are then compared to the corresponding  $WL150_N$ . Note that those dropsondes which do not have at least five readings within each layer and a layer width of at least 100 m have been a priori discarded from the analysis, hence the sample (number) is fixed. As shown in the two-dimensional scatter plots of Figure 10, the scaling factor increases with the altitude as well as both the bias and the standard deviation ( $SD$ ) of the difference. This change in the scaling factor and bias is expected, since close to the surface, the winds tend to increase with altitude (see, e.g., Figure 1). It is clear that the winds at the higher altitudes do not well represent the 10-m wind, as the  $SD$  increases substantially (factor 3 or a factor 10 in variance) from a) to d).

This analysis has been also performed by comparing the averaged  $WL150$  winds against the collocated QC-accepted SFMR 10 m surface wind speed, as shown in Figure 11.

In nominal conditions, the  $WL150_N$  and the SFMR-L winds are well correlated. As expected, the  $WL150_N$  winds are higher than the collocated SFMR-L, due to the fact that the correction factor is not used here to convert the dropsonde averaged winds into surface winds. When moving towards higher altitudes, although the correlation is still good, the mean bias increases from  $2.27 \text{ m s}^{-1}$  at  $z_{min} = 10\text{-}15 \text{ m}$  to  $4.28 \text{ m s}^{-1}$  at  $z_{min} = 200 \text{ m}$ , showing that the dropsondes catch higher winds at higher altitudes. A slight increase of the SD is also seen, in line with a variance increase of  $6.7 \text{ m}^2 \text{ s}^{-2}$ , which corresponds closely with the variance ( $SD^2$ ) of Figure 10 d), although computed for a different weather sample. Moreover, the mean bias is not constant, but rather scales with the wind speed, as also shown in the Figure 10 fits.

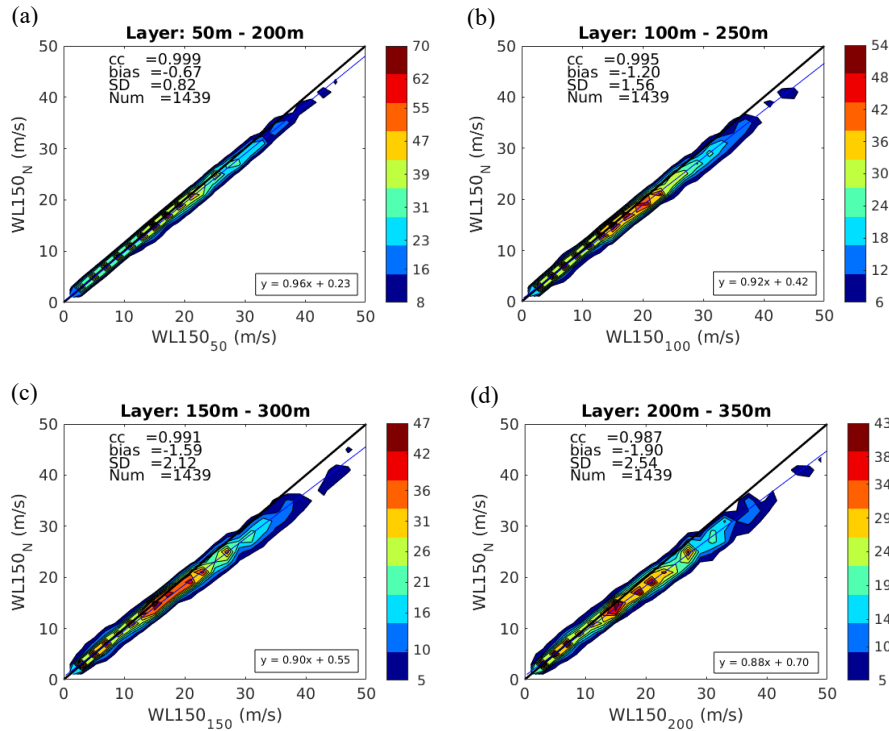


Figure 10. Two dimensional histograms of the dropsonde  $WL150$  at different 150-m layer altitudes versus their corresponding  $WL150_N$  (see colourbar). The 150-m layer is placed at 50-200m (a), 100-250m (b), 150-300m (c) 200-350m (d). The same statistical parameters as in Figure 9 can be found in the legend. The corresponding linear fit is also shown at the bottom right side of each plot.

These results show that the scaling factor used to process the dropsonde surface winds should not be independent on the layer altitude, as it has been done so far in the dropsonde reprocessing. No significant changes in the results are expected though when using the present dropsonde data set, since the vast majority of the dropsonde profiles have the lowest available reading around 10 m altitude. However, we suggest to account for the layer altitude for future processing.

Indeed, according to Uhlhorn *et al.*, (2007), we have computed the ratio between the dropsonde-estimated 10-m wind ( $U_{sfc}$ ) and the  $WL150$  at  $z_{min} = 10 \text{ m}$ , 50 m, 100 m, 150 m, 200 m. The results are shown in Figure 12, where the estimated ratios (red stars) are compared against those estimated by Uhlhorn *et al.*, (2007) (black stars). Discrepancies between both ratios are noticeable, especially above 100 m altitudes. In addition, the ratio from Uhlhorn *et al.*, (2007) sharply decreases for  $z_{min}$  values higher than 150 m, while such decrease is not seen in our estimates.

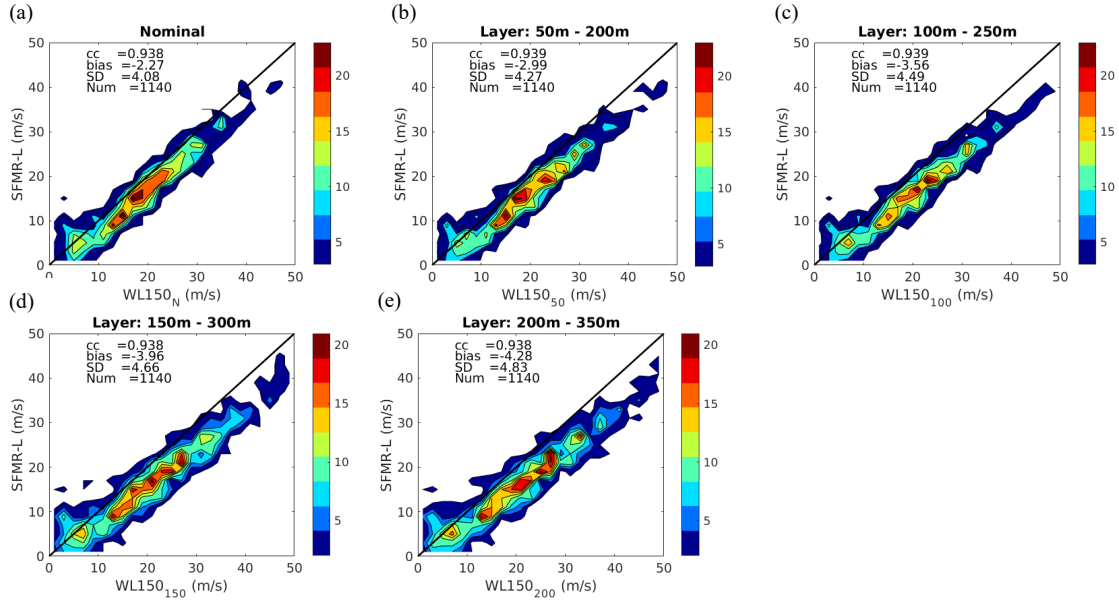


Figure 11. Two-dimensional histograms of the SFMR surface winds at the dropsonde launch time (SFMR-L) versus the collocated dropsonde WL150 winds (see colourbar). The WL150 wind speed is computed using dropsonde with lowest reading altitude ranging between 10-20 m. The 150 m layer is placed at the nominal altitudes (10-160m) (a), 50-200m (b), 100-250m (c), 150-300m (d) 200-350m (e). The same statistical parameters as in Figure 9 can be found in the legend.

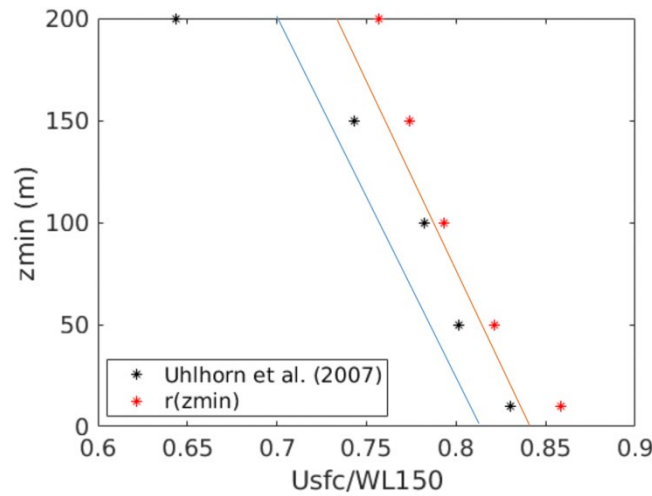


Figure 12. Ratio of the dropsonde surface wind speeds determined as  $U_{sfc} = 0.86 \cdot WL150_N$  and the WL150 wind speed, as a function of the altitude (red stars). The corresponding values of the ratio as presented in Uhlhorn et al., (2007) are also shown for comparison (black stars). For comparison, the corresponding ratios for a neutral profile with  $Z_0 = 1$  mm (solid red) and 5 mm (solid blue). Recall that for 5 mm, the correction is 0.81 rather than 0.86.

We have then derived a new functional form for this ratio with respect to the layer mean altitude ( $z_{mean}$ ), such that:

$$r(z_{mean}) = 1 - 2.24 \cdot 10^{-3} z_{mean} + 8.16 \cdot 10^{-6} z_{mean}^2 - 1.16 \cdot 10^{-8} z_{mean}^3 \quad (9)$$

In line with Figure 12, differences can also be seen between this polynomial function and that of Uhlhorn *et al.*, (2007). Such differences may be due to the fact that in Uhlhorn *et al.*, (2007), only eyewall dropsondes deployed in 2005 are examined, while in the current analysis dropsonde profiles from 2009 to 2018, outside the eyewall, are used. The behavior in eyewall conditions has not been addressed in this work. Moreover, no detailed description on how the  $r(z)$  functional form from Uhlhorn *et al.*, (2007) was obtained has been found so far, so further investigation is needed in order to better understand the source of such differences.

Assuming a logarithmic profile for the current outer eye-wall data with  $Z_0 = 1$  mm, we see a close fit at 50 m and 100 m, but a poorer fit at 10 m height, which might suggest uncertainty due to height, speed and acceleration knowledge. This would obviously lead to calibration errors in the 10-m winds, but also in the WL150 wind estimates.

On the other hand, in order to test the effect of the layer width, the WL150 wind has been computed considering different layer widths: 140 m – 150 m ( $WL150_N$ ), 90 m – 100 m ( $WL100$ ), 40 m – 50 m ( $WL50$ ) and 15 m – 25 m ( $WL25$ ). The data have been filtered in such a way that each layer contains at least 4 dropsonde measurements and the altitude of the lowest reading inside the layer is within 10 m to 15 m.

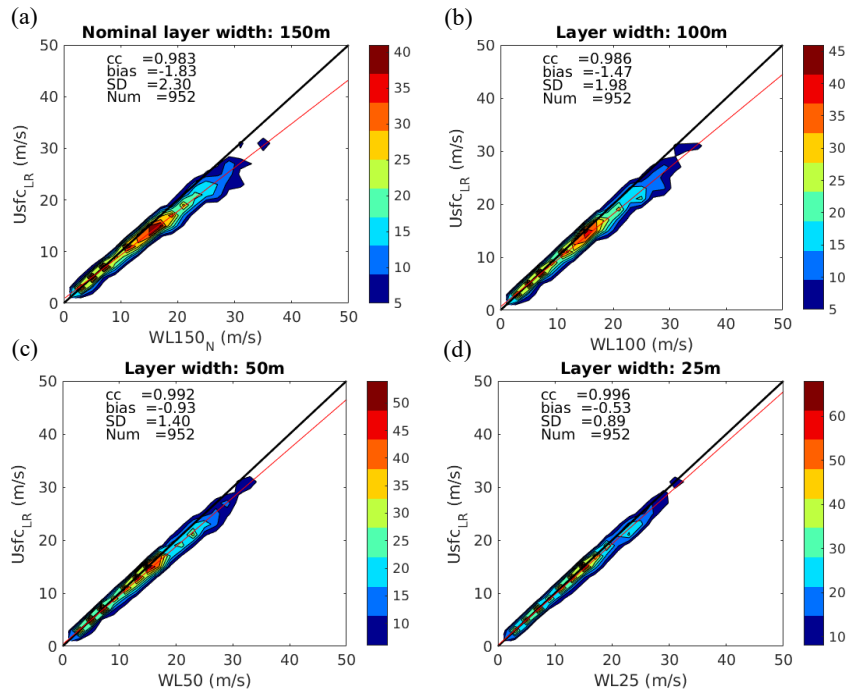


Figure 13. Two-dimensional histograms (see colourbar) of the dropsonde 10 m surface wind measurement and the dropsonde WL averaged winds at different layer widths: (a) 145m-150m ( $WL150_N$ ), (b) 95m-100m ( $WL100$ ), (c) 45m-50m ( $WL50$ ) and (d) 20m-25m ( $WL25$ ). All the layers correspond to the lowest altitude level, i.e., with a lowest reading around 10 m. The same statistical parameters as in Figure 9 can be found in the legend.

Figure 13 shows the comparison between the dropsonde LR surface wind ( $Usfc_{LR}$ ) and its corresponding WL averaged wind for the mentioned layer widths. As expected, when averaging the dropsonde measurements over smaller layers (w.r.t. the nominal 150-m layer) close to the surface, the correlation between the measured and the averaged wind increases. Both the mean bias and the SD considerably decreases when reducing the layer width to 25 m. As expected, the

regression (red) line changes with the layer width, approaching the diagonal (black line) for decreasing layer widths, which indicates again that the 25-m layer averaged winds are most representative of the dropsonde lowest level (10-m) winds.

In order to verify how representative the different WL averaged winds are of the SFMR winds, these two sets are compared in Figure 14. In this case, an additional filter has been included such that SFMR wind data with rain rate higher than  $10 \text{ mm hr}^{-1}$  are discarded. In the experience of NOAA/NESDIS/STAR OSWT not only rain-free data, but also those SFMR wind speeds derived under light rain conditions may be safely included in the analysis.

According to the previous results,  $WL150_N$  winds are higher than the SFMR-L winds. It should be noted though that Figure 14(a) has slightly different wind statistics than those of Figure 11(a). As it can be seen, the main difference between these two figures is the number of dropsondes used. This is due to the two different analyses performed. In one case, we only focus on those dropsondes, whose wind profiles allow the computation of the  $WL150$  wind at different altitudes. In the other, we focus on those dropsondes, whose wind profiles allow the computation of the averaged WL winds at different layer widths. This leads to a different dropsonde data filtering, where still  $WL150_N$  winds are higher than the SFMR-L winds, albeit a little less (10%).

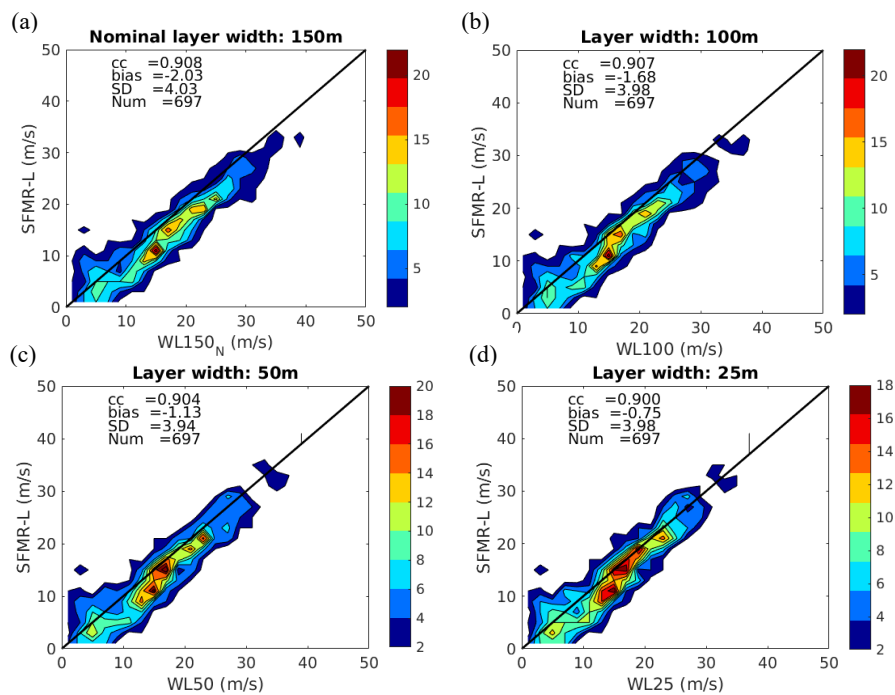


Figure 14. Two-dimensional histograms (see color bar) of the SFMR surface wind speeds at the dropsonde launch time (SFMR-L) and collocated dropsonde averaged winds. The dropsonde averaged wind speed is computed by using different layer widths of 140-150m (a), 90-100m (b), 40-50m (c), and 15-25m (d). The data have been filtered such that dropsondes having the layer lowest reading altitude between 10-20 m and a minimum of 5 readings per layer have been used. The same statistical parameters as in Figure 9 can be found in the legend.

The results in Figure 14 show that the mean bias between the averaged winds and the SFMR-L wind speeds decreases with decreasing layer widths as well as the root mean square error (not shown). In line with this, a slight increase of the SD of the difference is also seen at layer width

of 150 m with respect to 25 m, due to the fact that dropsonde measurements away from the surface become less representative of the SFMR winds, although at marginal statistical significance.

In order to more thoroughly address the representativeness differences between SFMR and dropsonde winds, an additional analysis has been carried out by comparing the dropsonde-estimated 10m surface winds with the collocated SFMR winds at different spatial scales. In particular, SFMR along-track averaged winds, centered at the SFMR-L position, are computed over 3 sec, 11 sec, 51 sec, 101 sec and 251 sec. Assuming that the aircraft speed is  $100 \text{ m s}^{-1}$  on average, such temporal distances correspond to a spatial distance of 200 m, 1 km, 5 km, 10 km and 25 km, respectively. In order to compute consistently averaged winds, a limit over the minimum number of QC-accepted SFMR points used in the average is set. In particular, since SFMR winds are provided at 1 Hz, this threshold is set to 2 points, 9 points, 40 points, 80 points and 200 points, respectively (i.e., a minimum of about 80% of valid points, except for the 3-sec averages for which a minimum of 66% of valid points is required). About 37% of the available collocations have the corresponding SFMR flight that meets these constraints, such that the computation of the five different averaged winds can be done.

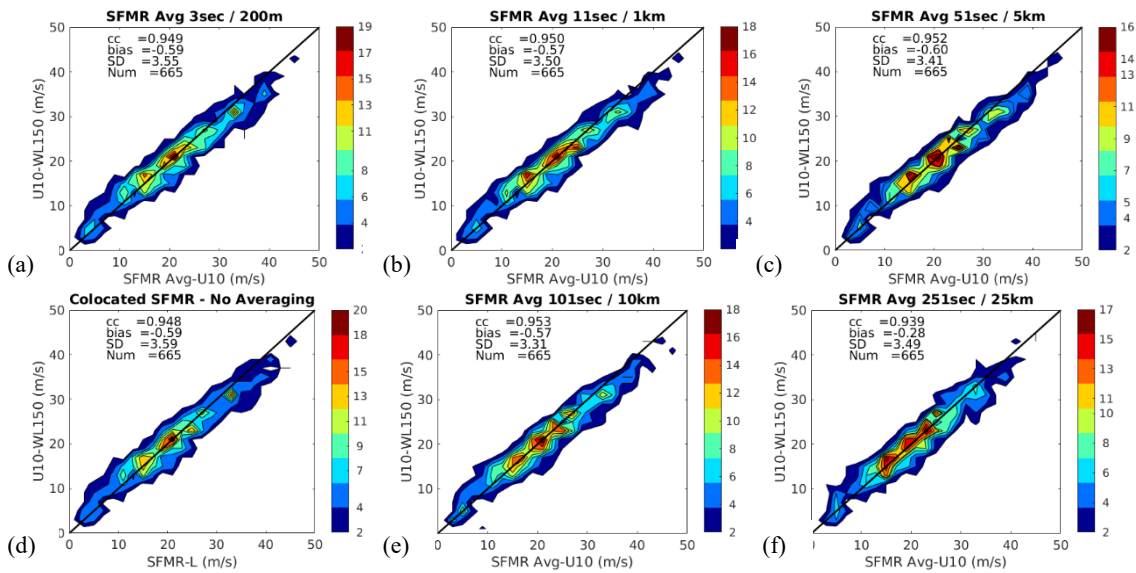


Figure 15. Two-dimensional histograms (see colorbar) of the dropsonde 10-m winds estimated using the WL150 algorithm versus the along-track averaged SFMR 10-m winds at different temporal/spatial scales: nominal (a), 3sec/200m (b), 11sec/1km (c), 51sec/5km (d), 101sec/10km (e), 251sec/25km (f).

The results in Figure 15 show that the dropsonde and SFMR winds at different temporal/spatial scale are in relatively good agreement with the dropsonde surface winds. There is a slight decrease (increase) of the SD (correlation, CC) for increased averaging widths, up to 10 km resolution. Note that for 25-km averaged winds, the SD (CC) increases (decreases) with respect to that of the 10-km averaged winds, indicating that the dropsonde spatio-temporally integrated measurement (by the WL algorithm) is more representative of about 10-km averaged SFMR winds. The location difference between SFMR and dropsonde probably prevents to investigate representativeness on scales smaller than 10 km, since different small-scale true variance is sampled by SFMR and dropsondes at 10-m height (cf. Figure 3 and Figure 8). The location difference may explain the differences in SD and CC at the the 5-km scales and smaller. Note though that the highest wind gradient regions are excluded from this analysis, since only dropsondes outside the eyewall region are used.

### 3.5. Summary

After detailed analysis of operationally exploited WL150 dropsonde winds, we conclude that it is not the best calibration resource from a dropsonde, as the reported 10-m surface wind is used as calibration reference in any case for WL150 and we found that WL150 may introduce noise as well as biases. An open question remains in the assessment of the position processing of the sonde near the surface, where its deceleration is maximum. The issue is related to the fundamental measurement of the dropsonde, i.e., the position measurement, which is proprietary information of the GPS manufacturers. Since the dropsonde is increasingly decelerated along its path towards the ocean surface, the position filtering could have systematic effects on reported position (lag), hence on computed speed and acceleration of the sonde, which are used to determine the 10-m wind. Detailed information from manufacturers appears essential to understand possible errors (error propagation modelling is needed). For future work, we furthermore suggest to include additional analysis using logarithmic wind profiles in order to further investigate the observed dropsonde 10-m winds.

## 4. ASCAT/SFMR WIND COMPARISON

In this Section, the ASCAT high-wind performance and calibration are investigated with respect to collocated SFMR winds. The ASCAT-related storm center estimation approach is shown in Section 4.1, while the ASCAT/SFMR collocation procedure is presented in Section 4.2. The SFMR wind data are analyzed at different temporal/spatial scales in order to assess the spatial representativeness error when compared against the 12.5-km sampled ASCAT wind products. Moreover, the SFMR rain data are also used to evaluate the impact of rain on both SFMR and ASCAT winds, notably for winds higher than  $25 \text{ m s}^{-1}$ . The results are shown and analyzed in Section 4.3.

### 4.1. ASCAT-related storm-centre estimates

In order to locate the storm center as sampled by each ASCAT overpass, the tropical cyclone “best track” (hereafter BT) data obtained from the WMO International Best Track Archive for Climate Stewardship (IBTrACS, Knapp et al., 2010) were used. In particular, we used the BT dataset version v03r10, available at the NOAA National Climate Data Center (online at <https://www.ncdc.noaa.gov/ibtracs/>). However, at the time this work has been performed, we have noticed that in this dataset there were few storms which did not have a complete BT for the whole duration of the storm. For those cases, the corresponding BT data available at the NOAA Hurricane Center have been used (<ftp://ftp.nhc.noaa.gov/atcf>).

BT data sets provide an estimate of the storm position every six hours for the whole duration of the storm. The BT data have then been linearly interpolated in order to have a storm position every second (hereafter referred to as BTsec position) in line with the SFMR temporal sampling rate. The methodology developed to identify the ASCAT wind vector cell (WVC) representing the storm center, consists of the following steps:

- i) First, select only the BTsec data within the time frame of each ASCAT orbit to reduce the number of points;
- ii) Then, compute the time difference between each BTsec point and the ASCAT WVCs and keep only those BTsec/ASCAT-WVC pairs where such difference is  $\leq 1$  second;
- iii) Finally, compute the spatial distance of each selected pair, i.e., between each selected ASCAT WVC and BTsec position; the ASCAT WVC whose selected pair distance is the lowest is chosen as the storm center. If the storm is out of the ASCAT swath, we use a 200 km distance limit between the selected ASCAT WVC and BTsec position.

Figure 16 shows an example of the selected WVC and the corresponding BTsec positions for hurricane Nicole on October 13<sup>th</sup>, 2016.

With this method, the accuracy of the ASCAT-related storm center strongly depends on the accuracy of the BT data. The wind community still argues about the accuracy of the BT center estimates, notably when interpolated in between 6-hour periods. But, so far, the BT data are one of the main sources publicly available online, providing the storm positions for most of the storm duration. The storm center positions can also be estimated using the SFMR data from the hurricane hunters during their flight experiments. Such center estimates are more accurate than the BT data. However, these data sets only cover the time interval in between the flight few storm centre crossings and, as such, the number of storm center estimates is limited to the number of the mentioned storm crossings. In this study, to maximize the ASCAT/SFMR collocations, the BT data are therefore used, in turn leading to larger ASCAT/SFMR collocation

errors (see also Section 4.2). An example of a clear storm centre mislocation is shown in Figure 17 of hurricane Matthew on September 30<sup>th</sup>, 2016. The storm center, as estimated by BTsec at the time of the ASCAT pass (black star), does not match the center as deduced from the ASCAT-derived wind field. As a consequence, the misplaced ASCAT WVC is then (wrongly) selected as the storm centre (green star).

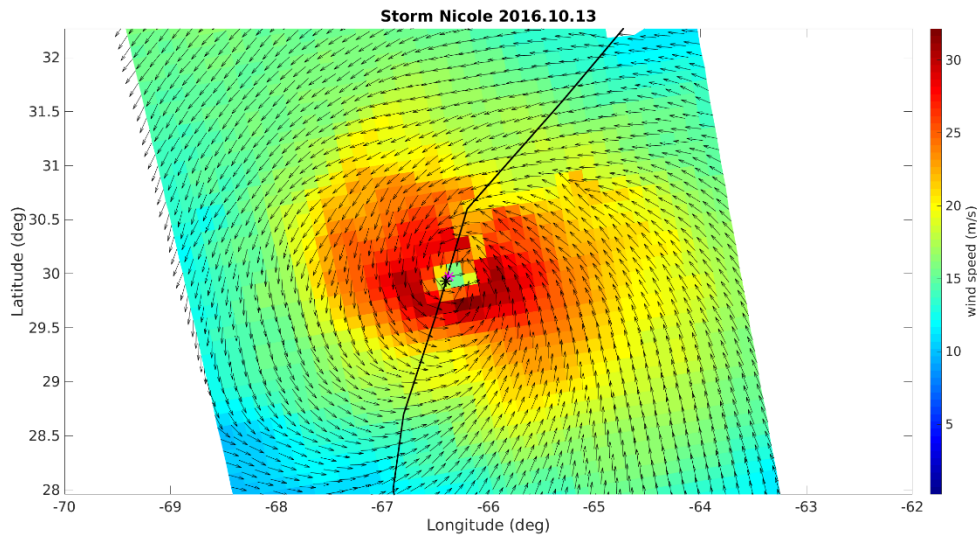


Figure 16. ASCAT wind map of hurricane Nicole on October 13<sup>th</sup>, 2016, along with the storm BTsec positions within a few hours from the ASCAT pass (solid line). The ASCAT WVC selected as the storm center (purple star) and the corresponding BTsec point (black star) are also shown.

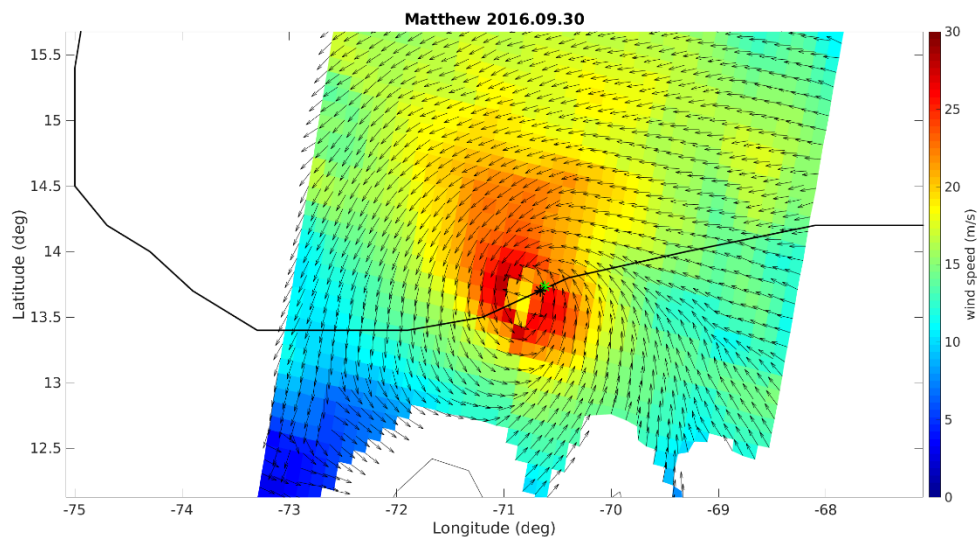


Figure 17. ASCAT wind map of hurricane Matthew on September 30<sup>th</sup>, 2016, along with the storm BTsec ASCAT WVC selected as the storm center (green star) and the corresponding BTsec point (black star) are also shown positions within a few hours from the ASCAT pass (solid line).

## 4.2. ASCAT/SFMR collocation approach

In order to perform collocations between ASCAT and SFMR, the first step is to convert the SFMR track in storm motion relative coordinates. This conversion is performed to allow a larger collocation temporal window between SFMR and ASCAT acquisitions. The underlying assumption is that within a certain temporal window (e.g., 2 or 3 hours), the structure of the hurricane (with respect to the direction of displacement of the storm) does not change. As such, SFMR spatially and temporally varying observations are projected into a “frozen” hurricane structure during such temporal window. This is done by converting the SFMR coordinates into a new coordinate system identified by the BT position at the time of each SFMR sample. Regarding the reference of the new coordinate system (i.e., the storm motion direction), different options can be considered. One option is to use the motion vector derived from consecutive BTsec points at every SFMR (1-sec) sampled location. Note that best track data are six hours apart, meaning that all SFMR acquisitions within such time frame share the same storm motion vector. Although such option seems quite consistent since the conversion closely follows the storm track as seen by the BT data, it may cause artefacts when the SFMR flight occurs over two consecutive BT 6-hour periods and there is an abrupt change of the storm motion direction. An example of such artefacts is shown in Figure 18. The ASCAT wind map of hurricane Karl on September 23<sup>rd</sup>, 2016, along with the BTsec data (within  $\pm 12$  hours of the ASCAT pass) and part of the SFMR flight track are shown both in original (Figure 18a) and storm-relative (Figure 18b) coordinates. Between  $-67^\circ$  and  $-66^\circ$  longitude and  $29^\circ\text{N}$  and  $30^\circ\text{N}$  latitude, a flight track North-South shift can be seen in the motion-relative SFMR with respect to the original track. This shift is located at a transition point between two consecutive BT 6-hour periods in which a remarkable storm motion turn is reported (see purple line direction changes). Such storm turn is obviously not produced from one second to the next, but since BT positions are only reported every 6-hours, a very abrupt storm motion vector change is estimated, which leads to the mentioned artefact in the storm motion centric flight track.

Alternatively, one can use splines to smoothly interpolate over the BT 6-hour positions, but the problem is that the storm motion turn can happen anytime within the 6-hour period, which means that any interpolation strategy will lead to similar storm motion vector errors. A more practical approach to avoid such artefacts is to use a single vector, which best represents the storm motion at the time of the SFMR flight (see Figure 18c) or of the ASCAT overpass. In this analysis, the BTsec position around the mean time of the SFMR storm centre crossings ( $t_{mean}^{SFMR}$ ) is used to compute the single storm motion vector.

The value of  $t_{mean}^{SFMR}$  has been computed by using the mean time of the SFMR wind speed measurements within the highest 15% wind speed data. To validate this value, the aircraft altitude at  $t_{mean}^{SFMR}$  is used. Note that during the storm crossings, the aircraft altitude is relatively constant but varies from flight to flight between 1.5 km and 3.5 km, which means that the flight level cannot be effectively used to compute  $t_{mean}^{SFMR}$ . With the proposed approach though,  $t_{mean}^{SFMR}$  usually corresponds to the time in the middle of the temporal window when the aircraft stays at such operational altitude. An example of the typical altitude of the aircraft at  $t_{mean}^{SFMR}$  is shown in Figure 19. Once the best track position at  $t_{mean}^{SFMR}$  has been identified, the corresponding storm motion vector is computed and the SFMR trajectory (see, e.g., Figure 20a) is converted into storm-motion coordinates, such that each SFMR point is referenced to the storm centre in polar coordinates, as shown in Figure 20b. It is important to mention that, due to the large variety of storm cases, the selected  $t_{mean}^{SFMR}$  may sometimes correspond either to the beginning or to the

end of the storm crossing time window, depending on how strong the winds are within each cross. In the few cases in which the SFMR storm centre crossings are within two different BT 6-hour windows, different  $t_{mean}^{SFMR}$  estimation approaches may lead to either one storm motion vector or another. However, the use of one vector with respect to another, if close in time, does not significantly affect the results, since both are equally (un)certain. The main limitation of this methodology is that, besides the uncertainty in the BT data itself, the storm track is unknown within the six hours separating two best track points. As a consequence, the selected reference vector may not accurately describe the actual storm movement, especially if the storm rapidly changes during this time. We assume that the storm velocity is constant over the 6-hour period, which is a rather crude assumption.

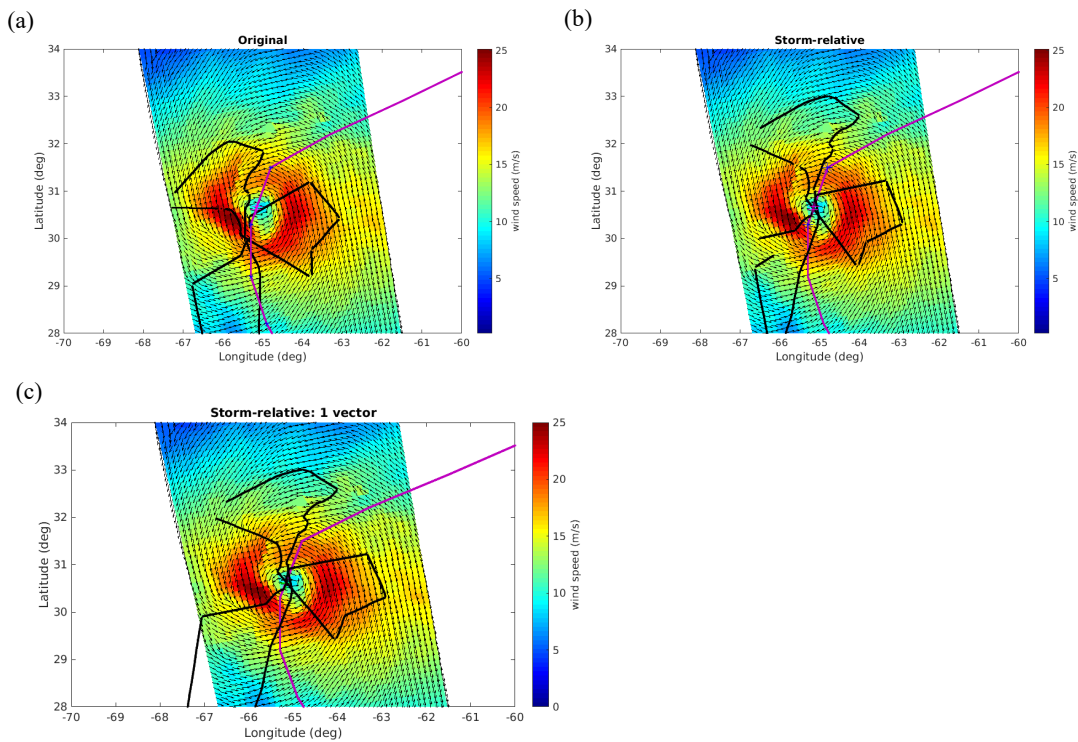


Figure 18. ASCAT wind field over hurricane Karl on September 23<sup>rd</sup>, 2016 along with the storm BTsec positions within a few hours from the ASCAT pass (purple line). The black line corresponds to the NOAA I2 SFMR flight trajectory in original coordinates (a), storm-motion relative coordinates (b) and storm-motion relative coordinates derived using a single vector (c). In (b) a track North-South shift is seen between  $-67^{\circ}/-66^{\circ}$  longitude and  $30^{\circ}$ N latitude, which is not seen in (c).

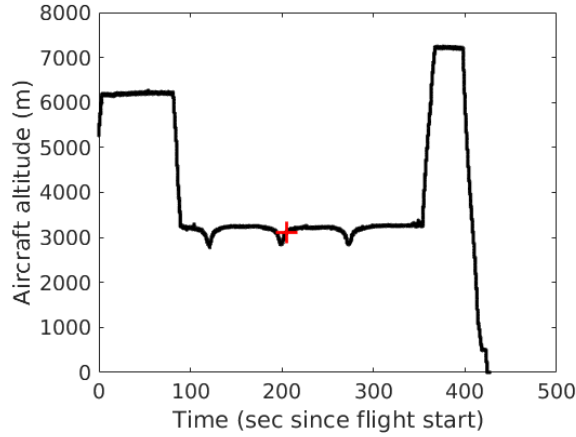


Figure 19. NOAA flight SFMR170903H1 during hurricane Irma on September 3<sup>rd</sup>, 2017 Aircraft altitude with respect to time, along with the altitude at  $t_{mean}^{SFMR}$  (red cross).

The converted SFMR trajectory is then relocated and centered on the BTsec corresponding to the ASCAT WVC selected as storm center (see Section 4.1). Then, such BTsec, that corresponds to the time of the ASCAT selected WVC ( $t_{SCAT}^C$ ), is used to re-compute the storm motion vector at the ASCAT pass time. This is done to provide a reference to the SFMR storm-motion centric track when collocated with ASCAT. This allows collocating ASCAT and SFMR data even when separated a few hours in time. However, the assumption on the “frozen” hurricane structure (see beginning of Section 4.2) cannot hold for long time differences. As such, the time distance between the hurricane hunters aircraft passes over the storm and the ASCAT pass, as defined in Eq. 10, is considered to filter the data. Those storm cases where  $\Delta t^* > 3$  h are discarded from the analysis. This ensures that ASCAT and SFMR observe the storm almost at the same time, so that we can assume that they capture the same storm structure and intensity.

$$\Delta t^* = |t_{SCAT}^C - t_{mean}^{SFMR}| \quad (10)$$

Finally, in order to compare the SFMR wind speed measurements with the corresponding ASCAT WVC wind, a spatial distance of  $6.25\sqrt{2}$  km is used to collocate the data. The wind comparisons are then analyzed with respect to the time difference between each SFMR measurement and the ASCAT pass.

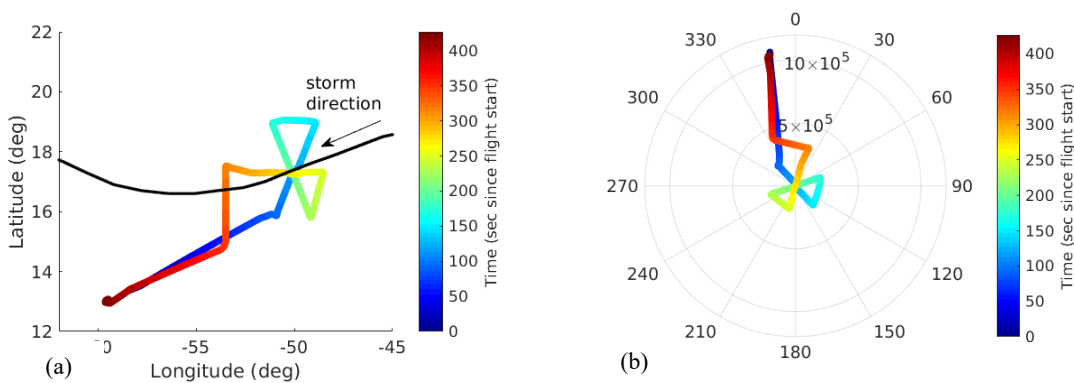


Figure 20. NOAA flight SFMR170903H1 during hurricane Irma on September 3<sup>rd</sup>, 2017. (a) Aircraft trajectory in original coordinates with respect to time (see colourbar), along with the BT data (black line); (b) Corresponding flight in storm-motion relative coordinates.

Note that, in order to carry out any ASCAT/SFMR analysis that involves the use of the corresponding BT data, the storm associated to the SFMR flight needs to be identified. Generally, the storm name is not provided in the SFMR file, but it is necessary to associate the SFMR flight to the correct BT data. To this end, we compute the distance ( $d^*$ ) between the SFMR flight position and the BTsec at  $t_{mean}^{SFMR}$  and we associate to each SFMR the BT data (and in turn the corresponding storm name) having  $d^*$  lower than 300 km. If the position at  $t_{mean}^{SFMR}$  is not available, we use the first available position within  $t_{mean}^{SFMR} \pm 5$  sec.

### 4.3. ASCAT/SFMR wind comparisons

The time difference between the ASCAT pass and the time when the hurricane hunters fly into the storm plays an important role in the wind comparison. As such time difference increases, the ASCAT/SFMR wind agreement decreases. Three examples of ASCAT-SFMR passes at different  $\Delta t^*$  are shown in Figure 21. The first example in Figure 21a, which refers to Hurricane Matthew on October 2<sup>nd</sup> 2016, has a  $\Delta t^* \cong 90$  min. The second example in Figure 21b, which refers to Hurricane Erika on August 26<sup>th</sup> 2015, has a  $\Delta t^* \cong 45$  min. The third example in Figure 21c, which refers to hurricane Julio on August 10<sup>th</sup> 2014, has a  $\Delta t^* \cong 30$  min. In all three cases, ASCAT significantly underestimates winds above  $15 \text{ m s}^{-1}$  with respect to SFMR wind speeds and, as expected, such discrepancies increase as the ASCAT winds increase. It is clear though that  $\Delta t^*$  plays an important role. The larger the  $\Delta t^*$ , the larger the ASCAT-SFMR wind discrepancies.

To carry out a statistical comparison between collocated ASCAT and SFMR winds, the time separation  $\Delta t$  between each SFMR wind acquisition and the ASCAT pass is used:

$$\Delta t = |t_{SCAT}^C - t_i^{SFMR}| \quad (11)$$

where  $t_i^{SFMR}$  is the time of the collocated SFMR measurement). The first comparison is done by collocating the ASCAT winds with the spatially-closest SFMR winds. The statistics are computed for  $\Delta t \leq 1h$  (Figure 22a),  $\Delta t \leq 2h$  (Figure 22b),  $\Delta t \leq 3h$  (Figure 22c). As previously mentioned, ASCAT is considerably than SFMR at high winds, however, it is worth noticing that ASCAT and SFMR winds have a reasonable scatter and they are very well correlated, with a correlation coefficient of 0.88. The correlation slightly decreases and the scatter increases with increasing time differences.

Very similar results to those in Figure 22 are obtained by collocating ASCAT winds with SFMR winds averaged over a distance of 12.5 km along track (see Figure 23). Note that there is a slightly better agreement between ASCAT and SFMR winds in terms of correlation coefficient and SD, when using SFMR spatially-averaged winds, indicating that the latter are more representative of ASCAT wind scales than the SFMR single measurements.

In Chou *et al.* (2013) a comparison between ASCAT and dropsonde wind speeds is shown. ASCAT high winds are clearly lower with respect to dropsonde winds in this study. Since dropsonde winds are used to calibrate SFMR, the ASCAT/SFMR results shown in this study are consistent with the ASCAT/dropsonde results reported in Chou *et al.* (2013).

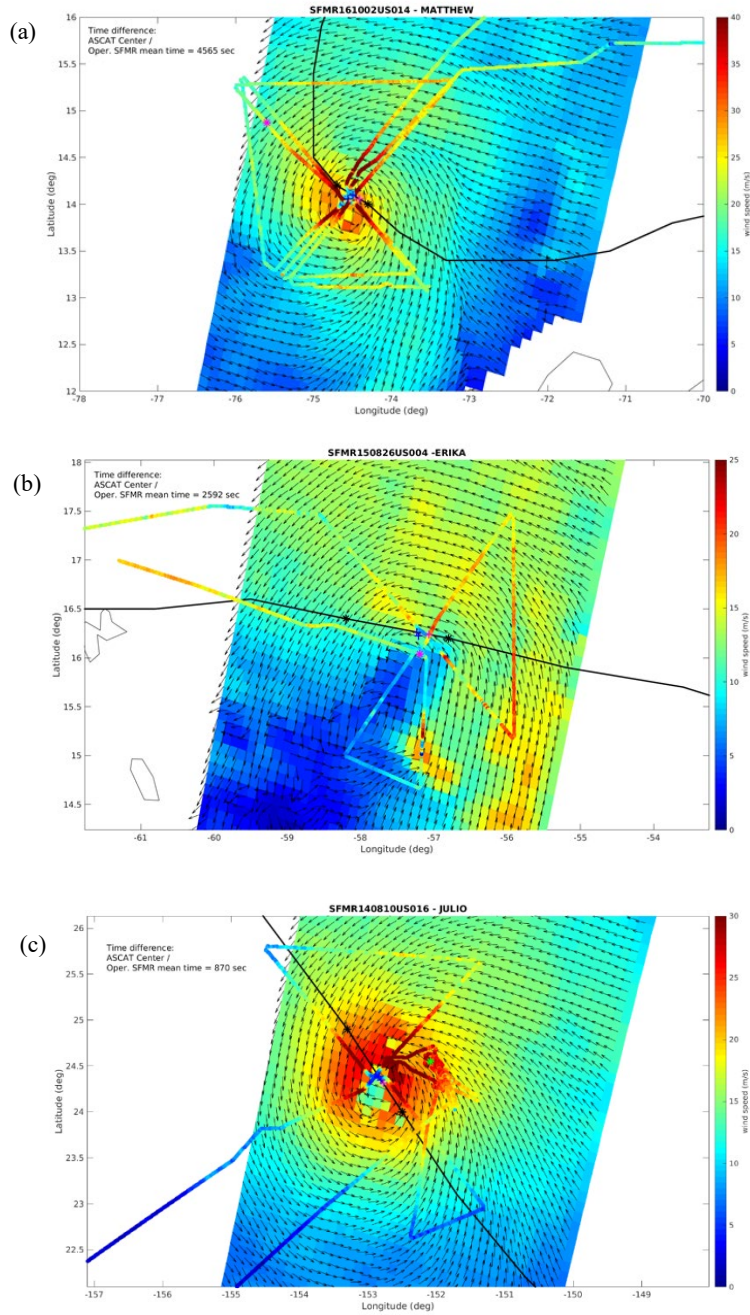


Figure 21. ASCAT wind intensities (see colorbar) along with the corresponding SFMR winds for three storms at different  $\Delta t^*$ : (a) hurricane Matthew on October 2<sup>nd</sup> 2016,  $\Delta t^* \cong 90$  min; (b) hurricane Erika on August 26<sup>th</sup> 2015,  $\Delta t^* \cong 45$  min, hurricane Julio on August 10<sup>th</sup> 2014,  $\Delta t^* \cong 30$  min.

Another relevant result from Figure 22 and Figure 23 is that the correlation between ASCAT and SFMR winds is relatively high, meaning that a suitable scaling (calibration) of ASCAT winds leads to very consistent ASCAT and SFMR high wind retrievals, as shown in Figure 24. The recalibrated ASCAT winds ( $x'$ ) are made consistent with SFMR by applying  $x' = 0.0095x^2 + 1.52x - 7.6$  to the nominal ASCAT winds ( $x$ ) above 12 m/s. Note that this recalibration improves correlation with SFMR by about 2% and reduces the RMS difference about 15%.

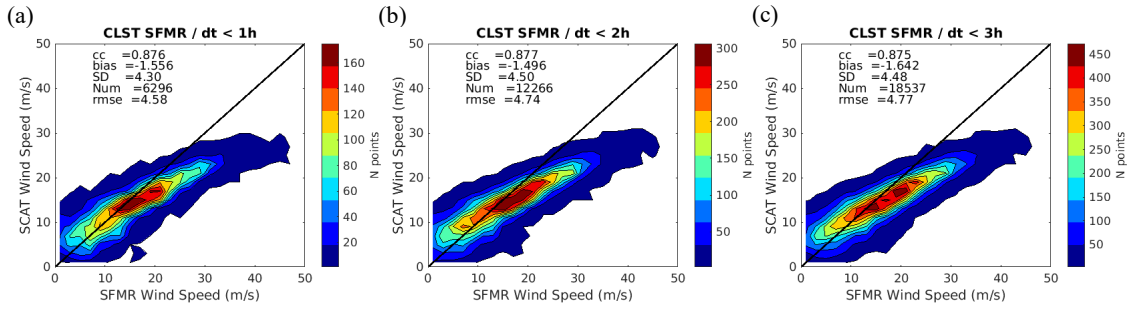


Figure 22. Two-dimensional histograms of ASCAT and collocated SFMR wind speeds, for  $\Delta t \leq 1h$  (a),  $\Delta t \leq 2h$  (b),  $\Delta t \leq 3h$  (c). The same statistical parameters as in Figure 9 can be found in the legend.

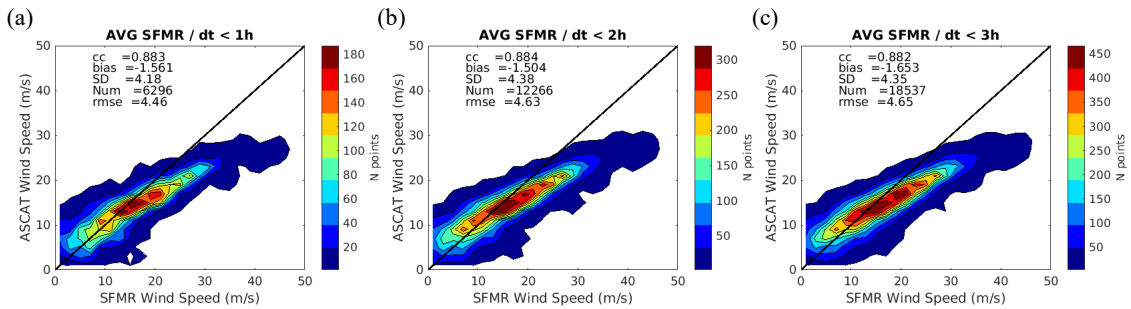


Figure 23. Same as Figure 22, but for collocated SFMR winds averaged over a distance of 12.5 km along track.

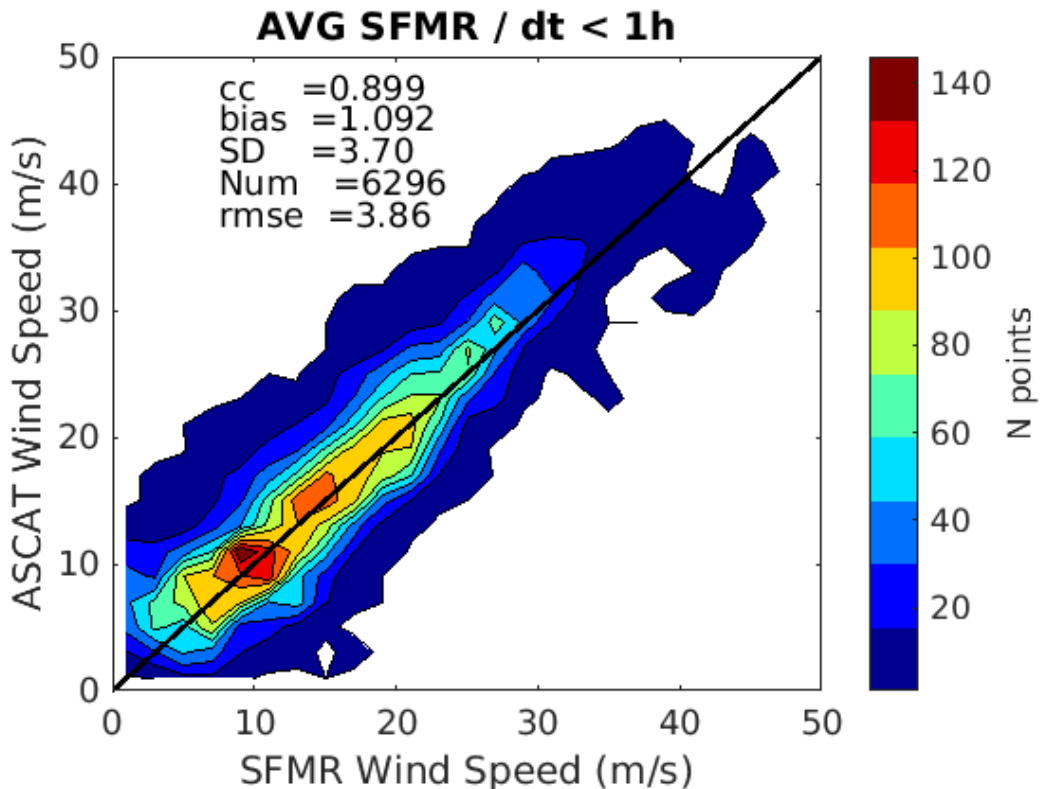


Figure 24. Two-dimensional histograms of ASCAT and collocated SFMR wind speeds, for  $\Delta t \leq 1h$  (a) as in the figure above, but now for recalibrated ASCAT winds with respect to SFMR. The same statistical parameters as in Figure 9 can be found in the legend.

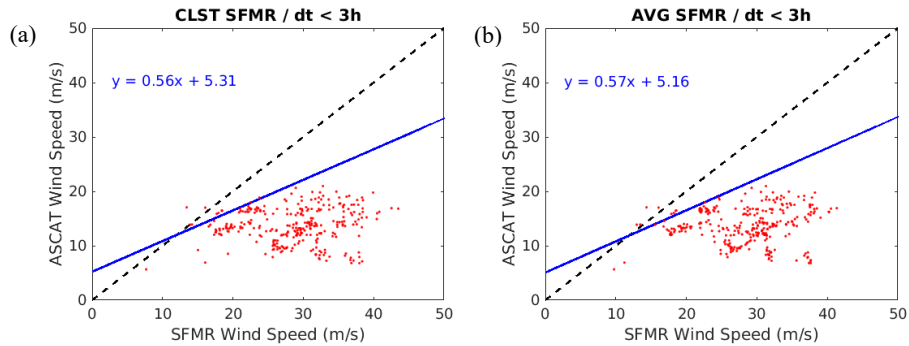


Figure 25. (a) Regression line (solid line) of the ASCAT/SFMR wind comparison as shown in Figure 22c. (b) Same as (a) but using the collocated averaged SFMR wind, as shown in Figure 23c. The equation of the regression line is shown in the legend. The red dots identify the outliers.

Note that with the developed collocation methodology, we were also able to identify outliers in the ASCAT/SFMR wind comparison. In Figure 25a and Figure 25b, the regression line (blue solid line) of the ASCAT/SFMR statistics for  $\Delta t \leq 3h$  corresponding to Figure 22c and Figure 23c, respectively, are shown. As it can be seen from the red dots, there is a considerable amount of ASCAT/SFMR pairs which are far from the corresponding regression line. These SFMR data belong to four SFMR flights corresponding to the following storms: SFMR 2009.08.10 US008 (Hurricane Felicia); SFMR 2009.09.01 US010 (Hurricane Jimena); SFMR 2012.08.27 US012 (Hurricane Isaac); SFMR 2017.09.18 US004 (Hurricane Maria).

For those pairs, the corresponding SFMR winds are much higher than the nominal ASCAT winds. We have checked the values of  $\Delta t^*$  for each flight and it does not exceed 113 min, therefore, the ASCAT/SFMR time difference should not be the cause of such wind disagreement. An example is shown in Figure 25, corresponding to the SFMR flight (in storm-motion-relative coordinates) over Hurricane Isaac. Since ASCAT is considered a stable wind reference, such large differences in the wind estimates are probably due to SFMR calibration issues. However, further investigation is needed to better understand the source of such discrepancies.

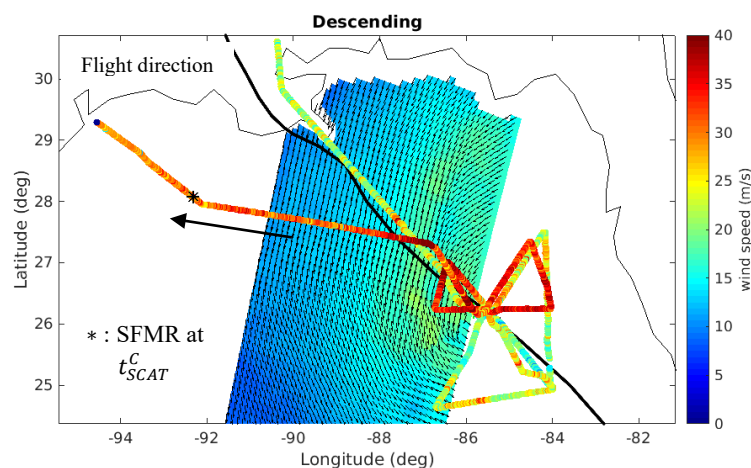


Figure 26. SFMR winds (see colorbar) during the AFRC flight US012 on August 27<sup>th</sup>, 2012 for hurricane Isaac. The corresponding ASCAT wind intensities are also shown.

#### 4.4. Summary

In summary, the reprocessed ASCAT winds are collocated with SFMR winds, using storm-motion centric coordinates to allow collocations even when they are separated by a few hours in time. Several sources of collocation errors have been reported, namely the Best-Track temporal sampling and geolocation inaccuracies and the temporal differences between the SFMR and ASCAT acquisitions. In particular, it is concluded that ASCAT/SFMR collocations with time differences larger than 3 h should be discarded from the analysis. Although ASCAT winds are found to be substantially lower than SFMR winds above  $15 \text{ m s}^{-1}$ , a high correlation coefficient of about 0.9 is found between both wind sources, and a preliminary recalibration of ASCAT winds leads to very consistent extreme winds. Before drawing any conclusion on ASCAT high-wind calibration, the ASCAT winds are compared to collocated buoy winds under high wind conditions in the next section.

## 5. ASSESSING BUOY WIND REFERENCE QUALITY

Moored buoy winds have been developed to sustain high wind conditions. However, for a buoy to meet hurricane winds is quite unlikely, where one particular case is shown in Figure 27 below. While the wind measurements look credible until the anemometer breaks when the eye wall passes the second time, it is not possible to accurately verify the buoy winds in this particular case. As shown below, the credibility of moored buoy winds may be investigated at higher latitudes, where winds between 15 and 25 m s<sup>-1</sup> are more common. We further note that commonly the 10-minute wind data reports over an hour, which represents the latest, complete six 10-min. segments before the end of the last acquisition, bounded by minutes 0, 10, 20, etc.. This may cause an apparent lag between, e.g., wind and pressure measurements.

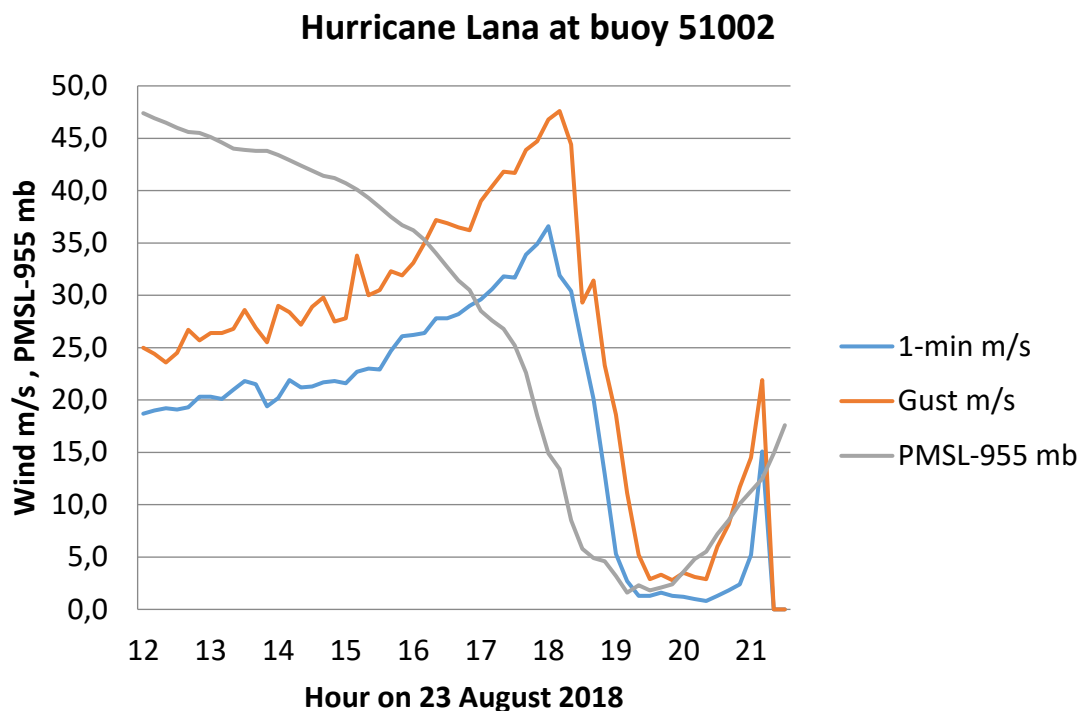


Figure 27. Moored buoy (number 51002) observation in hurricane Lana of mean sea level pressure, PMSL, above its estimated minimum of 955 mb, 1-minute sustained winds and local wind gusts. The wind measurements look credible until the anemometer breaks when the eye wall passes the second time and the PMSL surges.

Moored buoys come in a wide variety of configurations (e.g., in terms of mooring design, sensor types, sampling schemes, mounting techniques and telemetry) serving a wide variety of operational and research applications and disciplines. Bradley and Fairall (2006) focus on the requirements to make climate-quality meteorological and flux measurements at sea. Web sites for marine meteorological measurements from operational moored buoys are, inter alia:

- JCOMMOPS: <http://www.jcommops.org/>;
- ATLAS tropical moored buoys:  
[http://www.pmel.noaa.gov/tao/proj\\_over/mooring.shtml](http://www.pmel.noaa.gov/tao/proj_over/mooring.shtml)[http://www.pmel.noaa.gov/tao/proj\\_ove\\_r/mooring.shtml](http://www.pmel.noaa.gov/tao/proj_ove_r/mooring.shtml);
- NOAA Ocean Climate Stations: <http://www.pmel.noaa.gov/OCS>;

- TRITON tropical western Pacific moored buoys: [http://www.jamstec.go.jp/jamstec/TRITON/real\\_time/php/top.php](http://www.jamstec.go.jp/jamstec/TRITON/real_time/php/top.php);
- Global Tropical Moored Buoy Array: <https://www.pmel.noaa.gov/gtmba/>
- OceanSITES reference moored buoys: <http://www.oceansites.org>;
- Tsunami buoys: <http://www.ndbc.noaa.gov/dart/dart.shtml>;
- Wind/wave buoys: <http://www.jcomm.info/wet>;
- TRITON moored buoys: <http://www.jamstec.go.jp/iorgc/iomics/index.html>;
- <http://www.jamstec.go.jp/iorgc/iomics/index.html>;

In this section, the buoy wind quality at high wind conditions, i.e., between 15 and 25 m s<sup>-1</sup>, is assessed. First the consistency between two different buoy datasets, i.e., Cwinds and MARS winds, is assessed in section 6.1. Then, in section 6.2, the buoy winds are compared against ASCAT winds and triple collocation analysis is carried out to evaluate the quality of the buoy high-wind observations.

### 5.1. Cwinds versus MARS buoy winds

The Cwinds are collocated with MARS buoy winds over the period 2009-2014. Several inconsistent issues are found in the collocations:

- ~2.4% of Cwinds and MARS buoy data are with different anemometer height;
- The Temperature sensor Height (TsH) recorded in the MARS dataset is accurate to one decimal place; while in the Cwinds dataset, TsH below 4 m is assigned to a fixed value of 3 m (19.7% of the buoy measurements are indeed with TsH < 4 m).

Such inconsistency may lead to additional errors when converting the raw buoy wind speed to 10-m equivalent neutral ( $U_{10N}$ ) winds. Nevertheless, Figure 28 shows the histograms of buoy wind speed for different categories. It is clear that, the collocated Cwinds (purple line) and MARS (red line) winds have similar probability density functions (PDFs), particularly for winds above 10 m s<sup>-1</sup>. The slight differences for winds below 10 m s<sup>-1</sup> are probably due to the binning effect and the inconsistent sensor heights associated with the two datasets. The MARS buoy data set contains more high winds than the Cwinds (see the difference between the black and the blue curves above 10 m s<sup>-1</sup>; moreover, the number of points in the black PDF is about two times larger than that of the blue PDF), because the former dataset contains more buoys at high latitudes (e.g., ODAS).

After excluding the collocations with inconsistent sensor heights, the scatter plot of Cwinds versus MARS buoy wind speed data is shown in Figure 29. Again, this confirms that both buoy datasets are in good agreement, particularly for high wind conditions ( $w > 15$  m s<sup>-1</sup>). Note that the Cwinds high winds are also in good agreement with MARS high winds when comparing the collocated datasets with inconsistent sensor heights (not shown).

The wind variability under different wind speed conditions is estimated from the Cwinds data set. That is, the variance associated with buoy wind time series is translated into spatial wind variability using Taylor's hypothesis (Taylor, 1938), which allows for a temporal dimension to be converted into a spatial dimension, and vice versa. The time window (centred on the buoy measurement collocated with the ASCAT acquisition) used for calculating the mean buoy winds and the sub-cell spatial variability is defined by (May and Bourassa, 2011),

$$t_{window} = \frac{l_{footprint}}{\bar{w}} \quad (12)$$

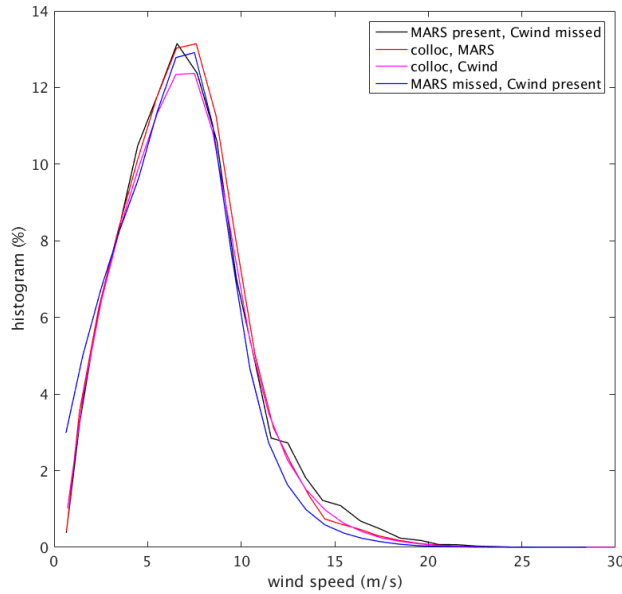


Figure 28. Histograms of the different buoy wind speed datasets for the two different sources. The black (blue) curve corresponds to the available MARS (Cwinds) buoy winds when the Cwinds (MARS) are missing; the red and magenta curves correspond to the collocated MARS winds and Cwinds respectively when both wind data sources are available. The collocation numbers of the above four categories are 3.4 million (black), 2.5 million (red), 2.5 million (magenta) and 4.4 million (blue), respectively

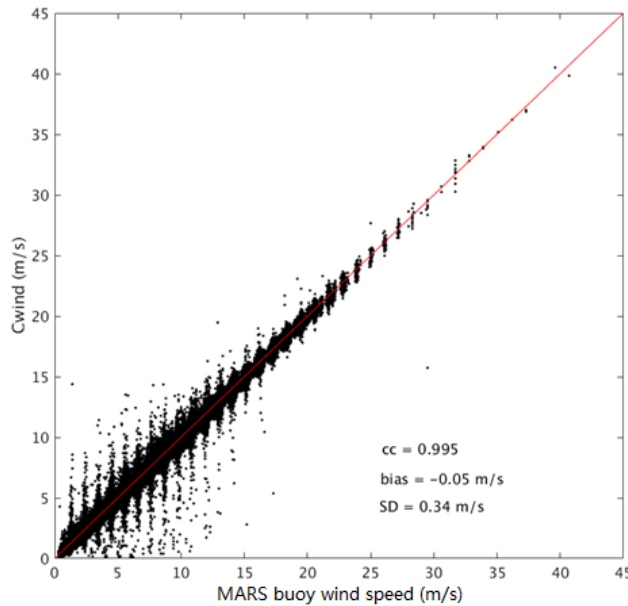


Figure 29. Scatter plot of Cwinds speed versus MARS buoy wind speed. The scores of the correlation coefficient (CC), the bias, and the SD of the speed differences are shown in the legend. The total number of points is 2.5 million.

where  $l_{footprint}$  is the ASCAT footprint size (i.e., 25 km in this study), and  $\bar{w}$  is the mean buoy wind speed within the time window. Figure 30 shows the mean SD value (a representation of the wind variability) of the wind  $u$ ,  $v$  and speed components for different speeds. It is clear that the wind variability increases with decreasing wind speeds, for low and medium wind conditions ( $w < 15 \text{ m s}^{-1}$ ). Note that due to mesoscale turbulence and convection, Taylor's hypothesis

becomes rather crude below  $7 \text{ m s}^{-1}$ , which corresponds to averaging lengths more than an hour. An anomalously high wind variability appears for  $w > 23 \text{ m s}^{-1}$ , which is not statistically significant due to the lack of buoy measurements.

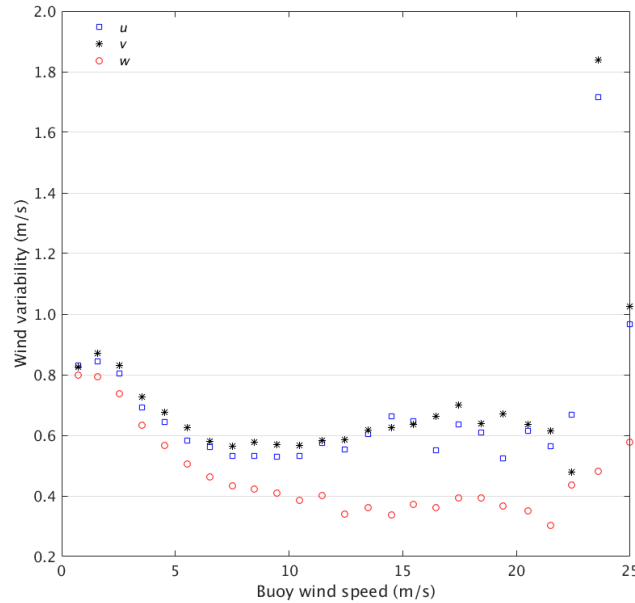


Figure 30. The wind variability estimated from the Cwinds dataset: the blue square and black symbols correspond to the zonal ( $u$ ) and meridional ( $v$ ) wind components, while the red symbol corresponds to the wind speed.

Hence, MARS buoy winds are favourable for high wind calibration, since these are more abundant and seemingly of equal quality to the archived buoy data. In a correspondence with UCAR on Cwinds QC, they agreed to track some of the collocated MARS and archive winds to check their QC procedures (in progress).

## 5.2. ASCAT/Buoy wind comparison

Since the different buoy datasets are in good agreement at high wind conditions and there are more high winds available in the MARS buoy dataset, the collocated ASCAT and MARS buoy winds are used to evaluate the buoy high wind quality in this sub-section. The collocation criteria for MARS buoy data are 30 minutes distance in time and 25 km distance in space from the ASCAT acquisitions. However, only the closest ASCAT WVC to the buoy acquisition is used in case more than one WVC meets the collocation criteria. The total amount of collocations is about 350,000. Figure 31 (a) illustrates the scatter-density plot of ASCAT wind speed versus MARS buoy wind speed for the QC-accepted data. In general, there is very good agreement between ASCAT and MARS wind speeds, as shown both by the scatter plot and the statistical scores (see legend). When focusing only on winds between  $15 \text{ m s}^{-1}$  and  $25 \text{ m s}^{-1}$  ( $15 \text{ m s}^{-1} - 1 < \frac{W_{ASCAT} + W_{buoy}}{2} < 25 \text{ m s}^{-1} - 1$ ,  $N \approx 9700$ ), a more pronounced bias of  $-0.30 \text{ m s}^{-1}$  is present, while the SD is only slightly larger ( $1.27 \text{ m s}^{-1}$ ), as compared to the overall distribution. This indicates that, on the one hand, there is a good agreement (low SD) between ASCAT and buoy high winds, and on the other hand, ASCAT  $U_{10S}$  winds underestimate high winds with respect to buoy  $U_{10N}$  winds. Figure 31 (c) shows that ECMWF wind speed is even lower than the buoy wind speed at high wind conditions, in which case the bias is about  $-0.85 \text{ m s}^{-1}$  in  $U_{10N}$ .

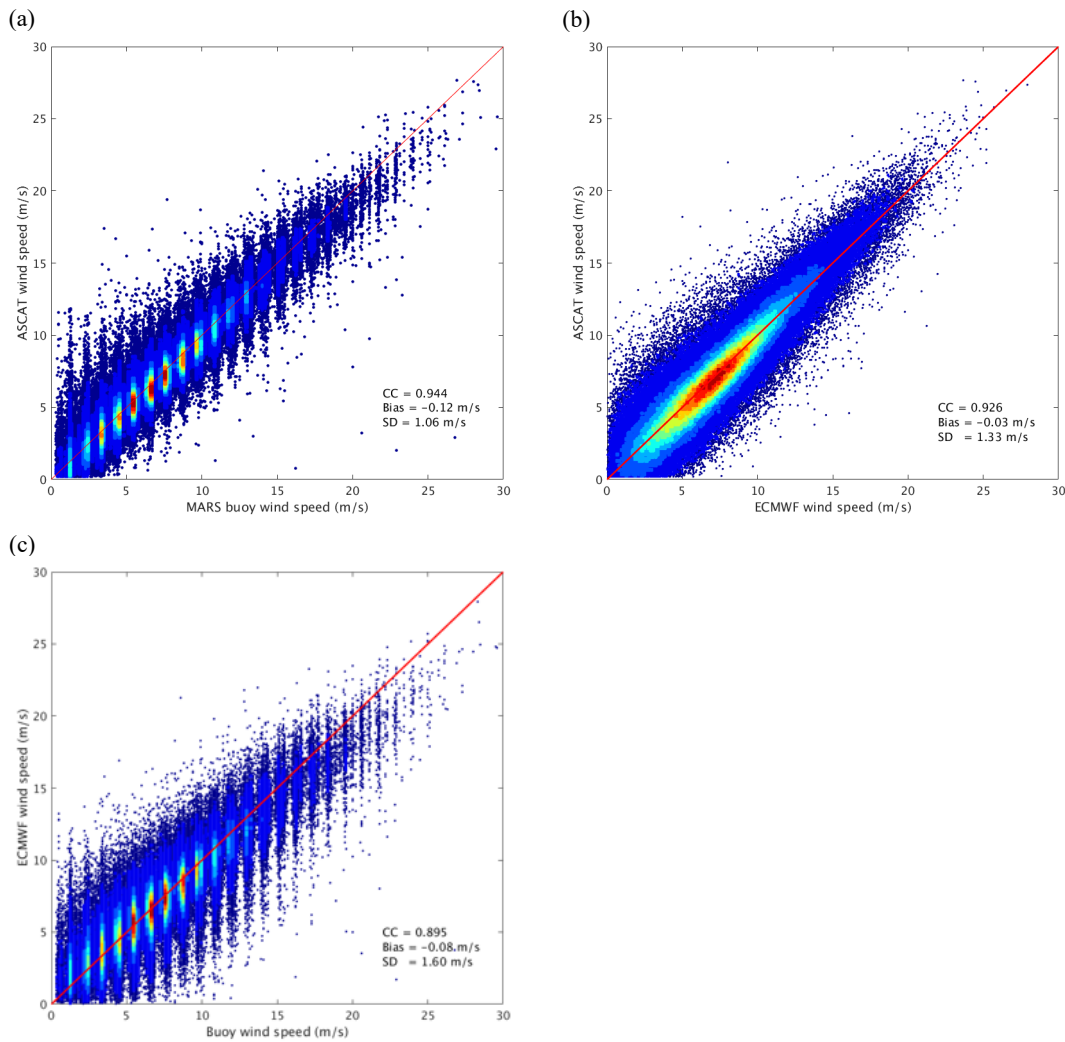


Figure 31. Scatter-density plot of (a) ASCAT  $U_{10S}$  wind speed versus MARS buoy  $U_{10N}$  wind speed; (b) ASCAT  $U_{10S}$  versus ECMWF  $U_{10N}$ ; and (c) ECMWF  $U_{10N}$  versus buoy  $U_{10N}$ . The scores of the correlation coefficient (CC), the bias, and the SD of the speed differences are shown in the legend. The total number of points is about 350,000.

Figure 32 shows the ASCAT  $U_{10S}$  wind speed bias w.r.t. MARS buoy  $U_{10N}$  winds as a function the mean ASCAT and buoy wind speed. Generally, the (negative) ASCAT wind speed bias increases with increasing wind speed, for mean winds above  $15 \text{ m s}^{-1}$ . Note from Figure 6, depending on the common MSL pressure at high winds, differences between  $U_{10N}$  and  $U_{10S}$  of  $0.5$  to  $1.0 \text{ m s}^{-1}$  appear quite plausible, hence conversion to  $U_{10S}$  is needed to evaluate the ASCAT biases found here.

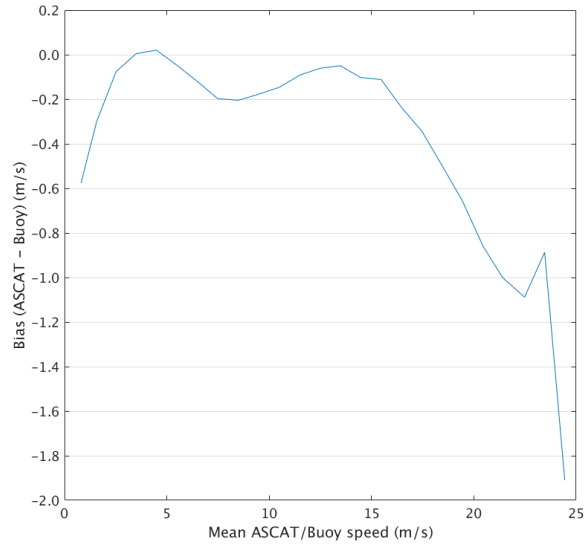


Figure 32. The bias of ASCAT  $U_{10S}$  wind speed w.r.t. MARS buoy  $U_{10N}$  winds as a function of the mean ASCAT/buoy wind speed.

The so-called triple collocation (TC) technique, first introduced by Stoffelen (1998) to estimate the uncertainties and calibration of three sea surface wind data sources, is adapted and used to estimate the uncertainties of the different wind sources (i.e., buoy, ASCAT, and ERA5). As discussed in Lin *et al.* (2015), it is very important to accurately estimate the representativeness error  $r^2$ , i.e., the common true variance of buoy ( $w_1$ ) and ASCAT ( $w_2$ ) not resolved by ECMWF ( $w_3$ ), in order to successfully estimate the individual random errors of each of the three collocated data sources. Here, the slope approach in Hoareau *et al.* (2018) is used to estimate the  $r^2$  value. That is, the  $r^2$  value that leads to well intercalibrated datasets (i.e., the regression slopes of  $w_3$  versus  $w_2$ , and  $w_3$  versus  $w_1$  are both close one) after TC is used. Note that this approach implicitly defines the calibration values through  $r^2$ .

Regarding the overall triple collocated dataset, the estimated  $r^2$  value is  $0.48 \text{ m}^{-2} \text{ s}^{-2}$  for both  $u$  and  $v$  components using the above mentioned method. Such value is smaller than the estimated value by integrating the difference between the scatterometer wind power density spectra (PDS) and the ECMWF model output PDS from the finest scatterometer scale of 25 km to the largest ECMWF error scale of 800 km ( $0.63 \text{ m}^{-2} \text{ s}^{-2}$  and  $1.00 \text{ m}^{-2} \text{ s}^{-2}$  for  $u$  and  $v$  components, respectively) (Vogelzang *et al.*, 2011). Probably, the underestimation of the  $r^2$  value is due to the fact that the ECMWF model is slightly biased low, while Horeau *et al.* assume calibration factors close to 1. Nevertheless, Table 1 and Table 2 present the main TC results of the overall triple collocations for different  $r^2$  values. It shows the estimated SD errors at ASCAT scale are nearly independent of the  $r^2$  value, except for the one of ASCAT  $v$  component.

Table 1. Triple Collocation scale factors (first row), bias corrections in  $m s^{-1}$  (second row), and error SDs in  $m s^{-1}$  at ECMWF (third row) and ASCAT scales (forth row), the  $r^2$  value is  $0.48 m^{-2} s^{-2}$  for both  $u$  and  $v$  components. Note that ASCAT is  $U_{10S}$  and ECMWF and buoys are  $U_{10N}$ .

	Buoy		ASCAT		ECMWF	
	$u$	$v$	$u$	$v$	$u$	$v$
Scaling factor	1.000	1.000	0.997	1.004	1.002	1.023
Bias correction	0.00	0.00	0.12	-0.03	0.18	0.03
SD error (ECMWF scale)	1.32	1.35	0.90	0.97	1.13	1.18
SD error (ASCAT scale)	1.13	1.16	0.57	0.68	1.33	1.37

Table 2. The same as Table 1, but the  $r^2$  value is  $0.63 m^{-2} s^{-2}$  and  $1.00 m^{-2} s^{-2}$  for  $u$  and  $v$  components respectively.

	Buoy		ASCAT		ECMWF	
	$u$	$v$	$u$	$v$	$u$	$v$
Scaling factor	1.000	1.000	0.997	1.004	0.997	1.003
Bias correction	0.00	0.00	0.12	-0.03	0.18	0.03
SD error (ECMWF scale)	1.38	1.53	0.98	1.21	1.06	0.91
SD error (ASCAT scale)	1.13	1.16	0.57	0.68	1.32	1.35

Since the wind variability (Figure 30) does not show remarkable changes at high wind conditions, the  $r^2$  value of the winds between  $15 m s^{-1}$  and  $25 m s^{-1}$  is considered to be similar to that of the overall dataset. Assuming the  $r^2$  value is that of Table 2, the TC results for only winds between  $15 m s^{-1}$  and  $25 m s^{-1}$  is shown in Table 3. The results indicate that, for high winds ( $w > 15 m s^{-1}$ ), both the buoy and the ECMWF wind quality degrade while ASCAT wind quality does not significantly vary. Note though that the TC results very much depend on the accuracy of the  $r^2$  estimates and the (TC model) assumption of unbiased and well-behaved wind component distributions, two conditions which are not really met after conditionally sampling at high winds.

### 5.3. Summary

In summary, although the TC-estimated wind quality shows some buoy wind degradation at high winds, Figure 31 clearly shows fairly good agreement between ASCAT and buoy winds, indicating that buoys winds between 15 and  $25 m s^{-1}$  can be used for calibration and verification purposes.

Table 3. The same as Table 1, but for the winds between  $15 m s^{-1}$  and  $25 m s^{-1}$ . The  $r^2$  value is  $0.63 m^{-2} s^{-2}$  and  $1.00 m^{-2} s^{-2}$  for  $u$  and  $v$  components respectively.

	Buoy		ASCAT		ECMWF	
	$u$	$v$	$u$	$v$	$u$	$v$
Scaling factor	1.00	1.00	1.01	1.00	1.06	1.03
Bias correction	0.00	0.00	0.13	-0.19	0.43	-0.04
SD error (ECMWF scale)	2.05	2.31	0.98	1.22	1.39	1.15
SD error (ASCAT scale)	1.90	2.08	0.60	0.69	1.60	1.52

Finally, we recall the earlier remarks in relation to Figure 6 and the common low PMSL at extreme winds in tropical hurricanes, resulting in differences between  $U_{10N}$  and  $U_{10S}$  of about 5%, hence conversion to  $U_{10S}$  remains future work to evaluate the ASCAT biases found here.

## 6. SENTINEL 1 AND SFMR WIND COMPARISON

Figure 4 depicts the tropical cyclone (TC) cases obtained with S1.

### 6.1. C-band cross-polarization signal wind sensitivity

Although a significant decrease of sensitivity of the VV co-polarization Normalized Radar Cross Section (NRCS) to ocean surface wind has been reported for wind speeds exceeding 25-35 m s<sup>-1</sup> (depending on the incidence angle and studies) (Carswell, 1999, Donnelly 1999, Soisuvarn et al., 2013), the implications on the wind speed retrieval quality and the exact trend of the NRCS dependency to wind remain a topic of debate for the speeds occurring in the strongest storms. As a matter of fact, the sensitivity analysis of the C-band backscattered signal to the ocean surface wind for speeds larger than 30 m s<sup>-1</sup> is directly limited by the lack of reference data and is addressed in this report. In this section we are mainly dealing with the backscattered signal from the ocean in cross-polarization (VH) as this radar parameter is more novel than co-polarization (VV), not yet measured by scatterometers and consequently even less accurately characterized. In general and despite the aforementioned existing limitations a consensus exists (Vachon and Wolfe, 2011, Zhang et al., 2012, Horstmann et al., 2013, van Zadelhoff, 2014, Hwang et al., 2015, Mouche et al., 2017, 2019) regarding the following facts :

- The VH backscattered signal is much lower than VV and more sensitive to noise;
- Backscattered signal dependency to incidence angle is much weaker in VH than in VV;
- Backscattered signal dependency to ocean surface wind direction with respect to the antenna look angle is much weaker in VH than in VV. Very few studies show this (Horstmann, 2013);
- The sensitivity decrease of backscattered signal dependency for increasing ocean surface wind speed is much weaker in VH than in VV.

To analyse the sensitivity of the C-band backscattered signal we adopt two complementary strategies:

- We co-analyse VV and VH NRCS without attempting to consider any wind speed as reference. This allows to overcome the issue of getting reliable reference data;
- We analyse VH NRCS with respect to ancillary wind information. SFMR wind speed measurements are used for TC where strong wind speeds are expected, whereas ECMWF wind vectors are used for situations corresponding to more moderate wind speeds. The signal sensitivity analysis independent should be independent of the source of the ancillary data.

### 6.2. Transects over Tropical Cyclones

Considering the high resolution of SAR, a straightforward test to directly evaluate the NRCS sensitivity is proposed. We simply analyse transects of NRCS as measured in category-5 TC in both co- and cross- polarization. As we specifically select the transects to be across the TC eye, we expect to see the backscattered signal by the ocean surface to increase from the TC centre (where minimum wind speeds are located) up to the centre of the eye-wall (where maximum wind speeds are located). Here, the TC category is given by analysis of experts in Regional

Specialized Meteorological Centres (RSMC), using independent data sets. We focus particularly on the strongest category to cover a large range of wind speeds and possibly depict the full dynamic range of the signal for each transect. The following two figures (Figure 33 and Figure 34) present VH NRCS images as obtained for category-5 TC and the associated transects for both VH (top) and VV (bottom). For each acquisition, the transect is done at a given fixed incidence angle (see legend). The maximum NRCS as observed in each polarization and on each side of the TC centre is indicated by a grey circle and its location with respect to the TC centre is highlighted by a vertical bar.

Figure 33 presents results for medium incidence angles around 30 degrees whereas the Figure 34 deals with large incidence angles around 35-40 degrees. The low incidence angle cases correspond to the Mangkhut and Jebi TC, which occurred in 2018. As observed, the NRCS in VH increases from the TC centre (0 km) to the centre of the eye wall around 22.5 km away from the centre. For larger radius, the VH NRCS decreases again. This shape is typical for TC ocean surface wind sections. The same analysis is conducted for VV and reveals an increase of the VV NRCS from 0 km to about 12.5 km (15 km and 10 km, for the Mangkhut and Jebi TCs respectively). Then, the VV NRCS remains essentially flat, where the VH NRCS is above 0.01. The same behaviour is obtained on the other side. The two sides of a cyclone can be distinguished as upwind, where the wind blows towards the SAR antenna, and downwind, where the SAR antenna and the wind point in the same direction. The halt in the VV NRCS increase at a smaller distance from the centre than for VH NRCS confirms a significantly reduced sensitivity of the backscattered signal in co-polarization with respect to cross-polarization at incidence angles of about 30 degrees.

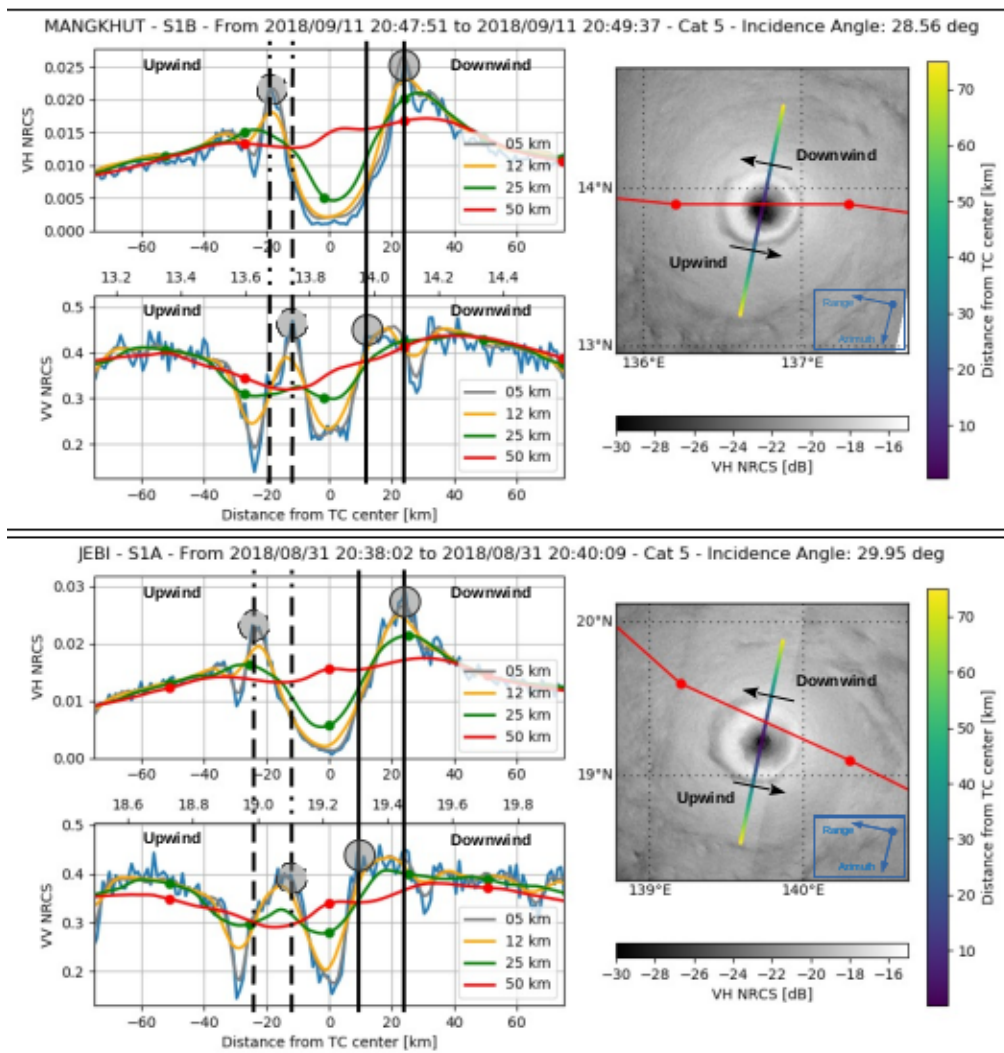


Figure 33. VH and VV NRCS transects across cat-5 TC for incidence angle of 30 degrees. To note, it seems that the saturation observed in VV signal occurs for VH NRCS values at about 0.01 (i.e., -20dB). From previous work, this roughly corresponds to ocean surface wind speeds of 30-35  $m s^{-1}$ .

When the incidence angle increases, this conclusion is not so clear anymore. In particular, we observe in Figure 34 that the VV and VH NRCS increase can go along over the same distance. In the case of Irma for instance, VV and VH NRCS increase during respectively 20 km and 22.5 km, reaching values of respectively 0.275 (-5.6 dB) and 0.0225 (-16.5 dB, corresponding to about 65  $m s^{-1}$ ) at 35.5 degrees. These two analysis confirm the decrease of the VV NRCS sensitivity loss when the incidence angle decreases, but also the higher sensitivity observed for VH. In addition, it can be noted that the width of the wind minimum in the TC eye where minimum NRCS values occur is always larger for VH than for VV. This indicates that VH NRCS as measured by C-band SAR (certainly depending on noise) is less sensitive to the ocean surface wind for low to medium wind speeds than VV NRCS.

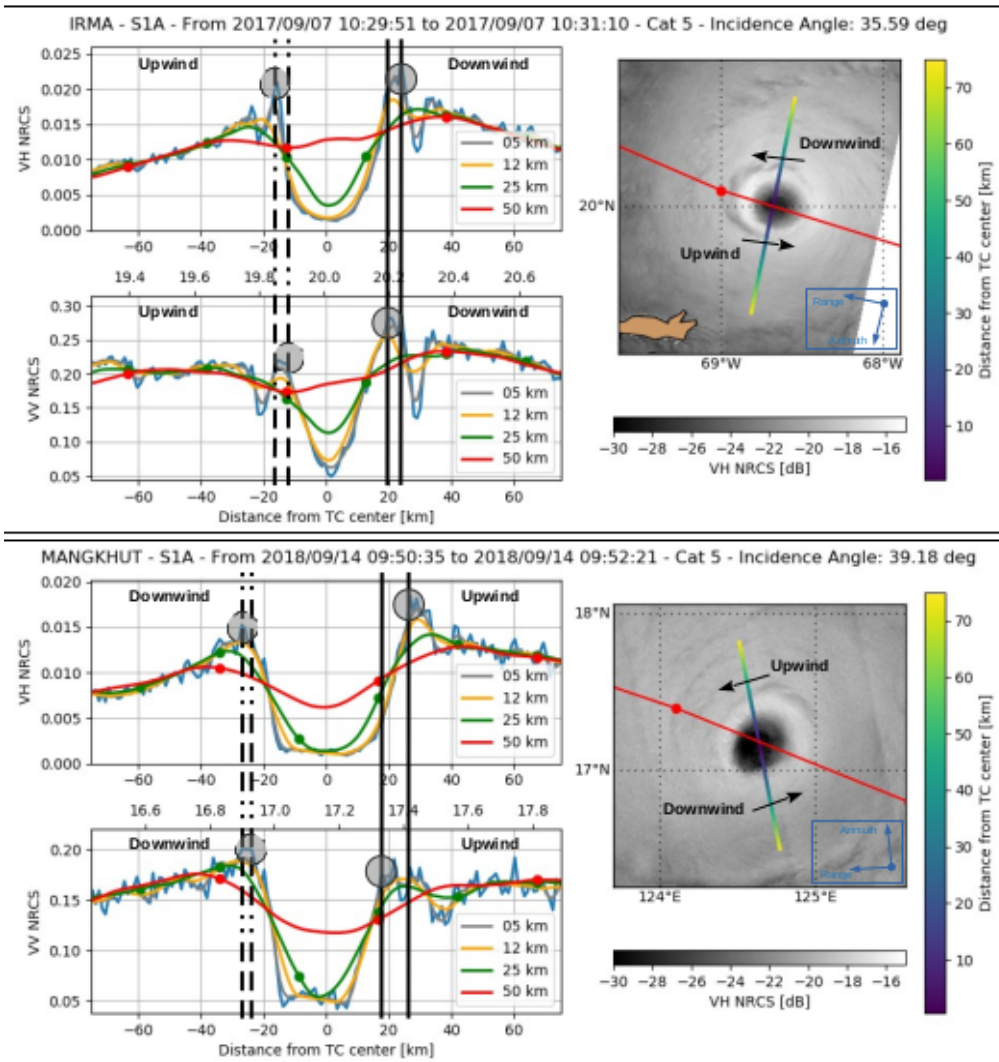


Figure 34. VH and VV NRCS transects across category-5 TC for incidence angles of 35 and 40 degrees.

Finally, for all cases presented here, we also notice a characteristic dark ring corresponding to a local minimum of NRCS in the signal for both co- and cross- polarization. As analysed in the case of acquisition over Irma, simultaneous measurements obtained with coastal rain radar from the NEXRAD network (Figure 34) exhibit strong values of radar reflectivity at the very same location (Mouche et al., 2019). This clear indication of a strong rain rate is further confirmed by SFMR measurements (see ). At this stage, there is no further elements to decipher between the possible contributions of rain attenuation and modification of the wind field dynamic that could both impact the NRCS. However, in the case of Jebi it is worth noting that the decrease in the VV-NRCS signal is larger than the decrease measured in the TC eye-wall. This most likely cannot be due to wind effects solely and indicates that the rain rate strongly affects the NRCS in such extreme cases. As observed in SAR data, close to the eye, those dark rings are more pronounced in co- than in cross- polarization. Finally, those dark rings are rather narrow (5 km) with respect to expected scatterometer nominal resolution (25 km) (Mouche et al., 2019). As such they are not expected to have a pronounced effect on the NRCS at medium resolution. Here, for

Mangkhut, in spite of almost a 60% decrease observed for VV-NRCS at 3 km resolution in the case of Mangkhut, a 20% decrease is obtained at 25 km, which corresponds to 0.8 dB, which would be a substantial change in scatterometer winds at  $40 \text{ m s}^{-1}$  due to the low wind sensitivity at these speeds and needs further investigation.

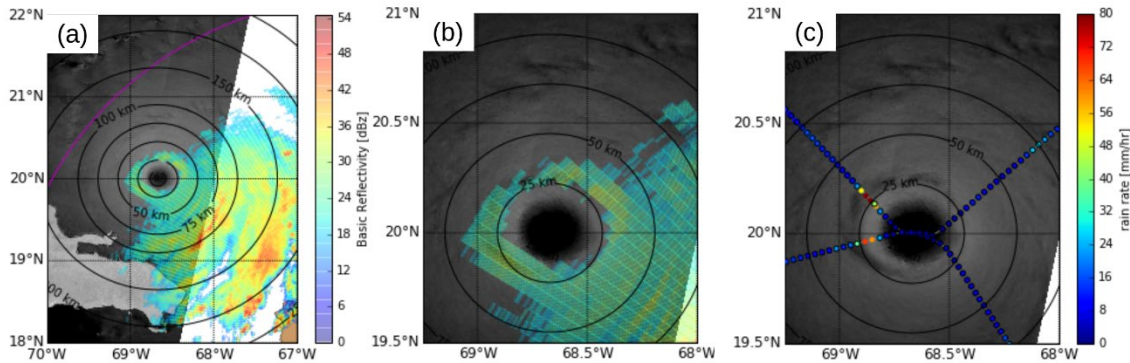


Figure 35. Rain during Irma category-5 hurricane on September 7, 2017. (a) Cross-Polarized Normalized Radar Cross Section and base reflectivity measured NEXRAD at the same time. Purple line indicates the limit of NEXRAD coverage (b) Same than (a) but zoomed on Irma eye. (c) Same than (b) but the colour code indicates rain rate measured by SFMR. Circles with (resp. without) black contours are considered as good (resp. bad) SFMR data as indicated by the product quality flag.

### 6.3. Signal sensitivity analysis with respect to ocean surface wind speed

In a number of papers the cross polarized signal (VH) from RadarSAT-2 and Sentinel 1 has been successfully used to link radar reflectivity to absolute wind speed (Vachon 2011, van Zadelhoff 2014, Hwang 2015) thanks to collocations with SFMR wind and rain measurements. In the van Zadelhoff et al. paper the RadarSAT-2 cross polarized VH signals were collocated to ECMWF forecast  $U_{10}$  wind speeds and the SFMR wind speeds, similar to the discussion in Section 4.3. It was concluded in the above-mentioned paper that the VH signal increases exponentially with wind speed and can be described as a combination of linear relationships in  $U_{10}$  vs. VH in [dB] up to at least  $45 \text{ m s}^{-1}$  based on the available data. There was indeed no wind direction angle relationship found and a small incidence angle dependence when using the RadarSAT-2 data.

In this section a description of a similar effort is outlined where Sentinel-1 VH SAR data from 32 tropical cyclones in 2016 and 2017 is collocated with available ECMWF and SFMR data. The analysis will be performed in two ways, one collocating the data to the SFMR native resolution and the second smoothing the SFMR measurements using an averaging moving window of 10 seconds and a spatial re-sampling at 3 km. During this pre-processing step, the quality flag included in SFMR data can be used to possibly filter out low-quality data. Second, the hurricane translation speed is computed from the hurricane track. In both cases the location of SFMR measurements are then shifted with respect to the time difference between each SFMR measurements and the SAR acquisition time using the TC motion vector. The duration of a SAR acquisition is typically a few seconds, whereas a flight with SFMR can last up to 6 hours and more. The SAR acquisition time is thus considered fixed with respect to the varying SFMR times.

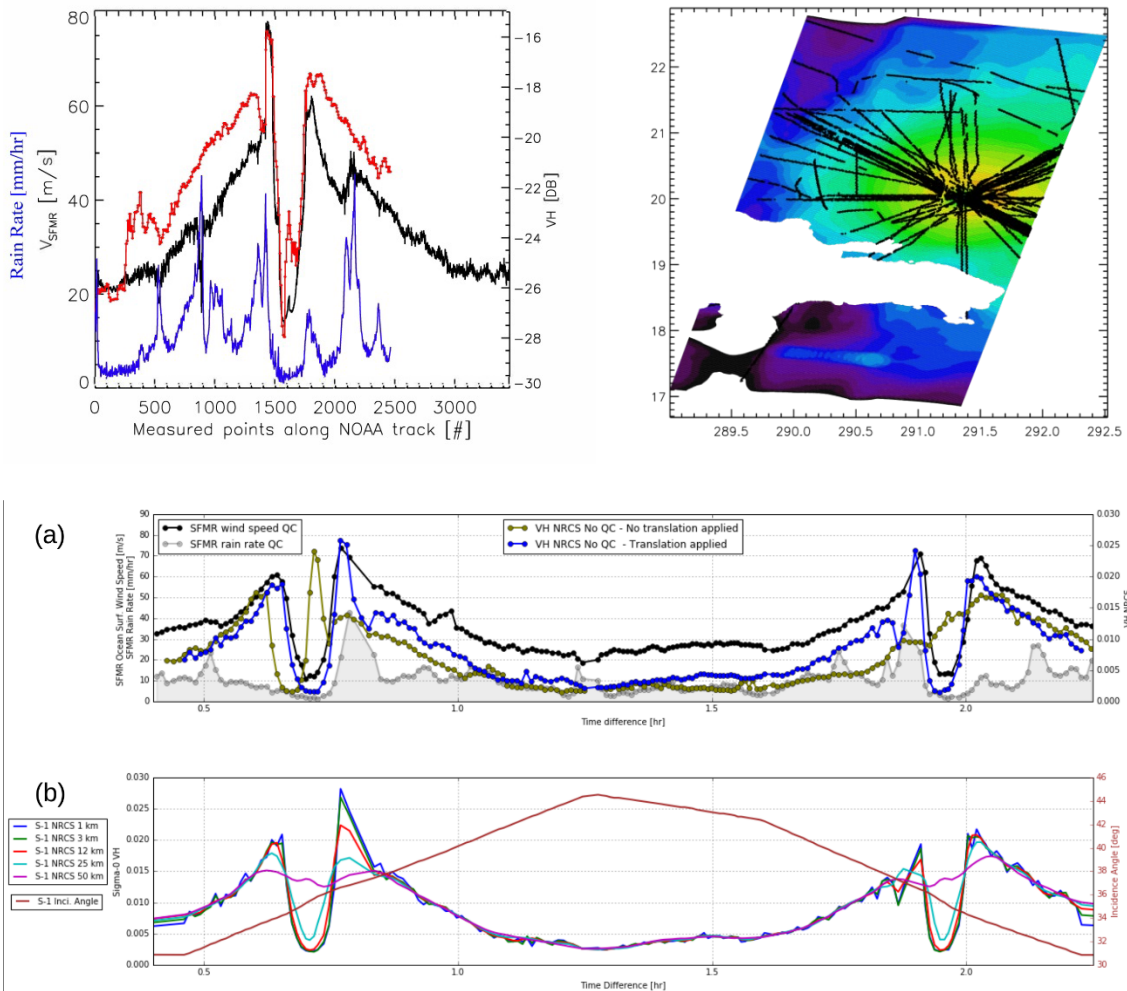


Figure 36. Left top plot: Flight track through Hurricane Irma (05-09-2017) with the SFMR retrieved wind speed (black), the SFMR rain rate (blue) and collocated Sentinel 1a VH cross-polarization radar signal (red) all at the SFMR resolution. Right plot: All collocated flight legs through Hurricane IRMA within two days of the Sentinel-1 observation (07-09-2017). The colour scale indicates the VH signal strength, the white area shows Cuba. Bottom two plots (a & b): Transect of collocated SFMR and SAR measurements at 3 km resolution. (a) Quality-controlled SFMR ocean surface wind speed (black) and rain rate (grey). NRCS in VH polarization with (blue) and without (olive) taking into account for Irma translation speed during the collocation (b). Same Sentinel-1 A NRCS transect than in (a) but for different resolutions (1, 3, 12.5, 25 and 50 km). Variation of SAR incidence angle along the transect is indicated in brown (right y-axis)

An example of the collocations obtained for Irma between Sentinel-1a and SFMR is given in Figure 36. In the top left panel a transect through Hurricane Irma is shown. Plotted are the retrieved SFMR wind speed (black line) measurements along the flight track and the collocated Sentinel 1a measured VH signal (red line) and the SFMR rain rate. A clear correlation is visible between the wind speed and VH signals. In the right panel the Sentinel 1a VH image from 07-09-2017 is depicted. Over plotted are all the available NOAA flight legs within 2 days of the Sentinel-1a overpass. Each of the individual legs passing through the hurricane eye is collocated to the VH image. They have been translated in latitude and longitude to the highest possible correlation taking into account only those observations with a rain rate below  $20 \text{ mm hr}^{-1}$ . The top left plot shows the collocation at SFMR resolution whereas Figure 36a(b) shows the

smoothed SFMR ocean surface wind speed and rain rate estimates as a function of time. Here the quality flag included in the SFMR data has been taken into account. The X-axis indicates the time difference with respect to the SAR acquisition time. In the present study, we only focused on collocations with an absolute time differences less than 2.5 hours. In this case, measurements have been measured by SFMR up to  $75 \text{ m s}^{-1}$ . These large values of wind speed strongly correlated with the highest values of rain rate, corresponding the western part of the TC eye, very close to Radius of Maximum Winds (RMW). The non-flagged observations appear to contain wind estimates where rain rates, which are discussed later, are up to  $40 \text{ mm hr}^{-1}$ .

To note, flagged measurements reach rain rates up to  $80 \text{ mm hr}^{-1}$ . This suggests that the quality procedure removes those measurements where rain is the most intense. Figure 36a also presents the collocated cross-polarized NRCS (blue) with respect to time corresponding to the same SFMR measurements. As observed and already reported with SAR data from the Radarsat-2 mission, there is a very strong correlation between SFMR ocean surface wind speeds and cross-polarized NRCS at C-Band (B. Zhang & Perrie, 2012). Figure 36a also shows the match-ups that result if the collocation procedure is not performed. The olive line shows NRCS that has not been aligned with TC motion. In this case the strong correlation between SAR and SFMR measurements is completely lost.

The impact of the different spatial resolutions is presented in Figure 36b. In this case, larger averaging areas blur the interpretation of the data; clearly showing that both the central wind minimum and peaked-ness of the wind maxima are severely impacted at spatial resolutions exceeding 12 km. In fact, at the time of acquisition, the eye diameter of Irma was about 30 km (about 16 nautical miles), as given by the Best-Track analysis, corresponding to less than 3 measurements at 25 km resolution. When the pixel sampling decreases, results are even worse (not shown). More generally, the use of SAR acquisitions with NRCS computed at different resolutions to systematically mimic lower resolution sensors can certainly help to characterize the resolution impact on the measurements depending on TC characteristics, particularly in the high wind-speed gradient areas near the RMW.

In the 2015-2017 period a number of very severe Hurricanes have been observed over the Atlantic by both Sentinels-1a and -1b and NOAA SFMR, increasing the maximum wind speed up to  $75 \text{ m s}^{-1}$  (see top Figure 36 for a transect through Hurricane Irma) . Next to this a number of Pacific and Indian Ocean tropical cyclones (typhoons) have been measured which have been collocated with ECMWF forecast data. By combining all the available collocated legs from the eight SFMR measured Atlantic hurricanes in the 2016 and 2017 period, the 2-D joint distribution shown in Figure 37 (blue contours) is created.

In Figure 37 a combination of three distributions is show. The solid contours depict the collocation of ECMWF forecast data with the 32 tropical cyclones for which Sentinel-1a and -1b observations were available in 2016 and 2017. Note that even for the strongest cyclones the ECMWF absolute stress equivalent wind speed ( $U_{10s}$ ) is hardly ever greater than  $40 \text{ m s}^{-1}$ . Over plotted are the results from the van Zadelhoff et al. (2014) results, where SFMR data was collocated with RadarSat-2 VH SAR data. The two red dashed lines indicate the relationships described in the above-mentioned paper, where the low-to-strong wind-speed regime ( $< 20 \text{ m s}^{-1}$ ) is described by the relationship found by Vachon and Wolfe (2011). This relationship is based on buoy comparisons to RadarSat-2 data. The strong-to-severe wind regime ( $>20 \text{ m s}^{-1}$ ) is based on the RadarSat-2 VH-SFMR wind speed data (green contours). The strong hurricanes observed

by the Sentinel-1 satellites expand parameter space up to  $\sim 75 \text{ m s}^{-1}$ , whereas the former RadarSat-2 dataset reached up to  $45 \text{ m s}^{-1}$ .

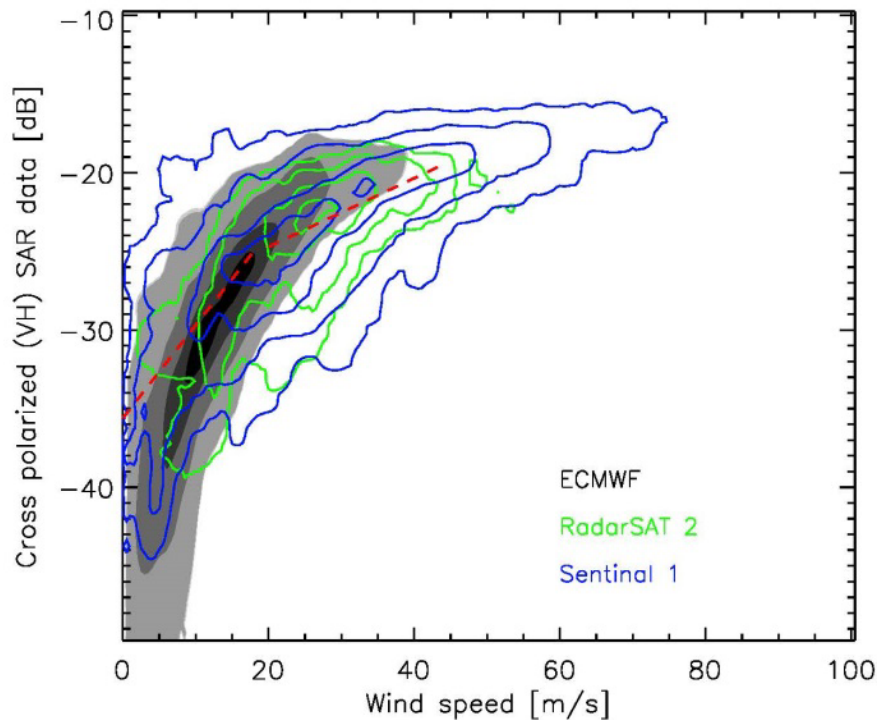


Figure 37. Distribution of VH SAR data versus wind speed for three datasets. The solid shading shows the collocated ECMWF  $U_{10S}$  forecast data with the Sentinel-1 SAR data. The green contours depict the results from the van Zadelhoff et al. (2014) paper comparing RadarSat-2 vs SFMR wind speeds and the blue contours present the results from Sentinel-1a and -1b VH observations vs. SFMR wind speeds for the 2016 & 2017 Hurricanes. The red dashed lines shows the Geophysical Model Function (GMF) as described in the above-mentioned paper. Note that the spatial resolution in ECMWF TCs is much lower than that in SAR.

The simple, with respect to VH in dB, linear relationship for the extreme wind speed is reasonable up to  $45 \text{ m s}^{-1}$ , maybe slightly too low with respect to the Sentinel-1a measurements, but exceeds the measurements for higher wind-speeds, where the distribution shows a lower slope. Nonetheless, there appears useful sensitivity up to  $\sim 70 \text{ m s}^{-1}$ .

When looking at the 3-km resolution collocated measurements and using a more severe quality-control on the SFMR measurements one can now more precisely document the relationship between cross-polarized NRCS and ocean surface wind speeds, including local extremes up to  $75 \text{ m s}^{-1}$ . For this purpose, Sentinel-1 and RadarSat-2 data are combined. Especially for weak cross-polarized backscattered signals, the signal-to-noise ratio is a key measurement, highly dependent upon the accuracy of the noise annotated in the SAR products. To note, noise corrections were often neglected (B. Zhang & Perrie, 2012), or not always properly taken into account for the entire data set (Hwang et al., 2015). Here, all SAR data are noise-corrected before collocation.

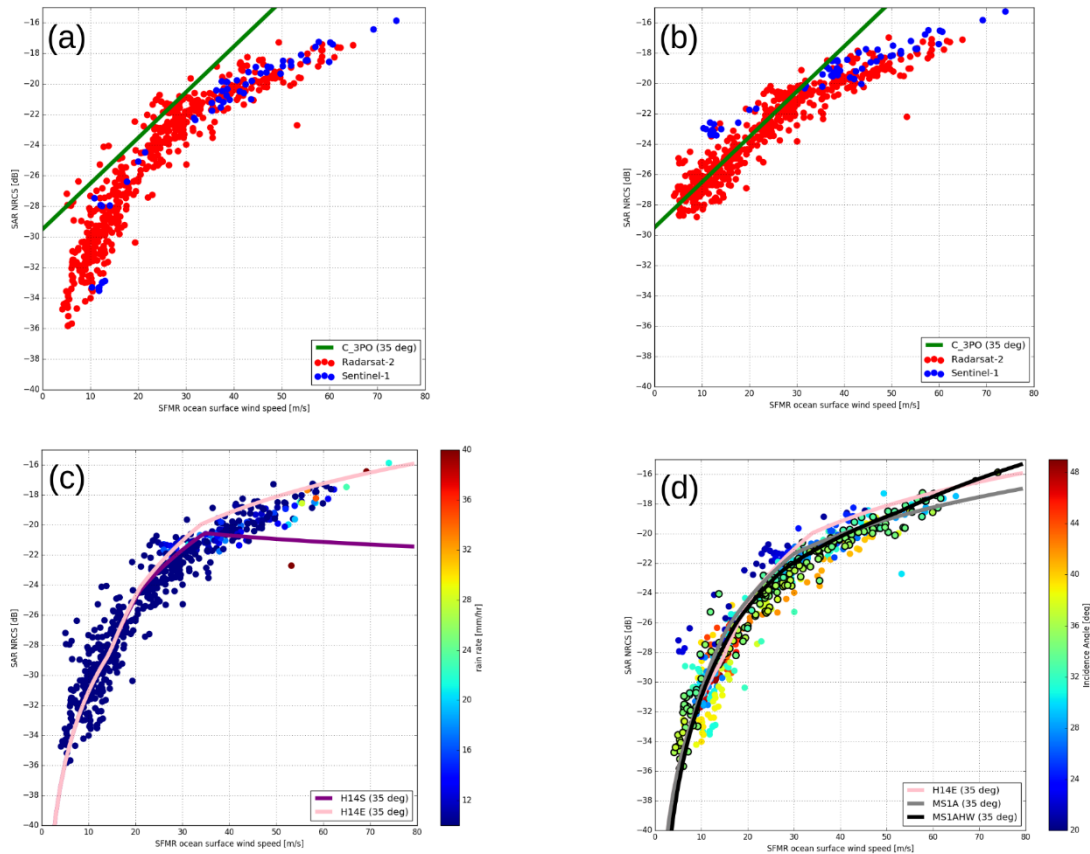


Figure 38. 3-km Sentinel-1 A (blue) and Radarsat-2 (red) NRCS in VH polarization (a) with noise correction (b) without noise correction and as a function of the ocean surface wind speed measured by SFMR. The green solid line stands for the Geophysical Model Function (GMF) proposed by G. Zhang et al. (2017). (c) Same than in (a) but with colour code indicating SFMR rain rate. Pink and purple solid lines respectively indicate the H14E and H14S GMFs from Hwang et al. (2015). (d) Same than in (a) but with colour code indicating SAR incidence angle. Pink and grey solid lines respectively indicate the H14E GMF from Hwang et al. (2015) and MS1A GMF from A. Mouche et al. (2017).

The impact of the ocean noise correction on the NRCS and its relationship with ocean surface wind speed is illustrated in Figure 38a without noise correction and Figure 38b with noise correction. Both cases show that the NRCS clearly increases with ocean surface wind speed, without any apparent NRCS saturation in wind speeds up to  $75 \text{ m s}^{-1}$ . With or without noise correction, these comparisons confirm the substantial potential of C-Band cross-polarized NRCS for retrieving oceanic surface wind speeds in TC environments over TCs, including category 4 and 5 hurricanes. Nonetheless, the NRCS to wind relationships, obtained with and without noise correction, are impacted by noise over the whole range of wind speeds. As anticipated, this impact can become particularly significant for the lowest branch of the high wind speed range ( $\sim 20 \text{ m s}^{-1}$  wind speed). Without noise correction, our present analysis consistently recovers previously reported relationships (Geophysical Model Function or GMF) between NRCS and wind speeds, especially those developed for wind speeds lower than  $30 \text{ m s}^{-1}$  (B. Zhang & Perrie, 2012; G. Zhang et al., 2017). The application of noise correction fully explains the difference observed between our analysis and reported GMFs in this range of wind speeds. For higher than  $30 \text{ m s}^{-1}$  wind speeds, these GMFs are not adapted, and simply fail to explain the collected data. The present analysis

demonstrates that noise corrected NRCS values increase from about -36 dB at 5 m s<sup>-1</sup> up to -16 dB at 70 m s<sup>-1</sup>.

This analysis also reveals the great consistency of the two different SAR missions (RadarSat-2 and S1) after calibration. This clearly demonstrates the potential to systematically combine the different instrument measurements in order to increase the temporal sampling of a given storm. In the following, we only consider NRCSs corrected for the noise annotated in the product.

Comparisons with other existing GMFs are presented in Figure 38c. The two GMFs proposed by (Hwang et al., 2015) display significantly different behaviours for wind speeds higher than 35 m s<sup>-1</sup> - note the relative saturation in the H14S GMF. The present analysis reveals that, between 35 and 70 m s<sup>-1</sup>, H14E GMF is clearly more adapted than H14S GMF. For this figure, the rain rate measured by SFMR is also reported. In our analysis, data show no evidence of significant degradation due to the presence of precipitation. For wind speeds between 5 and 30 m s<sup>-1</sup>, the rain rate is lower than 20 mm hr<sup>-1</sup>, and its effect on NRCS computed at 3 km resolution is hardly visible. Few measurements with rain rate between 20 and 40 mm hr<sup>-1</sup> and wind speeds larger than 30 m s<sup>-1</sup> have been collected, and in those cases, precipitation impacts are unclear. It is however noteworthy that around 52.5 m s<sup>-1</sup> wind speed, an outlier in NRCS is obtained for 40 mm hr<sup>-1</sup> rain rate. This latter result tends to indicate possible significant decreases of NRCS for high rain rates (see previous section for a discussion based on comparisons against NEXRAD radar).

In Figure 38d colours provide the SAR incidence angles. Overall, NRCS measurements decrease when the incidence angle increases. Here, this decrease can be observed up to 50 m s<sup>-1</sup>. This result agrees with previous studies (Hwang et al., 2015; Mouche et al., 2017; G. Zhang et al., 2017). The lack of cases at higher wind speeds prevents any conclusion of the impact of incidence angle on NRCS at those speeds. Future studies that make use of larger numbers of cases will be used to address this issue. Results of H14 E GMF from Hwang et al. (2015) and MS1A GMF from Mouche et al. (2017), are reported at 35 degree incidence angle and also shown in Figure 38. For comparison, circles surrounded with black lines indicate measurements with incidence angle between 32.5 and 37.5 degrees. Both GMFs agree quite well with the data. At wind speeds above 30 m s<sup>-1</sup>, differences appear, with an overestimation of the NRCS for H14E GMF between 30 and 60 m s<sup>-1</sup>, and an underestimation of the NRCS for MS1A GMF for wind speeds larger than 50 m s<sup>-1</sup>. This is not surprising. The H14E GMF has been derived with wind speed measurements up to 40 m s<sup>-1</sup>, while the MS1A GMF definition relies on medium-resolution wind speed from SMAP L-Band radiometer up to 50 m s<sup>-1</sup>. This new data set can be used to refine the existing GMF, provided that they are calibrated with respect to an in-situ reference, possibly extending the validity to ocean surface wind speeds up to 70-75 m s<sup>-1</sup> roughly.

#### 6.4. Saturation of VH signals

In van Zadelhoff et al. (2014) the highest VH measurements were compared to the Tropical Cyclone Best Track record, a product from the NHC GIS. This Best Track is a subjectively-smoothed representation of the tropical cyclone's location and intensity and may therefore differ from the true values. The intensity is described as its maximum 1 minute sustained surface wind speed and minimum sea-level pressure at 6 hour intervals over its life time. The track and intensity values are determined as a post-storm assessment of all available data. The track data itself is intended for regional-scale analysis and will not show the Hurricane's erratic motions

over its life time. The VH images and their retrieved velocities are independent of the NOAA best track assessment data and describe the hurricane in a very different manner. The VH-GMF results are based on a high spatial resolution snapshot, whereas the NOAA best track is a single intensity value of maximum sustained wind depending on time, for which the variability has to be treated in a different way. For the VH-GMF, only the tail of the image distribution is important since it describes the highest wind velocities. In the case of the 1-minute maximum sustained winds the most important issue is its stability in time, since this describes how stable the wind speed estimate is at the time of the SAR overpass.

For each Hurricane image, the best track intensity (i.e., from NOAA) is estimated by interpolating the maximum velocity to the satellite overpass time and the associated error is defined as the standard deviation of the 5 closest points of the respective best track, i.e., the more variable the Hurricane is over this time span, the larger the local error bar. For the retrieved VH-GMF velocities, a land-sea mask is applied to disregard high VH values due to land return. If one would subsequently take the highest wind speed in the image, the value could depend on high returns from non-sea-surface targets, e.g., coastlines or small islands, that weren't removed by the land-sea mask operation, ships or an occasional single high noise pixel. Instead of comparing the maximum retrieved wind speed, the 0.995 and 0.9995 percentile wind speed values are retrieved with the centre defined as its mean velocity value to ensure a robust retrieved value. These values are specific for the used swath and resolution of the respective SAR instrument. In the comparison between the RadarSat-2 data and best track data a linear trend was observed taking into account all available SAR images.

The same procedure has been followed for the available Sentinel-1 images (Figure 39). The individual tropical cyclone images are color-coded according to the region they were observed, where the 'trades' indicate latitude's between 0 and (+ or -) 30 degrees. The solid dashed line shows the results (incl. range) from the RadarSat-2 dataset. The Sentinel-1 results show very similar results for 1-minute maximum sustained wind speeds up to 60 -70  $\text{m s}^{-1}$ , albeit a slightly lower velocity with respect to the cross-polarized 0.995-0.9995 percentile range from RadarSat-2. This could be due to differences in resolution and calibration between the two satellites. It becomes more interesting around the 70  $\text{m s}^{-1}$  range where the maximum sustained 1-minute wind speed can be determined based on the highest VH values within the respective image. The best track values are estimates based on all the information available, this means that it may not represent the true value, the aim of plotting the standard deviation of the signal is to take this into account.

A number of the (trades) Atlantic and Caribbean cyclones have been flown through by NOAA aircraft, which provides more credibility to these specific best track estimates, some of which lie in the top of the graph.

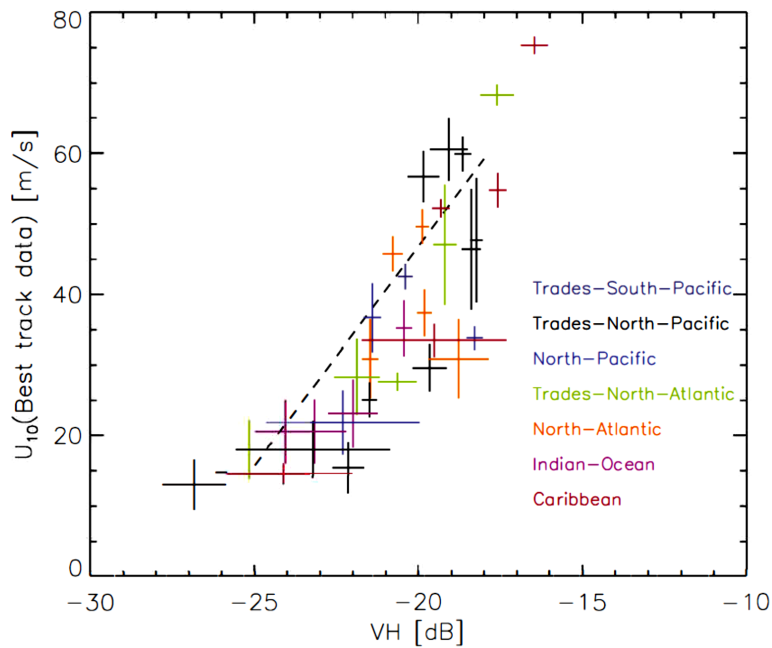


Figure 39. Comparison of the maximum 1-min sustained surface wind speed best-track estimates versus the averaged sum of the VH-GMF retrieved velocities of the 0.995 and 0.9995 percentiles for each hurricane. The error estimates in the x direction show the two percentile values and represent the variability close to the eye within the image, the y direction error bar shows the standard deviation within a 24 h window around the VH measurement, indicative of the variability of the Hurricane as a whole. The color indicates the region in which each hurricane was observed. The dashed line shows the linear relationship from the van Zadelhoff et al. (2014) paper, based on RadarSat-2 observations.

Combining the information from Figure 37 to 39, the SFMR-retrieved wind speed indicates one can retrieve VH wind speeds up to at least  $\sim 70 \text{ m s}^{-1}$ , even though the slope becomes more and more shallow, i.e., with lower skill. Similar information is provided by the best-track information, which is linearly rising up to around the same 1-minute sustained wind speed of  $\sim 70 \text{ m s}^{-1}$ , i.e., up to the maximum wind speed of a Category 4 hurricane on the Saffir-Simpson hurricane scale. This also shows that most of the wind-speeds will be retrievable using a SAR instrument within a category 5 hurricane, except perhaps for the most inner region (close to the eye), where the signal may have reduced sensitivity. Since most of the hurricane has however been detected, the wind speed distribution in this most inner region can be well estimated by combining hurricane models with the measurements in the outer region of the hurricane.

Especially when considering that future operational scatterometers with VH capabilities (MetOp-SG SCA) will have a far lower resolution compared to the SAR data considered here, one should expect that the absolute wind speeds for all types of tropical cyclones will be retrievable using straightforward guidance for the 1-minute sustained winds (see Figure 39).

Up to this point all the results presented above, using Sentinel-1 data, have been combined indiscriminately of where the tropical cyclone was situated. In Figure 40 the hurricanes are organized according to their 'ocean basin'. Depicted are the median VH backscatter data within  $2 \text{ m s}^{-1}$  velocity bins for all collocated points within their respective basin. In the lower end of the wind speed distribution the signals are close to equivalent noise level and scatter a lot. Between 10 and  $25 \text{ m s}^{-1}$  the median lines are well within the local standard deviations of the

distributions. This is also the case for the velocities between 25 and 40 m s<sup>-1</sup>, except for the Indian-Ocean basin, which consisted of 4 cyclone observations. Three of those showed a maximum velocity ~25m s<sup>-1</sup> and follow the median lines in the figure. The lower median VH values between 25 and 40 m s<sup>-1</sup> all originate from a single observation of tropical cyclone Dineo, just before the eye reached the coast of Mozambique. It is likely that neither the closest ECMWF forecast used did represent the cyclone well at time of the observation, resulting in this one outlier of the 32.

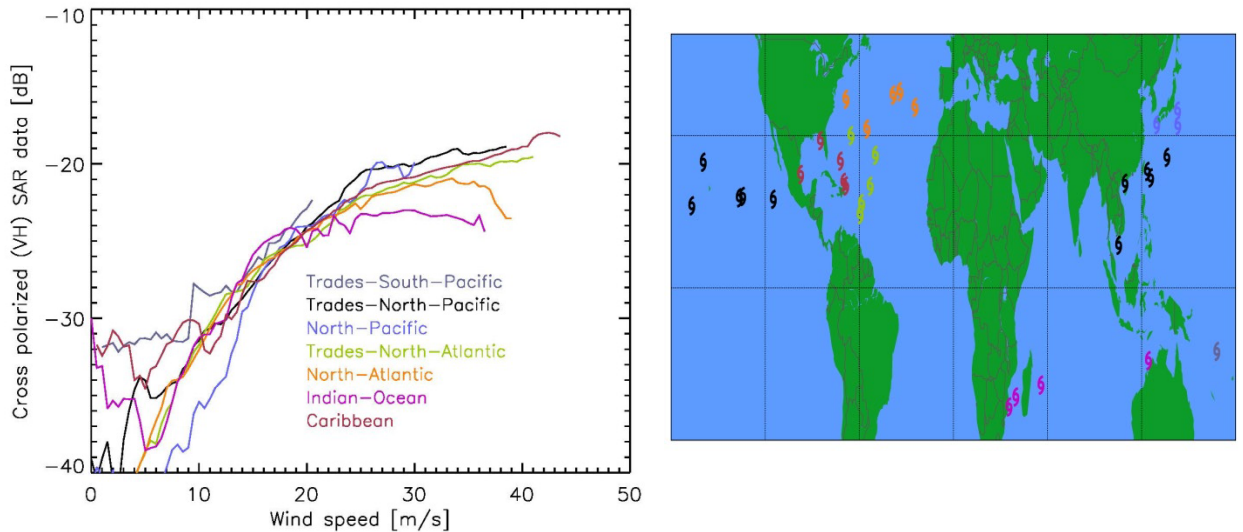


Figure 40. Left panel: Distributions of all the forecasted ECMWF stress equivalent wind speeds ( $U_{10s}$ ) versus collocated VH measurement points from the hurricanes within individual ocean basins. The lines show the median backscatter within 2 m s<sup>-1</sup> velocity bins for the distribution, color-coded according to the basin. In the right panel the position of the 32 tropical cyclones considered in this study is shown at the time of the Sentinel=1 overpass.

To conclude, the simple relationships shown in this and previous studies suggest the potential use of the VH measurements for a near-real-time wind speed assessment in the case of Hurricanes and Typhoons, thereby enabling hurricane prediction centres to improve their forecasts and potential safety and damage advisories. The VH signal has a positive skill with respect to wind speed up to 75 m s<sup>-1</sup> (Category 4 Hurricanes). No geolocational differences have been found between ECMWF wind speed forecast and the measured VH signals, making any potential VH-GMF globally valid. However, to date the only option to better describe the GMFs, depends on the number of available collocated SAR/SFMR measurements and possible refinements in the SFMR wind measurements quality. Furthermore, high-resolution data allow to mimic lower resolution measurements. This can be used to assess the impact of the resolution for deriving TC guidance parameters such as the maximum sustained 1-minute wind speed and radius of maximum wind speed. Indeed, as radius of maximum wind speed is expected to be below 40 km for cat-2 TC and higher, a medium resolution Level-2 product may not be able to provide a direct estimate of such parameters, but guidance based on the available measurements may be developed.

The VH signals have been linked here to the SFMR wind speed and are therefore not absolutely calibrated. A future VH-GMF will require absolutely calibrated SFMR wind speeds, i.e., through buoy wind and/or dropsonde references, for the entire wind speed range to be useful for Hurricane centres.

## 6.5. Analysis against L-Band Brightness temperature

Foam coverage and thickness conditions resulting from breaking waves explain the increase in the low-frequency (1.4–7 GHz) microwave emissivity of the ocean surface in storms (Reul et al., 2003). A monotonic increase in the latter with respect to ocean surface wind speed is observed. Since the first paper on L-Band brightness temperature,  $T_B$ , analysis as measured by SMOS over TCs (Reul et al., 2012, 2016), to show the high sensitivity of L-Band radiometers to extreme ocean surface wind speed and its low contamination by rain, several papers has been published to take benefit of these properties and developed Level-2 wind speed products (Meissner et al., 2017; Yueh et al., 2016; Reul, 2017). As compared to scatterometers, this is a rather new application and several open questions are still remain regarding the validity of these products. Inter alia, on the same issue than scatterometers, regarding the in-situ wind speed reference for calibration and the procedure to estimate parameters such as the maximum sustained wind speed for operational hurricane centres, due to the relatively low spatial footprint and its smearing effect on wind speeds.

Hereafter, we intentionally disregard the ocean surface wind speed from models or buoys, to take full advantage of the precise collocations (within 60 min) between the NRCS acquired in co-polarization and cross-polarization by C-band (5.405 GHz) synthetic aperture radars (C-SARs) onboard ESA’s Sentinel-1 missions and the brightness temperatures from the SMAP L-band radiometer. This approach prevents any issues regarding the geophysical model function definition, inversion scheme, and reference data quality. Moreover, from a sensor physics point of view, roughness, sea foam and resulting NRCS and brightness temperature changes can be directly related to the energy flux per unit area (Newell and Zakharov, 1992) and can thus be considered as a direct tracer of the air–sea momentum fluxes.

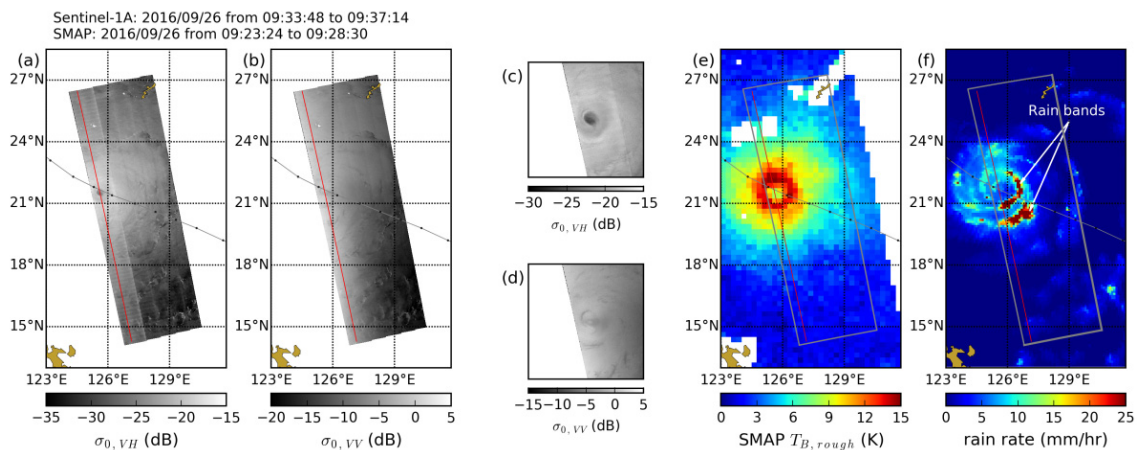


Figure 41: (a) Images of TC Megi on September 26, 2016. (b) Images of Sentinel-1  $\sigma_{0,VH}$  and  $\sigma_{0,VV}$ . (c) and (d) Enlarged images of  $\sigma_{0,VH}$  and  $\sigma_{0,VV}$  around the storm eye. (e) SMAP  $T_{B,rough}$ . (f) IMERG rain rate. Red straight lines across storm eye indicate a transect. Gray dotted curves indicate the track of storm.

Figure 41 presents acquisitions of the different types of data used in this report for the particular case of Typhoon Megi on September 26, 2016, at about 9:30 Universal Time Coordinated (UTC). At this time, the intensity of Megi from the best track data indicates Category 2 on the Saffir–Simpson scale with a maximum 1-min sustained surface wind speed of 95 and 90 knots, at 6:00 UTC and 12:00 UTC, respectively. The storm eye is clearly observed in SMAP  $T_{B,rough}$  and Sentinel-

1 NRCS in VH-polarization ( $\sigma^{0,VH}$ ) and is surrounded by a ring of brighter signal showing a maximum at about 50 km from the storm centre. Here, the storm centre defined by the minimum of SMAP  $T_{B,rough}$  is located at 21.6°N, 125.7°E. The shape of the eye is less obvious in the co-polarized NRCS ( $\sigma^{0,VV}$ ) signal. This is in line with the reported sensitivity of the co-polarized and cross-polarized NRCS across the storm's eye as analysed by Mouche et al. (2017). At SMAP and Sentinel-1 acquisition times, IMERG rain rate reaches maximum values around 50 mm/h found in two spiralling bands of heavy rain on the southeast of the storm centre (see annotations in Figure 41).

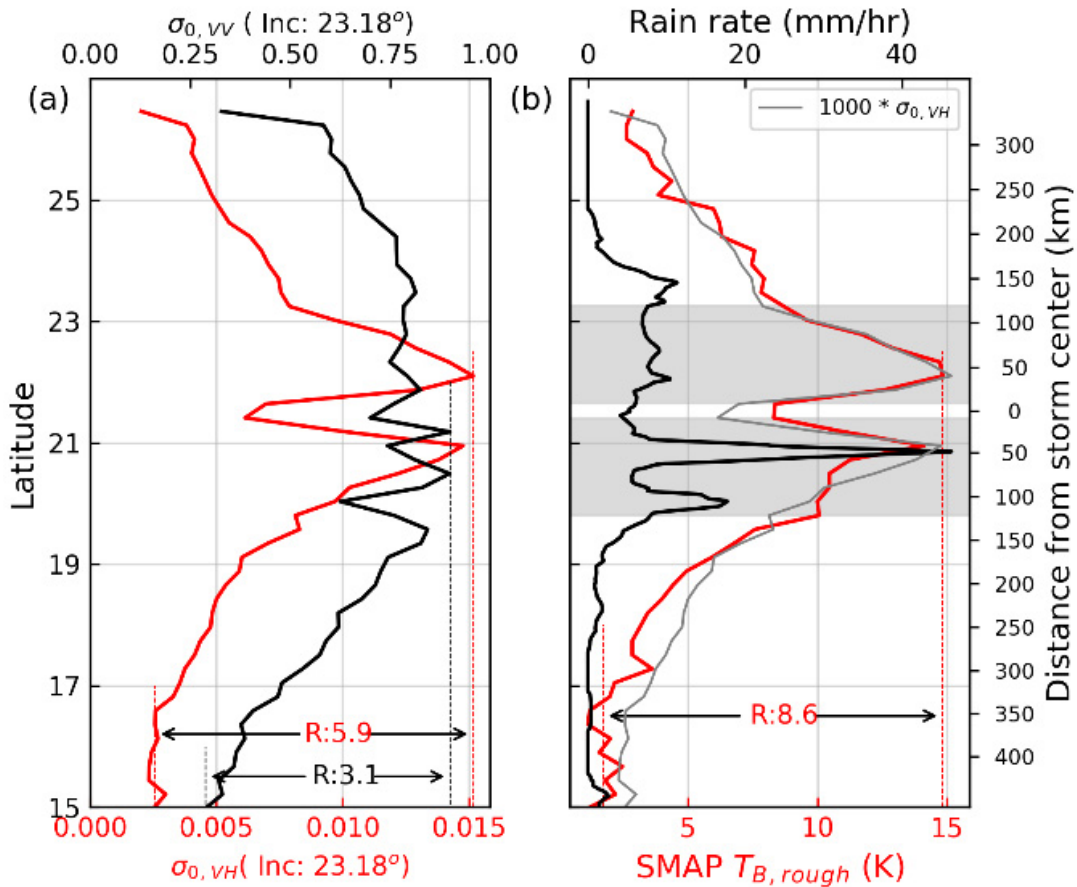


Figure 42: Analysis along transects across a TC eye. (a) Sentinel-1  $\sigma^{0,VH}$  and  $\sigma^{0,VV}$  on a grid of 25 km at different latitudes, where the red and black line represent  $\sigma^{0,VH}$  and  $\sigma^{0,VV}$ , respectively. (b) SMAP  $T_{B,rough}$  and IMERG rain rate at different latitudes, where the red and black line represent  $T_{B,rough}$  and rain rate, respectively. R gives the ratio of the values indicated by arrows.

A transect (red line) across the storm eye and the two rain bands is selected at a fixed incidence angle for Sentinel-1. As such, effects due to incidence angle variation or noise fluctuation across the swath are removed. As shown in Figure 42, when compared at a similar spatial resolution,  $\sigma^{0,VH}$  and SMAP  $T_{B,rough}$  display similar increase from the outer storm eye to the storm eye wall. The signal structures around the storm eye are also very consistent in both active and passive measurements. The magnitude between the outer storm signal values at 16.0°N and at 22.0°N (where the maxima are detected) is about six for  $\sigma^{0,VH}$  and nine for  $T_{B,rough}$ . A factor of about 1,000 is found between  $\sigma^{0,VH}$  and SMAP  $T_{B,rough}$ . Indeed, when taking into account this factor (see Figure 42), C-band  $\sigma^{0,VH}$  and L-band  $T_{B,rough}$  profiles across Megi hurricane are almost identical. In

contrast to  $\sigma^{0,VH}$ ,  $\sigma^{0,VV}$  clearly saturates between 19°N and 24°N close to the storm eye. For this transect, the magnitude of  $\sigma^{0,VV}$  between lowest and highest values is about three.

For this particular TC case, the two major rain bands as detected in the IMERG product are about 25 km wide. The band closest to the storm eye has a maximum rain rate of about 40 mm/h at 25-km resolution and is crossed by the selected transect at 20.9°N. The second band has a rain rate of about 20 mm/h and is located at 20°N, about 100 km from the storm centre, where the hurricane wind speed is expected to decrease. It is difficult to precisely quantify the rain impact on both C-band  $\sigma^{0,VH}$  and L-band  $T_{B,rough}$  from a single example. The performances of the merged IMERG rain measurements product in the specific case of hurricanes are also uncertain. To compute the L-band  $T_{B,rough}$ , the contributions of the SST and SSS to the signal are removed. In such an extreme case, intense rain conditions may significantly affect SST and SSS and results in brightness temperature modifications. As a matter of fact, we observe that the linear relationship between L-band  $T_{B,rough}$  and C-band  $\sigma^{0,VH}$  is not anymore valid in the southern part of the eye where much more intense rain is observed than that in the northern part of the eye.

When comparing the southern and northern areas of the transect (see grey areas in Figure 42 on each side of the eye), it can be seen that the two signal profiles are quite different near the peaks. This is particularly true for the L-band  $T_{B,rough}$ . A broader shape is found near the location of the second rain band, whereas a narrower shape is found near the location of the first and more intense rain band. For C-band  $\sigma^{0,VH}$ , we observe very similar shapes between northern and southern parts of the transects. In this case, where NRCS has been spatially averaged over 25-km, this tends to indicate a small impact of heavy rain on C-band  $\sigma^{0,VH}$  when wind speed is more intense (here we are close to the eye). We also note fluctuations in the NRCS near the location of the second and weaker rain band where the wind is expected to be lower (far from the eye). This may indicate a possible increase of C-band  $\sigma^{0,VH}$  due to rain for moderate or low winds (Xu and Stoffelen, 2019). Contrary to the  $\sigma^{0,VH}$  profile, the  $\sigma^{0,VV}$  one's exhibits a significant decrease (by a factor of 50%) coincidentally with the two rain bands. This would be unlikely due to rain cloud effects, as these are similar to cross- and co-polarisation, but could be due to wind direction changes, away from the downwind maximum. It would be of interest to investigate more of such cases nearby rain.

### Statistical Analysis

Analyses by Yueh et al. (2016) and Meissner et al. (2017) both show that  $T_{B,rough}$  in horizontal ( $T_{Bh,rough}$ ) and vertical ( $T_{Bv,rough}$ ) polarizations start to approximately linearly increase with ocean surface wind speed for values greater than  $11 \text{ m s}^{-1}$ . For a wind speed of  $11 \text{ m s}^{-1}$ ,  $T_{Bh,rough}$  is about 4.5 K and  $T_{Bv,rough}$  is about 2.1 K. Here, we use a reference value of 3.5 K as the lowest  $T_{B,rough}$  value for our analysis. A threshold of 0.002 is also applied to exclude Sentinel-1  $\sigma^{0,VH}$  lower than the noise equivalent sigma zero (NESZ) where signal-to-noise ratio (SNR) will be weak. The threshold is an approximation of the top NESZ value presented for Sentinel-1 EW mode in cross-polarization (Mouche et al., 2017). Note that we only use Sentinel-1 NRCS acquired in the EW mode for analyses (i.e., results shown in Figure 43 and Figure 44).

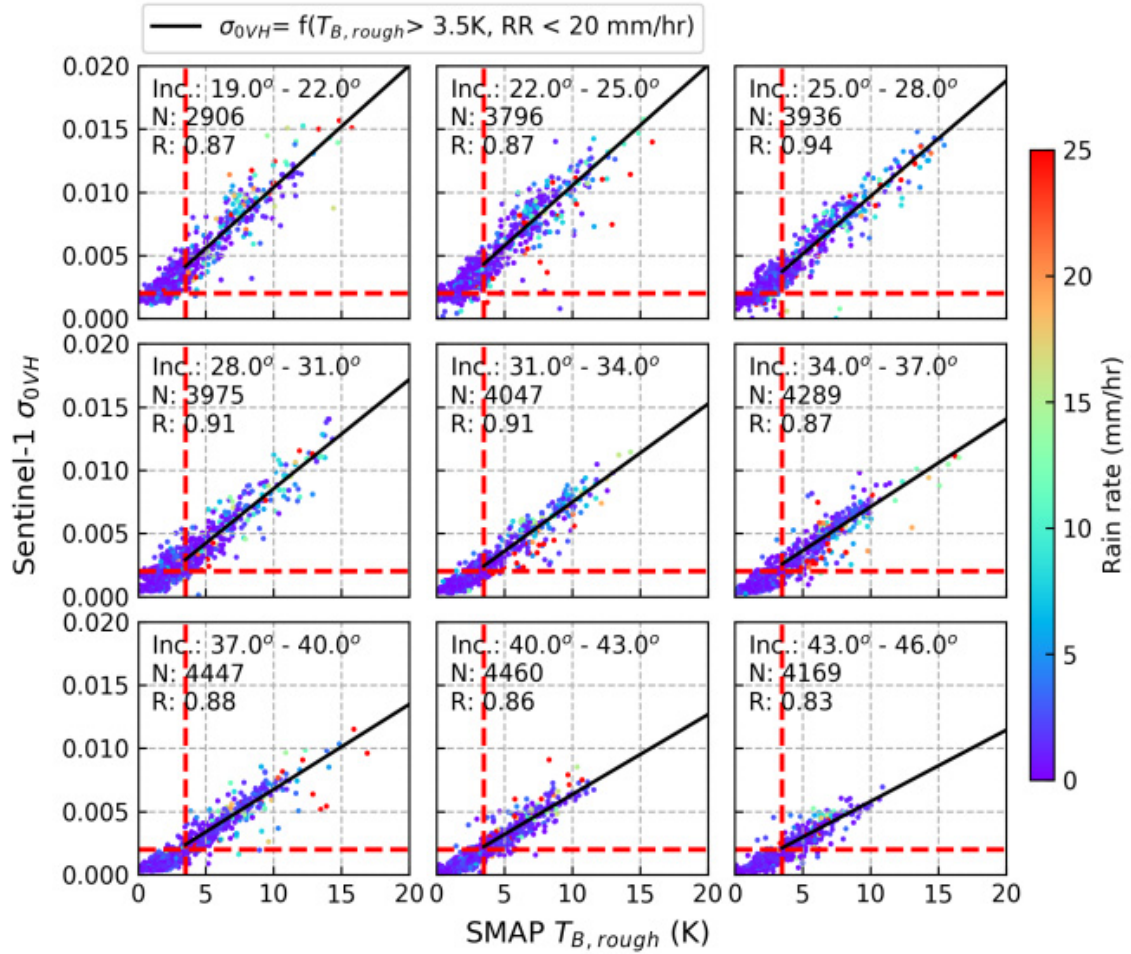


Figure 43: Sentinel-1  $\sigma^{0,VH}$  versus SMAP  $T_{B,rough}$  for different incidence angle and rain rate. Inc., N, and R are incidence angle, the number of points and the Pearson correlation coefficient, respectively.

Sentinel-1 EW mode covers incidence angles ranging from 18.9° to 47.0°. We, therefore, split the collocations into nine different incidence-angle range groups with bin width of 3°. In Figure 43, we present for each of these nine incidence angle bins the SMAP L-band  $T_{B,rough}$  (x-axis in Kelvin) against Sentinel-1 C-band  $\sigma^{0,VH}$  (y-axis in linear unit). The colour code indicates the rain rate (in mm per hour). For rain rate lower than 20 mm/h, C-band  $\sigma^{0,VH}$  (linear value) linearly increases with SMAP  $T_{B,rough}$  at all incidence angles. This linear trend sustains up to about 17 K for all SAR incidence angles between 19° and 40° and up to 12 K for larger incidence angles. No saturation is observed in the C-band  $\sigma^{0,VH}$ . The linear relationship is incidence ( $\theta_{SAR}$ ) angle-dependent and may be expressed as

$$\sigma^{0,VH}(\theta_{SAR}) = K(\theta_{SAR}) \times T_{B,rough}(\theta_{SMAP} = 40^\circ)$$

where  $K(\theta_{SAR}) = 1.24e^{-3} - 7.06e^{-4} \times \tan(\theta_{SAR})$ , is valid for  $\theta_{SAR}$  in the range between 19° and 46°. For heavy rain conditions ( $RR > 20$  mm/h), this linear relationship is not blurred. This indicates that L-band  $T_{B,rough}$  and C-band  $\sigma^{0,VH}$  do not have the same sensitivity to rain or rain-induced effects (e.g., wind downbursts or SSS changes) when computed at 25-km resolution.

The scatter plots of Sentinel-1  $\sigma^{0,VV}$  against SMAP  $T_{B,rough}$  are shown in Figure 44. A larger scatter between  $T_{B,rough}$  and  $\sigma^{0,VV}$  than between  $T_{B,rough}$  and  $\sigma^{0,VH}$  is clearly observed. We attribute this

larger scatter to the wind direction and perhaps incidence-angle effect on  $\sigma^{0,VV}$ , which is larger than the effect for  $\sigma^{0,VH}$  (Vachon and Wolfe, 2011). In addition, the analysis presented in Figure 44 suggests that rain tends to be dominant at crosswind (low NRCS) wind directions. Alternatively, rain may diminish the  $\sigma^{0,VV}$  values at all incidence angles, but that would pose a difference with respect to the VH results. Ignoring the dominance of wind direction,  $\sigma^{0,VV}$  increases with  $T_{B,rough}$  for incidence angles ranging from  $19.0^\circ$  to  $34^\circ$  until  $T_{B,rough} = 7.5$  K. Then  $\sigma^{0,VV}$  starts to decline. For incidence angles between  $34^\circ$  and  $40^\circ$ , these two regimes in the  $\sigma^{0,VV}$  variation with respect to  $T_{B,rough}$  are still observed, but exhibit less spread.  $\sigma^{0,VV}$  dynamic is found to be smaller at large incidence angles with maximum lower than 0.3 ( $-5.23$  dB). The co-analysis between C-band  $\sigma^{0,VV}$  and L-band  $T_{B,rough}$  indicates a loss of sensitivity of  $\sigma^{0,VV}$  for  $T_{B,rough}$  above 7.5 K roughly.

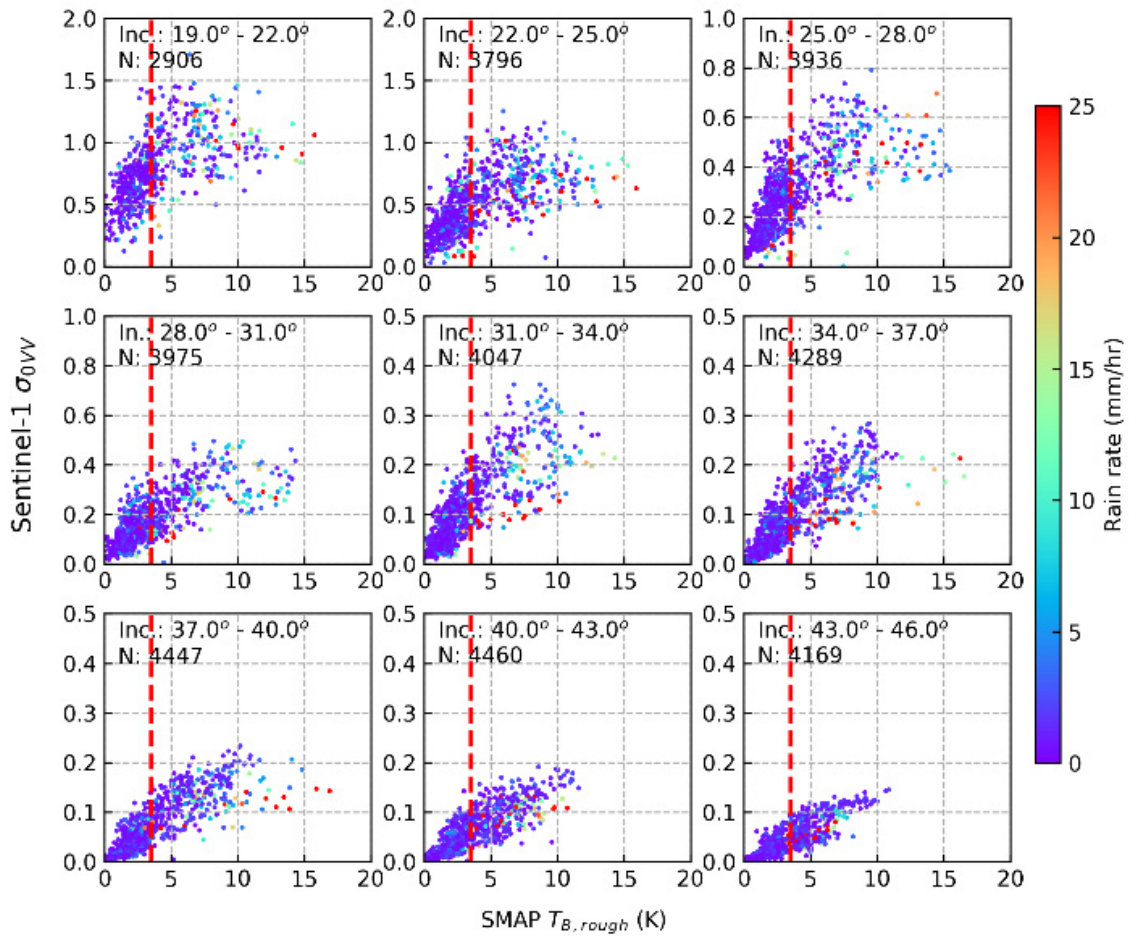


Figure 44: Sentinel-1  $\sigma^{0,VV}$  versus SMAP  $T_{B,rough}$  for different incidence angle and rain rate. Inc., N, and R are incidence angle, the number of points and the Pearson correlation coefficient, respectively.

### Conclusions on L band comparison

Our analyses show that the C-band cross-polarized backscattered signal has a sensitivity very similar to L-band passive sensors. For a given incidence angle, a proportional factor can be found between both quantities. Contrarily, the C-band  $\sigma^{0,VV}$  sensitivity generally decreases for  $T_{B,rough}$  values larger than 7.5 K. In terms of wind speed, based on the relationship from Meissner et al. (2017), the linear relationships between C-band  $\sigma^{0,VH}$  and L-band  $T_{B,rough}$  remains valid for wind speeds up to  $50 \text{ m s}^{-1}$ , and C-Band  $\sigma^{0,VV}$  appears to reduce its sensitivity for wind speeds larger

than 20–30 m s<sup>-1</sup> (depending on the incidence angle). This is somewhat inconsistent with operational practise and with Figure 23, comparing ASCAT to SFMR, showing sensitivity up to 40 m s<sup>-1</sup>, which is probably due to the large scatter due to wind direction in Figure 44, making the above assertion dependent on the sampled wind direction PDF and rather coarse.

The co-polarized and cross-polarized C-band NRCS behaviour are reasonably well predicted by physically-based models, where second-order scattering contributions are needed for modelling the VH NRCS (Fois et al., 2015) and returns are strongly sensitive to wave breaking processes (Kudryavtsev et al., 2014) for common winds. Yet, under extreme conditions, the increased transfer of energy per unit area can result in direct disruption of the interface between air and water, through the development of Kelvin–Helmholtz (KH) instabilities (Soloviev and Lukas, 2006). As such, long breaking waves may be less impacted than shorter wave breakers, that can be totally wiped out. Such a physical mechanism may explain the common sensitivity between the overall microwave emissivity and cross-polarized backscatter signals, as well as the saturation of the co-polarized signal for extreme winds. From a more applicative point of view, we confirm here again that having both co-polarization and cross-polarization channels on the future generation scatterometers, such as the next MetOp-SG will be a strong asset for wind measurements over extreme conditions. Moreover, in the view of producing long-term series of homogeneous wind measurements from multiple sources, we note that for the use of both this new VH channel and for L-band radiometer winds an in-situ reference will be needed for wind calibration. At 25-km resolution, when the rain rate is significant (>20 mm/h), we found that the sensitivities of L-band  $T_{B,rough}$  and C-band  $\sigma^{0,VH}$  are different. Uncertainties in the computation of the flat ocean surface contribution and in the rain rate over extreme events such as hurricanes make the error analysis quite challenging. A thorough assessment of the rain impact on both sensors certainly deserves further specific studies.

## 6.6. Summary

The results generally confirm the enhanced sensitivity of the VH polarization C-band NRCS to extreme winds. The demonstrated useful range has been extended to 70 m s<sup>-1</sup>. The sensitivity appears very similar to L-band passive brightness temperatures. Hence, measurement quality will depend on antenna beam stability and noise, which appear both quite favourable for SCA.

Spatial aggregation in tropical hurricanes has been investigated with SAR data and a box-car average over a distance larger than 25 km (i.e., > 15 km resolution) appears to dramatically degrade the hurricane structure and hence the wind speeds. The data sources also allowed the investigation of rain, which clearly affects the NRCS. However, distinguishing between cloud droplet effects, ocean surface roughness changes and wind downbursts remains challenging. On the other hand, the combination of different polarizations and frequencies opens the way for further more in-depth studies into rain effects.

## 7. DISCUSSION AND CONCLUSIONS

One of the CHEFS project objectives is to investigate and obtain a consolidated in-situ reference for the calibration of satellite and NWP model winds, which are generally stable, but lack absolute calibration. Two in-situ references are investigated that are mutually inconsistent in the common wind speed range of 15 to 25 m s<sup>-1</sup>. This work focuses on the collection, collocation, and analysis of five different high and extreme-wind datasets over a period of 10 years (2009-2018): SFMR, dropsondes, buoy, ASCAT and ERA5. To this end, three main analyses have been carried out by comparing: (i) SFMR and dropsondes winds; (ii) ASCAT and SFMR winds; and (iii) ASCAT and buoy winds.

Another CHEFS objective is to investigate the spatial representation of dropsonde, SFMR, SAR and ASCAT winds. SFMR is calibrated with respect to the WL150 dropsonde data and hence consistency of both sources in calibration is expected. SFMR and reprocessed dropsonde data provided by the NOAA/NESDIS/STAR OSWT, are analysed for calibration and validation purposes. The dropsonde data refer to Tropical Cyclone conditions, outside the storm eyewall. The SFMR winds have been reprocessed using a new version of the GMF [Sapp *et al.*, 2019]. The results of our analysis show that WL150 dropsonde and SFMR surface winds agree well, with a correlation coefficient of 0.9, a mean bias of 0.6 m s<sup>-1</sup> and a mean SD of about 4 m s<sup>-1</sup>. Similar results are obtained when comparing the dropsonde winds with the SFMR along-track averaged winds at different spatial scales (i.e., 200 m, 1 km, 5 km, 10 km, 25 km). The best dropsonde/SFMR agreement is found for SFMR 10-km averaged winds, indicating that the spatially and temporally integrated dropsonde surface wind measurement is representative of SFMR winds of 10-km resolution or smaller, where the 10-km optimum is probably determined by the typical collocation distance and the vertical averaging in WL150.

An analysis on the dropsonde WL150 algorithm used to estimate the dropsonde surface winds has also been carried out. The results show that when using a 150-m layer at altitudes higher than the nominal  $z_{mean} = 85$  m (e.g., for cases in which the dropsonde fails to report wind measurements close to the surface), the WL150 winds are biased high (as compared to the nominal case). Both the bias and the SD of the wind difference between the collocated SFMR wind and the corresponding WL150 wind increase for increasing  $z_{mean}$ . In addition, the bias is not constant, but rather scales with the wind speed. Therefore, the 0.85 factor (ratio) usually used in the dropsonde wind processing, to convert the WL150 wind into 10-m wind, should be dependent on  $z_{mean}$ , as also suggested by Uhlhorn *et al.*, (2007). The functional form of the ratio between dropsonde surface wind and the corresponding WL150 defined by Uhlhorn *et al.* (2007) is revised. The revised formulation is different to that of Uhlhorn *et al.* (2007), leading to notable ratio discrepancies at  $z_{mean} > 200$  m. This is probably due to the different dropsonde data set used to derive such equations. Note also that the SFMR/dropsonde statistics also change with the WL layer thickness. In particular, the WL25 (based on a layer thickness of 25 m) winds best agree with both the dropsonde lowest reading and SFMR winds. Low-level dropsonde winds appear mutually very consistent and consistent with a logarithmic profile. However, estimates of the 10-m wind are very sensitive to the dropsonde height sampling and knowledge. In summary, different WL algorithms lead to somewhat different winds.

The ASCAT winds have been reprocessed using the new CMOD-7 GMF and collocated ERA5 model winds as background winds. In order to collocate ASCAT and SFMR winds, the Best-Track (BT) data from the IBTrACS dataset version v03r10, available at the NOAA National Climate Data Center along with the BT data from the National Hurricane Center have been used to estimate

hurricane mean motion. The SFMR trajectory has been converted into storm-motion relative coordinates. This allows to collocate SFMR with ASCAT even when they are separated by a few hours in time. However, such approach cannot be used for large time differences. Several sources of collocation errors have been reported, namely the BT temporal sampling and geolocation inaccuracies and the temporal differences between the SFMR and ASCAT acquisitions. In particular, it is concluded that ASCAT/SFMR collocations with time differences larger than 3 h should be discarded from the analysis. The ASCAT/SFMR wind comparisons reveal substantially lower ASCAT winds at wind speeds higher than  $15 \text{ m s}^{-1}$ . Despite such disagreement, at high winds ASCAT is well correlated with SFMR winds, with a correlation coefficient of about 0.9, where a recalibration of ASCAT to SFMR winds leads to very consistent datasets. It is however questionable whether such recalibration to SFMR is physically plausible.

Indeed, very different results are obtained when comparing the nominal ASCAT  $U_{10S}$  with buoy  $U_{10N}$  winds. ASCAT wind products are in good agreement with collocated moored buoy winds up to  $25 \text{ m s}^{-1}$ , with ASCAT only slightly lower with respect to buoys for winds above  $15 \text{ m s}^{-1}$ , which is probably due to the lacking  $U_{10N}$  to  $U_{10S}$  conversion of the moored buoy data. Moreover, although buoy wind data show increased variance under high wind conditions, they show low bias and are generally found to be of reasonable quality between  $15$  and  $25 \text{ m s}^{-1}$ , indicating that moored buoy winds can be used for high-wind calibration and validation purposes. Open issues on the quality of moored buoy winds have been addressed in this range. Effects of the WBL are thought to be small, although the vertical displacement of small buoys in a typically logarithmic wind profile could result in a systematic low measurement bias of 3-5% (Taylor et al., 1999). WMO reports as typical measurement uncertainties obtained from operational moored buoys as follows: Wind speed  $1 \text{ m s}^{-1}$  or 5% above  $20 \text{ m s}^{-1}$  (WMO, 2018), while differences between moored buoys and dropsondes are larger above  $20 \text{ m s}^{-1}$ , cf. Figure 22a) and Figure 31.

Another open question is related to the fundamental measurements of the dropsonde, i.e., the position measurement, which is proprietary information of the GPS manufacturers. Since the dropsonde is increasingly decelerated along its path towards the ocean surface, the position filtering could have systematic effects on position (lag), hence on speed and acceleration of the sonde, which are used to determine the 10-m wind. Detailed information from manufacturers appears essential to understand possible errors (error propagation modelling is needed).

In this work, ASCAT is used as a stable reference to overcome the lack of buoy and SFMR collocations. Both SFMR and buoy winds are very well correlated with ASCAT, however, discrepancies between SFMR and buoy winds are seen in the high-wind scaling. Therefore, at this stage, conclusions cannot be drawn on which high-wind reference should be used for scatterometer wind calibration and validation at high and extreme wind conditions. Further investigations are needed to better understand the sources of such differences.

Scatterometers measure sea surface roughness and for verification purposes  $U_{10S}$  is derived, since  $U_{10S}$  can be verified against in-situ buoy and dropsonde winds, as well as against NWP wind references. High winds are generally associated with low pressure and hence with low air mass density, which limits the air-sea momentum transfer and the generation of sea surface roughness. Therefore, the conversion from  $U_{10N}$  to  $U_{10S}$  is needed for satellite surface wind calibration.

High and extreme moored buoy winds from the ECMWF MARS archive are shown to be of good quality and more abundant than archived buoy data at buoy data portals. A remaining concern exists in the quality-control procedures elaborated for these archives and their effect on the

presence of high and extreme buoy winds. Further work is needed to track the archive quality control for extreme cases.

The MetOp Second-Generation scatterometer SCA will host a cross-polarization (VH) channel for the retrieval of extreme winds. Using Sentinel-1 hurricane campaign winds, the VH GMF has been further verified. To conclude, the simple relationships shown in this and previous studies suggest the benefit of using the VH measurements for a near-real-time wind speed measurement in the case of Hurricanes and Typhoons, thereby enabling hurricane prediction centers to improve their forecasts and safety and damage advisories. The VH signal shows a beneficial skill with respect to wind speeds up to  $75 \text{ m s}^{-1}$ . Moreover, the excellent calibration stability of scatterometers, makes the addition of a VH channel on SCA a real asset in extreme winds. We note that SCA measurements will not capture the maximum 1-minute sustained winds as used for hurricane advisories, due to its too coarse spatial resolution and hence some statistical guidance remains necessary for the application of VH winds.

L-band radiometer and VH responses to extreme winds over the ocean are very similar and linearly related to close approximation. It will be useful to further explore the rain sensitivity of both measurement types, since these sensitivities are of a different nature. Whereas, C-band returns may be affected by heavy rain clouds, L-band measurements are affected by changing SST and SSS in a hurricane. The coarse resolution of L-band radiometer data is a limitation in such research.

## 8. RECOMMENDATIONS

Within an international setting much progress has been achieved in CHEFS. Nevertheless, to proceed with the much-needed consolidated in-situ reference, several open aspects need to be further addressed to achieve well-calibrated consolidated high and extreme satellite surface winds, inter alia, from wind scatterometers such as ASCAT and SCA.

A more thorough evaluation of the different spatio-temporal averaging procedures of both dropsonde and SFMR winds is recommended in order to better address the representativeness issues of both data sources and further improve the SFMR calibration. We suggest to include additional analysis using logarithmic wind profiles in order to further investigate the observed dropsonde 10-m winds, which are a more direct calibration resource for the 10-m surface wind than WL150 estimates. In this respect, the suggested association of wind bursts with humidity deficits and swell waves has not been further explored so far. The topic also includes an assessment of the position processing of the sonde near the surface, where its deceleration is maximum. A better understanding of the accuracy and reliability of the dropsonde wind measurements at the surface level is also needed as they are used in the dropsonde surface wind estimate algorithms (WL150).

The collocated GTS and archive buoy wind reports surfaced great consistency, but also many high wind reports that are not available in the archives, which issue has been communicated with JCOMM. Further investigation is needed to find the main reasons for this discrepancy. Furthermore, as buoy winds are our major resource for nominal satellite wind calibration, a closer collaboration with JCOMM, satellite wind producers and ECMWF will be very beneficial to consolidate the in situ, satellite winds and NWP community practises.

In addition, and to help establish a consolidated in-situ wind reference for satellite wind and NWP model calibration and tuning, one should exploit the few available moored buoy and dropsonde collocations.

$U_{10N}$  to  $U_{10S}$  conversions need to be implemented for all scatterometer wind comparisons, particularly at high and extreme winds, as these mainly occur at low pressures and hence low air mass density.

ASCAT winds show sensitivity to high winds, but lack good GMF calibration due to the lack of a consolidated in-situ wind reference. The saturation of the GMF at extreme winds is somehow compensated by the high calibration stability of the ASCAT instrument. As a result, further backscatter calibration refinements will support the retrieval of good-quality ASCAT winds in extreme conditions. In addition, GMF development and wind retrieval studies will be useful to improve high and extreme winds, in particular after that a consolidated in-situ wind reference has been established.

As more S1 SAR campaign data are collected, improved VH GMFs may be obtained in extreme winds. Since VH GMFs are closely related to L-band  $T_B$  and wind relationships, it is useful to further investigate geophysical effects (e.g., rain, SST, SSS) in both VH and L-band winds by using, for example, S1 and SMAP collocations. In addition, since NOAA embarked a VH antenna on a hurricane hunter airplane, these comparisons and results may be compared with spatially high-resolution and well-located comparisons between the airplane VH measurements and all of SFMR, dropsondes and the airplane range-gated scatterometer IWRAP measurements.

## 9. REFERENCES

- Ayet, A., Chapron, B., Redelsperger, J.L. *et al.*, 2019, On the Impact of Long Wind-Waves on Near-Surface Turbulence and Momentum Fluxes, *Boundary-Layer Meteorol.*, <https://doi.org/10.1007/s10546-019-00492-x> .
- Banal, S., Iris, S., & Saint-Jean, R. (2007, July). Canadian space agency hurricane watch program: Archive contents, data access and improved planning strategies. Proceeding of IEEE International Geoscience and Remote Sensing Symposium, 3494–3497. <https://doi.org/10.1109/IGARSS.2007.4423599> .
- Carswell J. R., W. J. Donnelly, R. E. McIntosh, M. A. Donelan, and D. C. Vandemark, "Analysis of C and Ku band ocean backscatter measurements under low-wind conditions," *J. Geophys. Res.*, vol. 104, no. C9, pp. 20 687–20 701, Sep. 1999.
- Chou K., Wu C., and Lin S., Assessment of the ASCAT wind error characteristics by global dropwindsonde observations, *J. of Geophysical Research: Atmosphere*, 118, 9011–9021, 2013, <https://doi.org/10.1002/jgrd.50724> .
- Copernicus Climate Change Service (C3S) (2017): ERA5: Fifth generation of ECMWF atmospheric reanalyses of the global climate. Copernicus Climate Change Service Climate Data Store (CDS), date of access. Available at: <https://cds.climate.copernicus.eu/cdsapp#!/home>
- De Kloe J., Stoffelen A. and Verhoef A., Improved Use of Scatterometer Measurements by Using Stress-Equivalent Reference Winds, *IEEE J. of Selected Topics in Applied Earth Observations and Remote Sensing*, vol. 10, no. 5, pp. 2340-2347, 2017.
- Donnelly W. J., J. R. Carswell, R. E. McIntosh, P. S. Chang, J. Wilkerson, F. Marks, and P. G. Black, "Revised ocean backscatter models at C and Ku-band under high-wind conditions," *J. Geophys. Res.*, vol. 104, no. C5, pp. 11 485–11 497, May 1999.
- Edson, J.B., V. Jampala, R.A. Weller, S.P. Bigorre, A.J. Plueddemann, C.W. Fairall, S.D. Miller, L. Mahrt, D. Vickers, and H. Hersbach, 2013: [On the Exchange of Momentum over the Open Ocean](https://doi.org/10.1175/JPO-D-12-0173.1). *J. Phys. Oceanogr.*, **43**, 1589–1610, <https://doi.org/10.1175/JPO-D-12-0173.1>
- Fernandez, D.E., Kerr, E.M., Castells, A.; Carswell, J. R.; Shaffer, S.J.; Chang, P.S.; Black, P.G.; Marks, F.D. IWRAP: The Imaging Wind and Rain Airborne Profiler for Remote Sensing of the Ocean and the Atmospheric Boundary Layer within Tropical Cyclones. *IEEE Trans. Geosci. Remote Sens.*, 43, 1775–1787, 2005.
- Fois, F., P. Hoozeboom, F. Le Chevalier and A. Stoffelen, 2015, "Future Ocean Scatterometry: On the Use of Cross-Polar Scattering to Observe Very High Winds", *IEEE Transactions on Geoscience and Remote Sensing* **53** (9), 5009-5020, <https://doi.org/10.1109/TGRS.2015.2416203> .
- Foster, Ralph, Chris Fairall, 2015, GPS Dropsondes, Scatterometer High Winds Workshop, December 9-10, 2015, National Hurricane Center, Miami, FL, USA.
- Franklin, J.L., Black M.L., Valde K., GPS Dropwindsonde Wind Profiles in Hurricanes and Their Operational Implications. *Weather Forecast*, 18, 32–44, 2003,
- Hersbach H., and Dee D., ERA5 Reanalysis is in Production, *ECMWF Newsletter*, 147, 2016, available online at: <https://confluence.ecmwf.int/display/CKB/What+is+ERA5>

- Hoareau N., Portabella M., Lin W., Ballabrera-Poy J. and Turiel A., 2018, Error Characterization of Sea Surface Salinity Products Using Triple Collocation Analysis, *IEEE Trans. Geosci. Remote Sens.*, 56, 9, 5160-5168, <https://doi.org/10.1109/TGRS.2018.2810442> .
- Hock, T.F. and J.L. Franklin, 1999: *The NCAR GPS Dropwindsonde*. *Bull. Amer. Meteor. Soc.* **80**, 407–420, [https://doi.org/10.1175/1520-0477\(1999\)080<0407:TNGD>2.0.CO;2](https://doi.org/10.1175/1520-0477(1999)080<0407:TNGD>2.0.CO;2)
- Horstmann, J., Wackerman, C., Falchetti, S., & Maresca, S. (2013, June). Tropical cyclone winds retrieved from synthetic aperture radar. *Oceanography*, 26. Retrieved from <https://doi.org/10.5670/oceanog.2013.30> .
- Hwang, P. A., Stoffelen, A., van Zadelhoff, G.-J., Perrie, W., Zhang, B., Li, H., and Shen, H. (2015), Cross-polarization geophysical model function for C-band radar backscattering from the ocean surface and wind speed retrieval, *J. Geophys. Res. Oceans*, 120, 893– 909, doi:[10.1002/2014JC010439](https://doi.org/10.1002/2014JC010439).
- Knapp, K.R., Kruk M.C., Levinson D.H., Diamond H.J., and Neumann C.J., The International Best Track Archive for Climate Stewardship (IBTrACS): Unifying tropical cyclone best track data, *Bulletin of the American Meteorological Society*, 91, 363-376, 2010, <https://doi.org/10.1175/2009BAMS2755.1> .
- Kudryavtsev V., I. Kozlov, B. Chapron, and J. A. Johannessen, 2014, “Quad-polarization SAR features of ocean currents,” *J. Geophys. Res. Oceans*, vol. 119, no. 9, pp. 6046–6065.
- Lin W., Portabella M., Stoffelen A., Vogelzang J., and Verhoef A, ASCAT wind quality under high subcell wind variability conditions, *J. Geophys. Res. Oceans*, 120, 5804– 5819, 2015, <https://doi.org/10.1002/2015JC010861> .
- Lin W., Portabella M., Stoffelen A., Vogelzang J., Verhoef A., On Mesoscale Analysis and ASCAT Ambiguity Removal, *Quarterly Journal of the Royal Meteorological Society*, 142, 697, 1745-1756, 2016.
- Liu W.T., Katsaros K., and Businger J., Bulk Parameterization of Air-Sea Exchanges of Heat and Water Vapor Including the Molecular Constraints at the Interface. *J. of Atmospheric Sciences*, 36, 1722-1735, 1979.
- Meissner T. , L. Ricciardulli, and F. J. Wentz, “Capability of the SMAP mission to measure ocean surface winds in storms,” *Bull. Amer. Meteorol. Soc.*, vol. 98, no. 8, pp. 1660–1677, Aug. 2017.
- Mouche Alexis, Chapron Bertrand, Zhang Biao, Husson Romain (2017). Combined Co- and Cross-Polarized SAR Measurements Under Extreme Wind Conditions . *IEEE Transactions On Geoscience And Remote Sensing* , 55(12), 6746-6755. <https://doi.org/10.1109/TGRS.2017.2732508>.
- Mouche Alexis, Chapron Bertrand, Knaff John, Zhao Yili, Zhang Biao, Combot Clement (2019). Co-polarized and Cross-Polarized SAR Measurements for High-Resolution Description of Major Hurricane Wind Structures: Application to Irma Category 5 Hurricane . *Journal Of Geophysical Research-oceans* , 124(6), 3905-3922. Retrieved from <https://doi.org/10.1029/2019JC015056>.
- Newell A. C. and V. E. Zakharov, “Rough sea foam,” *Phys. Rev. Lett.*, vol. 69, no. 8, pp. 1149–1151, Aug. 1992.
- Piepmeier J. et al., “Algorithm theoretical basis document SMAP L1B radiometer brightness temperature data product: L1B\_TB,” NASA/GSFC, Greenbelt, MD, USA, Tech. Rep. SMAP-ALGMS-RPT-0026, 2016.

Pineau-Guillou, Lucia, Arduin Fabrice, Bouin Marie-Noelle, Redelsperger Jean-Luc, Chapron Bertrand, Bidlot Jean-Raymond, Quilfen Yves (2018). Strong winds in a coupled wave-atmosphere model during a North Atlantic storm event: evaluation against observations. *Quarterly Journal Of The Royal Meteorological Society*, 144(711 Part.B), 317-332. Publisher's official version : <https://doi.org/10.1002/qj.3205> , Open Access version : <https://archimer.ifremer.fr/doc/00410/52118/> .

Potter, Henry, Hans C. Graber, Neil J. Williams, Clarence O. Collins, Rafael J. Ramos, and William M. Drennan, 2015, In situ Measurements of Momentum Fluxes in Typhoons, *J of the Atmospheric Sciences* 72, 104-118, <https://doi.org/10.1175/JAS-D-14-0025.1> .

Reul N. and B. Chapron, "A model of sea-foam thickness distribution for passive microwave remote sensing applications," *J. Geophys. Res. Oceans*, vol. 108, no. C10, p. 3321, Oct. 2003.

Reul N., et al., "SMOS satellite L-band radiometer: A new capability for ocean surface remote sensing in hurricanes," *J. Geophys. Res. Oceans*, vol. 117, no. C02006, Feb. 2012.

Reul N., et al., "A revised L-band radio-brightness sensitivity to extreme winds under tropical cyclones: The five year SMOS-storm database," *Remote Sens. Environ.*, vol. 180, pp. 274–291, Jul. 2016.

Reul N. et al., "A new generation of tropical cyclone size measurements from space," *Bull. Amer. Meteorol. Soc.*, vol. 98, no. 11, pp. 2367–2385, Nov. 2017

Sapp J.W., Alswiss S.O., Jelenak Z., Chang P.S., Carswell J., Stepped Frequency Microwave Radiometer Wind-Speed Retrieval Improvements. *Remote Sens.*, 11, 214, 2019, <https://doi.org/10.3390/rs11030214> .

Soloviev A. and R. Lukas, *The Near-Surface Layer of the Ocean: Structure, Dynamics and Applications (Atmospheric and Oceanographic Sciences Library)*, vol. 31. Dordrecht, The Netherlands: Springer, 2006.

Stoffelen, A. Toward the true near-surface wind speed: Error modeling and calibration using triple collocation, *J. Geophys. Res.*, 103, 7755–7766, 1998, <https://doi.org/10.1029/97JC03180> .

Taylor, Peter K., Elizabeth C. Kent, Margaret J. Yelland, and Ben I, 1999, THE ACCURACY OF MARINE SURFACE WINDS FROM SHIPS AND BUOYS, Moat, Southampton Oceanography Centre, Southampton, SO14 3ZH, UK, <https://pdfs.semanticscholar.org/af18/9a756bc6b1e85df8a66a1c74153d913c185c.pdf> .

Uhlhorn, E.W., Black, P.G., Franklin J.L., Goodberlet M., Carswell, J., Goldstein, A.S., Hurricane Surface Wind Measurements from an Operational Stepped Frequency Microwave Radiometer. *Mon. Weather Rev.*, 135, 3070–3085, 2007.

Vachon, P. W. and Wolfe, J.: C-band cross-polarization wind speed retrieval, *IEEE Geosci. Remote S.*, 8, 456–459, <https://doi.org/10.1109/LGRS.2010.2085417> , 2011.

Zadelhoff, G.-J. van, Stoffelen, A., Vachon, P. W., Wolfe, J., Horstmann, J., and Belmonte Rivas, M.: Retrieving hurricane wind speeds using cross-polarization C-band measurements, *Atmos. Meas. Tech.*, 7, 437–449, <https://doi.org/10.5194/amt-7-437-2014> , 2014.

Vogelzang J., Stoffelen A., Verhoef A., and Figa-Saldana J., On the quality of high-resolution scatterometer winds, *J. Geophys. Res.*, 116, C10033, 2011, <https://doi.org/10.1029/2010JC006640> .

Verhoef, A. and Stoffelen A., ASCAT Wind Product User Manual version 1.16, 2019. Available online at: [http://projects.knmi.nl/scatterometer/publications/pdf/ASCAT\\_Product\\_Manual.pdf](http://projects.knmi.nl/scatterometer/publications/pdf/ASCAT_Product_Manual.pdf)

WMO, 2017, Guide to Meteorological Instruments and Methods of Observation, [https://library.wmo.int/doc\\_num.php?explnum\\_id=4147](https://library.wmo.int/doc_num.php?explnum_id=4147).

Xu, Xingou & Stoffelen, Ad (2019), Improved Rain Screening for Ku-Band Wind Scatterometry, IEEE Transactions on Geoscience and Remote Sensing, 1-10, <https://doi.org/10.1109/TGRS.2019.2951726> .

Yueh S. H. et al., "SMAP L-band passive microwave observations of ocean surface wind during severe storms," IEEE Trans. Geosci. Remote Sens., vol. 54, no. 12, pp. 7339–7350, Dec. 2016.

Zhang, B., & Perrie, W. (2012). Cross-polarized synthetic aperture radar: A new potential technique for hurricanes. Bull. Amer. Meteorol. Soc., 93 , 531–541.

Zhang, G., Li, X., Perrie, W., Hwang, P. A., Zhang, B., & Yang, X. (2017). A Hurricane Wind Speed Retrieval Model for C-Band RADARSAT-2 Cross-Polarization ScanSAR Images. IEEE Transactions on Geoscience and Remote Sensing, 55 , 4766-4774.

## 10. ACRONYMS

AFRC	Air Force Reserve Command (USA)
ASCAT	Advanced scatterometer on MetOp
ASPEN	Atmospheric Sounding Processing Environment (NCAR)
AWDP	ASCAT Wind Data Processor (OSI SAF)
BT	Best Track
C	microwave frequency band (ASCAT, S1, RadarSat)
C3S	Copernicus Climate Change Service (EU)
CC	Correlation Coefficient
CHEFS	C-band High and Extreme-Force Speeds (this project)
CMEMS	Copernicus Marine Environment Monitoring Service (EU)
CMOD7	C-band GMF ( <a href="http://projects.knmi.nl/scatterometer/cmod7/">http://projects.knmi.nl/scatterometer/cmod7/</a> )
COARE	Coupled Ocean Atmosphere Response Experim. ( <a href="http://www.soest.hawaii.edu/COARE">www.soest.hawaii.edu/COARE</a> )
Cwinds	Continuous buoy winds (NOAA archive)
ECMWF	European Centre for Medium-range Weather Forecasts
ENVISAT	Environmental Satellite (ESA)
ERA	ECMWF Re-Analysis
ERS	European Remote-sensing Satellite (ESA)
ESA	European Space Agency
EU	European Union
EUMETSAT	European Meteorological Satellite organization
EW	Extra Wide swath mode SAR (S1)
GMF	Geophysical Model Function
GPM	Global Precipitation Mission
GPS	Global Positioning System
GRDH	Ground Range Detected High resolution SAR (S1)
GRIB	GRIdded Binary or General Regularly-distributed Information in Binary form
GTS	Global Telecommunication System (WMO)
HH	Horizontal polarisation transmitted and received
Himawari	Japanese geostationary satellite
IBTrACS	International Best Track Archive for Climate Stewardship (WMO)
ICM	Institut de Ciències del Mar
ICOADS	International Comprehensive Ocean-Atmosphere Data Set (NOAA)
ID	Identification code
IFREMER	Institut Français de Recherche pour l'Exploitation de la Mer (
IFS	Integrated Forecast system (ECMWF)
IMERG	Integrated Multi-satellitE Retrievals for GPM (NASA)
IOVWST	International Ocean Vector Winds Science Team
ITT	Invitation To Tender
IW	Interferometric Wide swath mode SAR (S1)
IWRAP	Imaging Wind and Rain Airborne Profiler (NOAA)
JAMSTEC	Japan Agency for Marine-Earth Science and Technology
KNMI	Royal Netherlands Meteorological Institute
L	microwave frequency band (SMAP)
L1	Level-1 satellite instrument data; geolocated, calibrated measurements
LKB	Liu-Katsaros-Businger atmospheric surface layer
LR	Lowest Reading
MARS	Mass Archive and Retrieval System (ECMWF)
MDA	MacDonald Dettwiler and Associates

MetOp	Operational Meteorological polar satellite (EUMETSAT)
MLE	Maximum Likelihood Estimator
NASA	National Aeronautics and Space Administration (USA)
NCAR	National Center for Atmospheric Research (USA)
NDBC	National Data Buoy Center (USA)
NESDIS	National Environmental Satellite, Data, and Information Service (USA)
NEXRAD	Next-Generation Radar, network of 159 S-band weather radars (USA)
NHC	National Hurricane Centre (USA)
NOAA	National Oceanic and Atmospheric Administration (USA)
NRCS	Normalised Radar Cross Section
NUIST	Nanjing University of Information Science and Technology
NWP	Numerical Weather Prediction
ODAS	Ocean Data Acquisition System buoys
OSI SAF	Ocean and Sea Ice Satellite Application Facility (EUMETSAT)
OSVW	Ocean Surface Vector Wind
OSWT	Ocean Surface Winds Team (STAR)
PDF	Probability Density Function
PDS	Power Density Spectra
PIRATA	Prediction and Research Moored Array in the Atlantic
PMSL	Mean Sea Level Pressure
QC	Quality Control
RadarSat	Commercial Earth observation satellite with SAR (Canada)
RAMA	Research Moored Array for African–Asian–Australian Monsoon Analysis and Prediction
RMW	Radius of Maximum Winds
RSMC	Regional Specialized Meteorological Centres
S1	Sentinel-1 (EU Copernicus)
SAR	Synthetic Aperture Radar
SCA	Scatterometer planned on MetOp-SG (EUMETSAT)
SD	Standard Deviation
SFMR	Stepped-Frequency Microwave Radiometer
SG	Second Generation
SHOC	Satellite Hurricane Observations Campaign (S1)
SM	Strip Map SAR mode (S1)
SMAP	Soil Moisture Active Passive instrument (NASA)
SSS	Sea Surface Salinity
SST	Sea Surface Temperature
STAR	Center for Satellite Applications and Research (NESDIS)
TAO	Tropical Ocean Atmosphere buoys (NOAA)
TC	Tropical Cyclone
TRITON	Triangle Trans-Ocean Buoy Network (JAMSTEC)
TsH	Temperature sensor Height
UCAR	University Corporation for Atmospheric Research
UTC	Universal Time Coordinate
VH	Vertical polarisation transmitted and Horizontal received
VV	Vertical polarisation transmitted and received
WBL	Wave Boundary Layer
WL150	Algorithm to estimate wind at 10-m height from the lowest 150 m of measurements
WMO	World meteorological Organization
WOA	World Ocean Atlas
WV	Wave SAR mode (S1)
WVC	Wind Vector Cell